Computational Investigation of Magnetic Hyperthermia for Complex-Shaped Tumor using Finite Volume Immersed Boundary Method

A Thesis

submitted in partial fulfilment of the requirement

for the award of the degree of

Doctor of Philosophy

in Engineering

Submitted by:

Mr. Amritpal Singh

(Regn. No. 901808002)

Under the guidance of

Dr. Neeraj Kumar

Assistant Professor, MED

Department of Mechanical Engineering
Thapar Institute of Engineering & Technology,
(Deemed to be University) Patiala-147004, India

October 2023

DECLARATION

I, **Amritpal Singh** hereby certify that the work presented in this thesis report entitled "**Computational Investigation of Magnetic Hyperthermia for Complex-Shaped Tumor using Finite Volume Immersed Boundary Method**" in partial fulfillment of the requirement for the award of the degree of **Doctor of Philosophy** and submitted in Mechanical Engineering department of Thapar Institute of Engineering & Technology (Deemed to be University), Patiala, is an authentic record of my own research work carried out during a period from July 2018 to September 2023 under the supervision of **Dr. Neeraj Kumar,** Assistant Professor, Mechanical Engineering Department of Thapar Institute of Engineering & Technology, Patiala. The matter presented in this thesis has not been submitted by me for the award of any other degree of this or any other Institute.

Amritpal Singh

(Registration no. 901808002)

This is to certify that the above statement made by the candidate is correct to the best of our knowledge and belief.

(Dr. Neeraj Kumar)

Assistant Professor, MED

Thapar Institute of Engineering & Technology

(Deemed to be University), Patiala-147004, Punjab, India

Dedicated to my Parents Sh Nishan Singh, Smt Sarabjeet Kaur, Brother Jobanpreet Singh, Wife Prabhjot Kaur and Daughter Anand Kaur

ACKNOWLEDGMENTS

It is a great pleasure for me to express my respect and a deep sense of gratitude to my Ph.D. supervisor Dr. Neeraj Kumar, Assistant Professor, Mechanical Engineering Department, Thapar Institute of Engineering Technology, Patiala, for his wisdom, vision, expertise, guidance, enthusiastic involvement, and persistent encouragement during the planning and development of this research work. I also gratefully acknowledge his painstaking efforts in thoroughly going through and improving the manuscripts without which this work could not have been completed.

I am highly obliged to Prof. Padmakumar Nair, Director, Thapar Institute of Engineering Technology, Patiala, and Dr. N. Tejo Prakash, Senior Professor & Dean, Research and Sponsored Projects for the encouragement, support, and necessary facilities to carry out and complete this work on a steady course. I am also thankful to present Chairman of the Doctoral Committee Dr. T. K. Behra, Senior Professor & Head, Department of Mechanical Engineering, for the much-needed support throughout the work for providing all the facilities, help, and encouragement for carrying out the research work.

I am very thankful to Dr. Bhupendrakumar Chudasama, Professor, School of Physics and Materials Science, Dr. Sayan Sadhu, Assistant Professor, Department of Mechanical Engineering and Dr. Madhup Kumar Mittal, Associate Professor, Department of Mechanical Engineering, for being the members of the Doctoral Committee and spending their valuable time reviewing and critically examining the work.

I also wish to express my deep sense of gratitude to Dr. Manish Kumar, Assistant Professor, Department of Mechanical Engineering, MNIT, Jaipur, for introducing the Immersed Boundary Method. I would like to express my loving gratitude to my family members, especially to my Mother Smt. Sarabjeet Kaur, and to my wife Mrs. Prabhjot Kaur for their patience, love, and encouragement during this journey.

I wish to express my appreciation to my friends Kashminder Singh Mehta, and Gurmeet Singh and thanks to research fellows at the department for their help and motivation throughout my research work. I also would like to express my deep and sincere thanks to my friends and all other persons whose names do not appear here for helping me either directly or indirectly in all even and odd times.

I am also thankful to the anonymous reviewers of my research publications. Their comments and suggestions were very helpful in shaping my research work. I would also like to extend my special thanks to Mrs. Promila, Charnjeet Singh and other staff members of the MED Department, for their timely help and cooperation, extended throughout the course of the investigation.

Finally, I am indebted and grateful to the Almighty for helping me in this endeavor.

(MR. AMRITPAL SINGH)

ABSTRACT

Magnetic nanoparticle hyperthermia therapy (MNPH) is an emerging cancer treatment modality owing to its advantage of minimal invasive as well as can target irregular deep-rooted and poorly accessible tumors. Hyperthermia utilizes heat to sensitize pathological (cancerous) tissues for chemo/radiation therapy or to directly kill the cancerous cell through thermal ablation. However, achieving precise control of the spatial thermal dose within the tumor region is challenging due to various factors. These include tissue physiology, the size and shape of tumors, the distribution of magnetic nano-particle (MNP) in the tissue and magnetic field parameters. Since the tumors can have any irregular shape, thus devising the treatment protocol for MNPH for complexly shaped tumor remains a challenging task. Application of computational methodology can assist to clinician to devise a suitable treatment protocol for hyperthermia therapy. Computational simulation of the bioheat models in the complex tissue is challenging and computationally intensive due to the unavoidable complexity associated with the body-fitted grid generation. The objective of the present study is to develop the Cartesian grid based finite volume immersed boundary method (FV-IBM) for the bioheat transfer equation. The developed FV-IBM framework is used to simulate and analyze intratumoral MNPH therapy in complex and real tumor models.

Immersed boundary method (IBM) is employed to enforce the boundary effect on the non-body conformal Cartesian grid. The finite volume method (FVM) is used as a numerical technique to discretize the governing equations. The validation and verification of the FV-IB method have shown that the scheme is nearly second-order accurate. Furthermore, the numerical results in the spherical tumor model are in good agreement with previously reported results for steady and transient cases. Results for MNP-based hyperthermia investigation with two heat source (Gaussian and uniform) distribution patterns in the liver tumor are in good agreement with the numerical solution of COMSOL Multiphysics. Thus, a simple and robust FV-IBM based numerical scheme is proposed to solve the bioheat models in arbitrary tissue shapes.

The developed FV-IBM framework is used to investigate the effects of tumor shape on magnetic nanoparticle hyperthermia (MNPH) using four categories (spherical, oblate, prolate, and egg-shape) of tumor models having different morphologies. These tumors have equal volume; however, due to the differences in their shapes, they have different surface area. The shape of tumors is quantified in terms of shape factor (ζ). Magnetic hyperthermia is applied

(frequency 150 kHz, and magnetic field amplitude 20.5 kA/m) to all tumor models, for 1 hour, after injection of magnetic nanoparticles (MNP) at the respective tumor centroids. The distribution of MNP after injection is considered as Gaussian. Results show that the therapeutic effects of MNPH depend significantly on the shape of a tumor. Tumors with higher shape factors receive less therapeutic effects in comparison to the tumors having lower shape factors. An empirical thermal damage model is also developed to assess the MNPH efficacy in real complex-shaped tumors.

Intratumoral multi-injection strategy enhances the efficacy of magnetic nanoparticle hyperthermia therapy (MNPH). Further a criterion for the selection of injections and their location depending on the tumor shape/geometry is also developed. Developed strategy is based on the thermal dosimetry results obtained on different invasive 3D tumor models during MNPH simulation. Primary and secondary injections are used to inject MNP, based on the invasiveness of the tumor. Optimizing strategy is devised based on the zone of influence of primary and secondary injections. Results indicate that the zone of influence of secondary injection lies between the 0.7 and 0.8 times the radial distance between the center of tumor core and the branch node point. This zone of influence of secondary injection produces minimum heterogeneity of temperature in the tumor model. Additionally, the multi-injection strategy is more effective when the protrusion volume exceeds 10% of the total volume. The developed criterion for the selection of multi- injection strategy and the location of the injection point can help in devising treatment protocol for magnetic nanoparticle hyperthermia therapy.

Moreover, a supplementary study is also conducted to analyze the cooling effect caused by blood vessels on a MNPH. The MNPH is simulated on the physical models constructed from DICOM images using the open-source 3D-Slicer software. The physical model comprises cancerous tissue, blood vessels, and surrounding liver tissue. Intratumoral injection of magnetic nanoparticles (MNP) is used to deliver MNP at the center of the tumor volume. In order to perform the parametric study, the tumor's position with respect to the blood vessel is changed. The therapeutic effect is evaluated based on the percentage of tumor volume exceeding the therapeutic threshold temperature of 43°C. The results indicate that there is a significant increase in the cooling effect when the tumor is in close proximity to the blood vessel. Close proximity of blood vessel with respect to tumor reduces the effectiveness of MNPH. However, this cooling effects diminish when tumor is away from the major blood vessels.

Contents

List of Figures

List of Tables

List of Acronyms/Abbreviations

AMF	Alternating magnetic field
BNF	Bionized nano ferrite
CAD	Computer aided design
CHT	Conjugate heat transfer
CT	Computed tomography
DICOM	Digital Imaging and Communications in Medicine
DS	Degree of stasis
FDM	Finite difference method
FEM	Finite element method
FV-IBM	Finite Volume immersed Boundary method
FVM	Finite volume method
GAs	Genetic algorithms
HI	Heterogeneity index
IBM	Immersed boundary method
LBM	Lattice Boltzmann method
MNPH	Magnetic nanoparticle hyperthermia
MNP	Magnetic nanoparticles
MRI	Magnetic resonance imaging
MTT	Minimum therapeutic temperature
NM	Nelder-Mead algorithm
PBHT	Penne's bioheat transfer
PSO	Particle swarm optimization
RMS	Root mean square
SA	Simulated annealing
SAR	Specific absorption rate (kg/m^3)
SLP	Specific loss power (W/kg)
STL	Stereo-Lithography
TB	Tumor Boundary
TD	Thermal dosimetry
TV	Tumor Volume
WHO	World health organization

List of Symbols

T_{10}, T_{90}	Minimum temperature within 10% and 90% tissue volume (K)
A_a	Pre-exponential factor (1/s)
C_D	Thermal damage
C_p	Specific heat (J/(kg·K))
E_a	Activation energy (J/mol)
T_a	Arterial temperature (K)
V_d	MNP distributed volume (m^3)
V_p	Tumor protruded portion volume (m^3)
m_i	Mirror nodes
q_{es}	External heat source (W/m^3)
q_m	Metabolic heat generation (W/m^3)
r_o	Core radius (m)
ω_b	Blood perfusion rate (1/s)
ω_{bi}	Initial blood perfusion rate of tissue (1/s)
ΔV	Volume of discretized elements (m^3)
Δt	Time step (s)
$CEM43$	Cumulative equivalent minutes (min)
$\emptyset$	Volume fraction
A	Surface area (m^2)
$C(\tau)$	Survival fraction of tissue at time τ
H	Magnetic strength (A/m)
M	MNP total amount (mg)
R	Universal gas constant (J/mol/K)
R	Radius (m)
T	Temperature (K)
V	Volume (m^3)
k	Thermal conductivity (W/(m·K))
m	MNP amount in each control volume (mg)
r	Radial distance (m)
x, y, z	Cartesian coordinate index

Ω	Thermal damage
α, β, γ	Quadratic fit coefficients
ε	Root mean square error
ζ	Shape factor
η	Normal vector
ξ	Normalized distance between ghost and surface node
ρ	Density (kg/m^3)
σ	Standard deviation
τ, t	Time (s)

Subscript

e,w,n,s	East, west, north, south
H	Healthy tissue
T	Tumor
tis	tissue
b	blood
i, j, k	Node index

Superscript

t	time

Chapter 1

Introduction

1.1 Background

Cancer is a leading cause of human death as indicated by statistics [1–3]. According to a report from the Ministry of Health and Family Welfare in India, cancer is responsible for more than four lakhs deaths every year in the country [4]. The term "cancer" encompasses the uncontrolled growth and spread of abnormal cells in the body. Some common types of cancer leading to solid tumors include breast, lung, colorectal, and prostate cancer. These tumors can be either benign or malignant, benign ones grow slowly and do not spread, while malignant tumors proliferate uncontrollably, invading nearby tissues and spread to other body parts (as shown in Figure 1.1). Whereas others like Leukaemia, Lymphoma, Multiple Myeloma, and Myeloproliferative Neoplasms do not manifest as solid tumors. Among the prevalent forms of cancer causing significant mortality rates in humans are lung, breast, colorectal, stomach, and liver cancer [1].

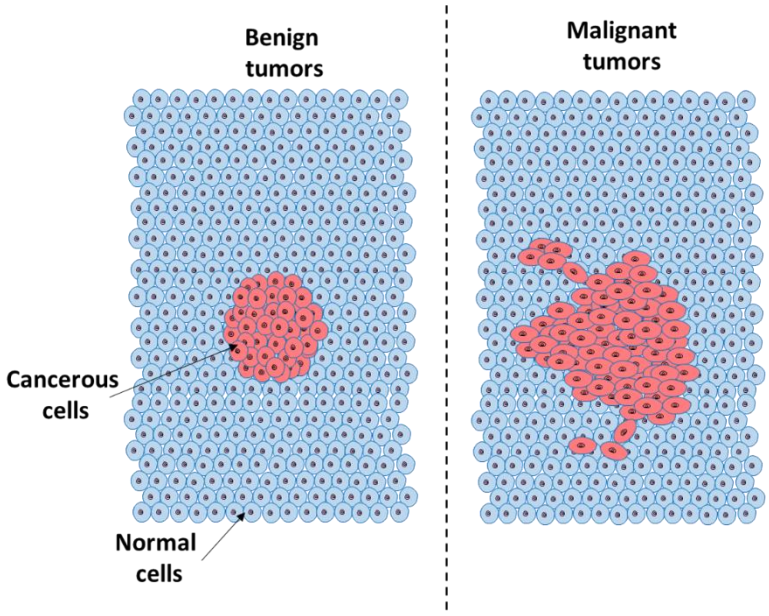

Figure 1.1. Depiction of the benign and malignant tumors

Clinicians and researchers have been striving to combat the menace of cancer, resulting in the availability of several treatment methodologies to reduce or eliminate tumors. Conventional approaches for the cancer treatment are surgery, chemotherapy, and radiotherapy. Conventional cancer therapies can have long and short-term side effects that

impact a patient's health. [5–7]. Thus, there exists a societal need for safe, and least-invasive therapy that can effectively cure cancer while minimizing the risk of adverse effects. Hyperthermia is one of the emerging anticancer modalities that uses heat to destroy cancer cells or make them more sensitive to other cancer treatments such as radio and chemotherapy [8–11].

1.1.1 Hyperthermia

Hyperthermia means to elevate local or global body temperature. The biological and physiological effects of tissue heating enhance the damaging probability of the tissue. Furthermore, the cancer cells are more vulnerable to heating than the normal tissue cells [8–10]. Therefore, in this therapy, tumor temperature is elevated to the therapeutic range of 4 to 5 ℃ from normal body temperature and maintained about 0:5–2 hours. The extreme case of hyperthermia (thermo-ablation) involves raising the tissue temperature above 50℃ for a short duration to directly ablate the tumor tissue [12–15]. Various types of local hyperthermia inducers are laser, microwave antenna, ultrasound and magnetic nanoparticles (MNP) etc [16–18]. Among them, magnetic nanoparticles hyperthermia (MNPH) have the advantage of being minimally invasive as well as can target irregular deep-rooted and poorly accessible tumors [14,19–22].

1.1.2 Magnetic nanoparticle hyperthermia

In the MNPH, the superparamagnetic nanoparticles are injected into the tumor region via intravascular or intratumoral injections [23]. In an intravascular method, MNP are injected into the artery, and the particles are transported to the targeted tumor by carrier fluid. The distribution of MNP within the tumor depends on the efficiency of the carrier vascular system and local blood perfusion in a tumor. Thus, there are higher probabilities of vascular leakage, which directly influence the delivery and distribution of MNP to the targeted tumor. In another approach (intratumoral injection), the nanoparticles are directly injected into the tumor [8]. This leads to minimum MNP leakage, and the control of particle distribution is much higher compared to intravascular injection. However, directly injecting the MNP particles to the targeted tissue has its own clinical challenges. Following that, the MNP are exposed to the alternating magnetic field (AMF) (as shown in Figure 1.2). Owing to the Brownian and Neel relaxation mechanism under the AMF, the MNP begin to produce heat [8,24]. This heating raises the temperature in the tumor and surrounding healthy region [14,25,26]. The heating

capacity of MNP, which is defined as specific loss power (SLP), depends upon various factors such as AMF strength, frequency, MNP properties and its spread in the tissue [19,27–32]. Two types of MNP that are generally used in various in-vivo investigations are magnetite (Fe_3O_4), and maghemite (Fe_2O_3) [9].

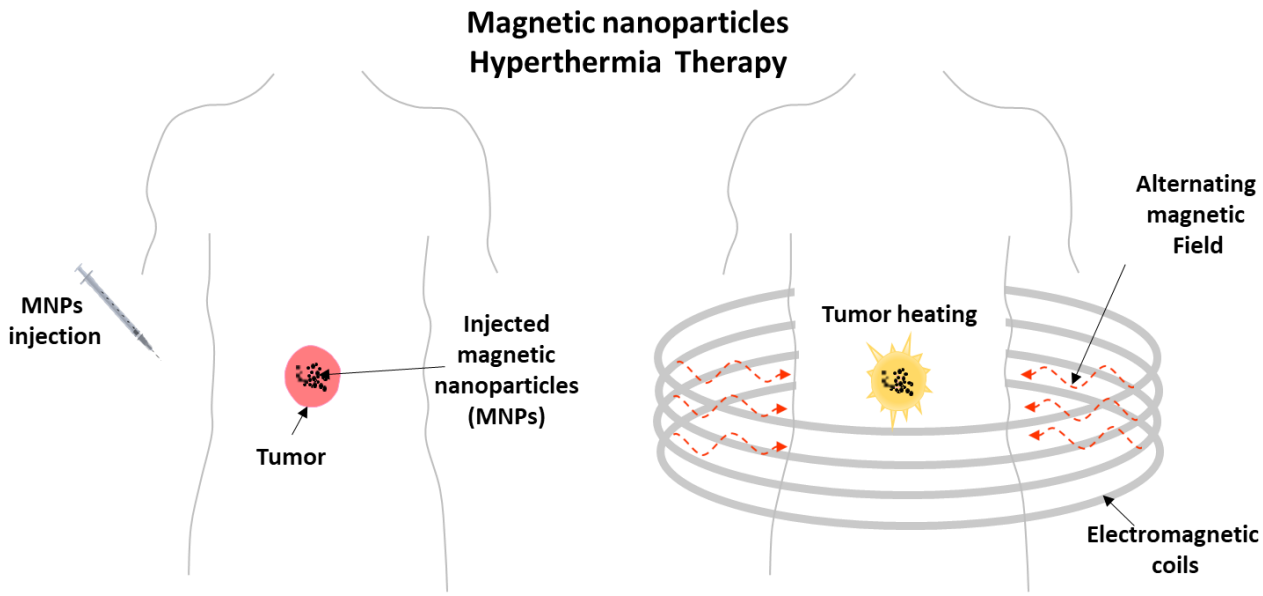

Figure 1.2. Depiction of the magnetic hyperthermia therapy.

Many preclinical and clinical investigations have successfully demonstrated the applicability of the MNPH therapy [9,19,30,33]. In 2005, Wang et al. [31] conducted both in vitro and in vivo studies of magnetic hyperthermia therapy. They found that various factor, such as MNP size, dispersion rate, surfactants, and magnetic field influence the heating value of MNP. In their in-vivo investigation, a total amount 50 mg of MNP were injected into a 2 cm size of liver carcinoma in rabbit. After exposing the tumor to a magnetic field of 20kA/m and frequency 55kHz, the core tumor temperature was elevated to 45℃ within 5 minutes. Johannsen et al. [34] in their in vivo experiments on rats, have reported the maximum temperature of 70℃ with 18 kA/m magnetic field and 100kHz frequency. In another experiment with 12.6kA/m field strength, the maximum temperature of 54.8℃ at the tumor center and 41.2 ℃ at the tumor periphery was observed. Furthermore, it was found that the MNPH inhibited tumor growth significantly by $44-51\%$. Based on these observations, Johannsen et al. [35] performed the first clinical trial to assess the feasibility of magnetic hyperthermia therapy in patients with prostate tumours. The maximum temperature reported in the prostate was 55℃ under a frequency 100kHz and 4.5kA/m magnetic field. The results

indicated that local tissue heating to thermoablative temperature with magnetic hyperthermia technology is achievable. Jordan et al. [36] conducted an in vitro investigation to examine the SAR of ferrite material under varying magnetic field strengths ranging from 0 to 1.6 kA/m. The study found that the SAR (Specific absorption rate) is comparable to RF heating with a 5 mg per gram tumor concentration of MNP under clinically acceptable magnetic field and power. An in-vivo study conducted by Wang et al. [37] in 2014, investigated the feasibility of magnetic hyperthermia therapy in rats with Walker-265 breast carcinomas. The authors injected a total dose of 62.5mg/ml magnetic fluid intratumorally to the tumor volume and exposed it for 30 minutes under the frequency of 180 kHz and a magnetic field 55 GS. The study found that repeated MNPH therapy inhibited the tumor growth and enhanced the survival of the tumor-bearing rats. Thus, various pre-clinical as well as clinical studies have demonstrated the feasibility of MNPH for cancer treatment.

Experimental investigations and clinical trials have demonstrated that magnetic hyperthermia therapy can selectively focus on tumor tissue and substantially increase its temperature. However, there are many practical limitations associated with MNPH, one of these is controlled elevation of the temperature within the tumor tissue. The spatial temperature elevation in tumor during MNPH is affected by various factors such as the amount of MNP dose, magnetic field properties, and nanoparticle distribution etc. The morphological aspect of tumors (as most of the tumors are irregular in shape with high aspect ratios) also complicates the distribution of MNP in tumor mass, [38,39]. Thus, the chances of spatial ill-distribution of MNP in tumor tissue and diffusion and dispersion of MNP in healthy tissue are quite high. This leads to less potent therapeutic effects and also inadvertent heating or damaging of the healthy tissue. Therefore, targeting the tumors having complex morphology using MNPH is still a challenging task.

As discussed earlier, the distribution of MNP within tissue plays a pivotal role in achieving the required temperature profile during Magnetic Nanoparticle Hyperthermia (MNPH). This becomes especially crucial due to tumor tissue's intricate and irregular structure. In 2008, Salloum et al. [30] experimentally investigated the effect of infusion rate (varied from 1.25μl/min to 40 μl/min) on different agarose gel concentrations. Results demonstrated that a sufficiently low infusion rate could create a uniform spherical like distribution profile with a higher concentration near the point of injection. However, higher injection rates do not produce symmetric MNP dispersion in the tissue. In a subsequent in-vivo investigation into rat limb, Salloum et al. [9] studied temperature elevation by injecting 0.1 cc and 0.2 cc of MNP and

found that nanoparticles concentration is higher in the vicinity of the injection site when the injection amount is bigger. A similar phenomenon has been observed by Attaluri et al. [19] in an in-vivo study on rats with prostatic tumor. The study observed that a slow infusion rate leads to less volumetric distribution of MNP (i.e., MNP are more confined in the vicinity of injection site), which increases the localised heating within the tumor during thermotherapy. Thus, MNP distribution in the targeted tissue is one of the key parameters in MNPH, which depends on injection rate and tissue physiology. As the tumors can have any arbitrary shape, thus confined distribution of MNP in the tumor tissue is challenging. Researchers have explored multiple methods to enhance the effectiveness of MNPH such as multi-injection strategy for MNP delivery, and power modulation technique [20,40–47].

1.1.2.1 Multi-injection strategy

In the intratumoral multi-injection strategy, more than one MNP injection is inserted in the tumor region (as described in Figure 1.3). This strategy offers the advantage of increasing MNP distribution region within the tumor. Consequently, the therapeutic effect enhances [20,44–46]. However, evaluating the position of injection sites and the amount of MNP in each site is one major challenge. In the previous works, different optimization techniques such as Nelder-Mead (NM), a genetic algorithm (GAs), simulated annealing (SA), particle swarm optimization (PSO) etc are used to develop the multi-injection strategy. In 2009, Salloum et al. [20] used NM optimization algorithm to obtain the optimized heat source and its distribution around the injection sites. The objective of this algorithm is to elevate the temperature of, at least 90 per cent of a tumor volume near or above the therapeutic range, while not more than 10 per cent of healthy tissue volume should thermally affected. The number of injection sites and its position is defined based on the several random spheres covering the total tumor volume. Mittal et al. [48] have optimized the spatial and temporal parameters which affect the heating within the tissue using a genetic algorithms (GAs). The application of the algorithm was used in a 3D spherical tumor. Tang et.al. [49] have shown that the NM method (prior used by Salloum et al. [20]) has stability issues due to the higher dependency on initial parameters. They have used another optimization method, i.e. simulated annealing (SA) for multi-injection MNPH. Later, Tang et.al. [42] proposed a strategy to optimize the injection dose and its location for magnetic hyperthermia using metaheuristic algorithm. Boroon et al. [46] used the conjugate gradient approach to evaluate the best injection locations and the optimized heat source in a 2D square brain tumor model. The results showed that increasing the injection sites could lead to larger tumor damage; however, injecting MNP fluid to multiple locations with

precision is challenging task. Singh et al [44] with their computational investigation have shown that the temperature field with multi-injection is more homogenous and uniform in a tumor than a single injection. Recently, Jiang et al. [43] used the PSO algorithm to explore the homogenous temperature distribution in circular and elliptical tumor models with different injections. They showed that the four injection sites could be an appropriate strategy for the required temperature distribution in spherical and elliptical tumor.

In most of these investigations, the locations or number of injections are pre-defined to devise the optimization algorithm and evaluate the power source and MNP distribution. However, the tumor-specific, number of MNP injections and its location is still undefined.

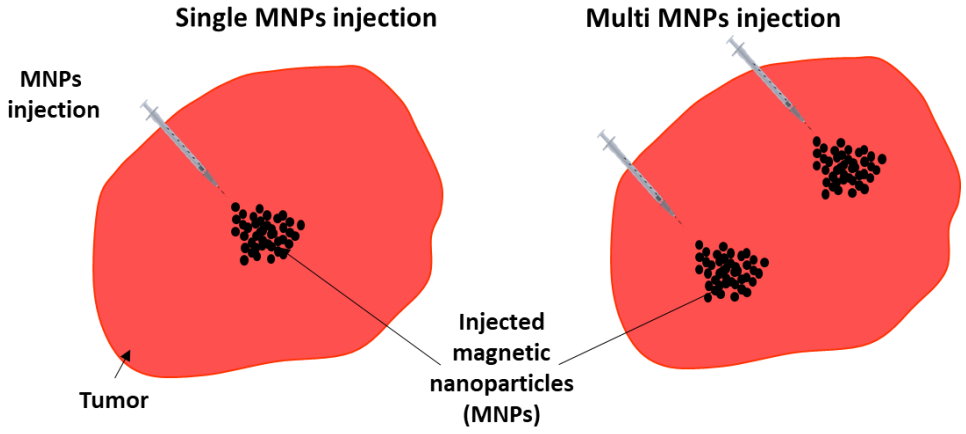

Figure 1.3. Depiction of the single and multi- MNP injections strategy.

1.1.2.2 Power modulation method

In power modulation methodology, the input power in terms of magnetic field strength or frequency has been varied to ensure that the tissue heating remains within the tumor region. In 2015, Soetaert et al. [50] have studied the effect of modulated and unmodulated magnetic field strength on MNPH within malignant liver tissue. Further, Kandala et al [40] have studied the effectiveness of power modulation to reduce the heterogeneity of temperature in the tumor due to the non-uniform distribution of magnetic nanoparticles in hyperthermia therapy. However, the maximum temperature reached within the tumor using power modulation is 16 per cent less as compared to constant power heating. Moreover, power modulation heating achieves the required thermal dose, up to 9 times quicker as compared to constant power heating. It should be noted that most of the optimization works for MNPH are done through the simulations. In these simulations, geometry of the tumors is simple, like spherical, cylindrical, ellipsoidal, or some random arbitrary shape. Limited works have been reported

where MNPH simulation are performed to optimise the governing parameters of MNPH on tumor models created from actual tumors.

Furthermore, most of the MNPH simulation considers the tumor position far from any major blood vessel. However, the cooling effect of blood vessel also influence MNPH therapy. Astefanoaei et al.[47] has investigated the cooling effect due to blood vessels. They observed that as the blood vessel's size reduces or blood flow's velocity decreases, the cooling effect caused by blood vessels get diminishes. In 2014, Yue et al. [51] studied the effect of a bifurcation of the blood vessel on the thermal dose. The geometric model of a 3D irregular-shaped tumor similar to a sphere enclosed within the healthy tissue, and the bifurcated vessel passes through the tumor region was simulated in the COMSOL software. They found that the large blood vessel and location of injection sites significantly affect the temperature distribution within the tumor. They observed that, the temperature of both large and small blood vessels did not increase significantly during MNPH. Tang et al. [52] performed a numerical study on a tumor model with a blood vessel intersecting through a spherical tumor. The results indicated that the presence of high blood flow inside the blood vessel significantly reduced the temperature in its surrounding area. Gheflati et al. [53] conducted a numerical investigation on the cooling effect of a large blood vessel in the tissue during laser-based hyperthermia therapy. The results revealed that as the blood velocity increases, the cooling effect of the vessel also increases, consequently reducing the potential thermal damage caused by the treatment.

1.2 Research Gaps

Numerous computational efforts have been reported to enhance the therapeutic effects of magnetic hyperthermia treatment, but still, there are many challenges for its successful clinical applications. In the simulation of MNPH therapy within tumor models, many researchers have predominantly employed basic tumor shapes like spheres or cubes, which may not accurately represent the complex and irregular morphology of actual solid tumors. [44,54–56]. However, it's worth noting that in the existing literature, solid tumors are categorized as segmental, discoidal, or irregular in shape [38,39]. Consequently, the effect of tumor morphology on the effectiveness of MNPH therapy has yet to be thoroughly investigated.

Various researchers have described that the multi-injection strategy can significantly enhance the effectiveness of MNPH therapy, especially in complex and arbitrarily shaped tumors [20,44–46,48]. In the multi-injection strategy, the precise position of injection sites

within tumors and the amount of MNP at each injection site are the two important factor. Previous researchers have utilized various optimization algorithms to optimize the multi-injection strategy [20,45,46,57]. However, it's important to note that in many of these studies, injection positions are predefined, focusing on optimizing the radial distribution of MNP and their associated heating value. Optimizing injection sites for 3D arbitrary tumor shapes can be computationally intensive, and as such, there is a need for a more straightforward and efficient method to assess the position of multi-injection sites.

Further, It has also been reported that the blood vessels close to the tumor affect the therapeutic region in the tumor during MNPH therapy [47,51]. However, quantitative analysis of the convective effect due to blood vessels is not much elaborated.

Generally the researchers have used numerical schemes such as the finite volume method (FVM), finite element method (FEM), Lattice Boltzmann method (LBM), and finite difference method (FDM) using body conformal mesh to compute the bioheat physics within tumor models[40,44,55]. However, the body conformal mesh generation in complex shapes is a time-consuming and cumbersome task that also affects the accuracy of computational results. The emerging numerical technique of immersed boundary methods (IBM), which works on non-body conformal grid structures or Cartesian grids, can help to overcome this issue [58,59]. IBM has been successfully implemented in various physics, such as fluid flow, heat transfer in complex physical domains as well as in bio-medical applications [59–62].

1.3 Objectives of this study

The following objective have been proposed in the present research work.

- The development and validation of Finite volume-immerged boundary method (FV-IBM) framework for a bio-heat model.
- Application of FV-IBM solver for the numerical solution of the bio-heat model in three-dimensional arbitrary complex-shaped tumor models for MNPH application.
- Investigation the effect of tumor shapes of complex tumor models on the treatment parameters
- Effects of injection strategies, MNP distributions, magnetic field parameters on therapeutic effect of magnetic hyperthermia in the three-dimensional arbitrary shaped tumor.

- Effects of convection on MNPH applications in the complexed three-dimensional tumor.

1.4 Motivation for the Research

MNPH therapy is one of the emerging hyperthermia cancer modalities owing to its minimum invasiveness and targeted approach for solid tumors. Over the years, numerous computational efforts have been dedicated to enhancing its effectiveness. However, upon reviewing the existing literature, it becomes evident that there are several important research gaps that need to be addressed. Addressing these gaps not only advances our understanding of MNPH but also contributes to enhance the application of MNPH therapy. One of the crucial factors influence the application of MNPH therapy is tumor morphology. Investigation the effect of tumor morphology on the MNPH therapy can enhance the prediction of therapeutic region. Over the last few decades, medical imaging has tremendously assisted clinicians in visualizing as well as accessing the pathological conditions of specific organs or localized body parts. These images are also utilized to generate 3D geometrical models of tissues or organs [63]. Therefore, the development of tumor specific multi-injection guiding criteria can provide some input to the clinician during the MNPH therapy. Additionally, the computational methodologies rely on numerical schemes to compute the bioheat physics within complex tumor shapes. The advantage of IBM in bioheat physics solvers offers to address the challenges posed by complex geometries more effectively. IBM allows us to tackle complex tumor shapes by the rectilinear grids without effecting the accuracy of the numerical solution.

1.5 Thesis organizations

The thesis chapters encompass detailed description of methodologies, results and discussion associated with each research objective or problem statement. The following is a brief overview of each chapter's content and objectives.

i) **Chapter 1** This chapter provides an overview of the topic, a literature review of computational and experimental-based MNP hyperthermia investigations, identification of research gaps, and the details of the objectives of the research work.

ii) **Chapter 2** In this chapter, the development and validation of the FV-IB method for simulating Penne's bioheat model for complex tumor shapes is described. The chapter discusses the details of the methodology and the validation.

iii) **Chapter 3** This chapter explores the impact of tumor shapes on MNPH therapy using the developed FV-IB method. The chapter investigates how different tumor shapes influence the effectiveness of the therapy, and the findings are presented and discussed.

iv) **Chapter 4** In this chapter, the development of a multi-injection MNP strategy aimed to enhance the therapeutic effect of MNPH using the FV-IB method is described. The chapter explains the devising criterion for MNP injections and their locations for MNPH therapy.

v) **Chapter 5** This chapter delves into the examination of the effect of blood vessels on MNPH therapy. The chapter discusses how the presence of blood vessels can influence the effectiveness of the MNPH therapy and presents the findings of the study. However, COMSOL Multiphysics software is used to simulate this bio-heat problem.

vi) **Chapter 6** provides the summary and conclusion of the present work. Additionally, this chapter outlines the scope for future work, identifying potential areas for further exploration and development in the field.

1.6 Closing remark

Magnetic nanoparticle hyperthermia therapy is an emerging therapy that utilizes heat to damage the cancerous cell solely or in conjunction with conventional therapies to augment their efficacy. Several computational researchers have delved into the study of heating profile to improve its overall efficiency. Yet, upon a comprehensive review of existing literature, notable research gaps become evident. Based on the research gaps, the primary objectives of our present study have been defined.

Chapter 2

Development of coupled finite volume immersed boundary method for the simulation of bio-heat transfer in 3D complex tumor

2.1 Introduction

The computation plays a significant role in investigating hyperthermia therapy. The complex tumor morphology and physiology make the computational investigation challenging and expensive. In previous works, investigators have applied different numerical methods such as finite element, finite volume, and the Lattice Boltzmann method [44,64,65] to discretize the bioheat model for the analysis of the MNPH therapy. However, for the complex morphology of tumors, the body-fitted structured or unstructured grid generation process is cumbersome and time-consuming. The increased complexity in tumor morphology deteriorates the quality of the grid, which can negatively affect the accuracy and convergence of the solver [60,61]. The advantage of immersed boundary method (IBM) over the other numerical methods is in terms of the implementation of boundary conditions by avoiding the body-conformal grids. In this chapter, the development and description of the numerical framework based on the finite volume immersed boundary method (FV-IBM) for bioheat transfer is elaborated. The methodology includes the discretization of the governing equation through the Finite Volume Method (FVM); and the implementation of the boundary conditions on the complex, and irregular-shaped surface through immersed boundary method (IBM). This numerical methodology is used to simulate MNPH on the 3D tumor models. These 3D tumor models are also generated from computed tomography (CT)/ MRI (magnetic resonance imaging) images through image segmentation and volume reconstruction of the tumor. The open-source 3D slicer software [63] is used to read, segment, and reconstruct surface/volume from these images. It helps in generating a 3D CAD (Computer aided design) model of the tumor from DICOM images. The CAD model inherits the surface information of three-dimensional objects in the Stereo-Lithography (STL) format. The STL format has the details of triangle vertices along with the unit normal vector of the triangular surface mesh. This STL information is utilized in IBM implementation to simulate these physics in complex geometries using a simple cartesian grid.

In this work, FVM is used to discretize the governing differential equation (Penne's bio-heat model) in Cartesian grids, and the boundary effect is reconstructed through the direct forcing function of IBM. Based on the FV-IBM methodology, in-house solver is developed to simulate bio-heat transfer in any complex tumor morphology. The procedure for implementation of various boundary conditions, like Dirichlet, Neumann, and conjugate heat transfer, is similar to that described by Das et. al. [61]. The validity and accuracy of the FV-IBM scheme are demonstrated through the solutions of the diffusion equation in the curvilinear geometry. Furthermore, the applicability of FV-IBM in bioheat physics is validated with analytical and previously reported numerical results in the spherical tumor model for steady and transient cases.

2.2 Numerical Methodology

2.2.1 Governing equation

A distinguishing factor of heat transfer in living systems is the influence of temperature on the blood flow within the local vascular structure. The blood flow through microcirculation within tissue, commonly known as perfusion [66,67]. The intricate vascularization and irregular tissue structure pose challenges in developing a mathematical model for this phenomenon. Many mathematical models have been proposed to account the heat transfer through the biological tissue [66,67].

A pioneer research carried out by the Penne's provided the first comprehensive mathematical model for heat transfer through the tissue. The author conducted a series of experiments on human forearms, measuring temperatures and formulating a model (equation 2.1) based on the conservation of thermal energy. This model is widely recognized as the classic, or Penne's Bioheat transfer (PBHT) model and differs from the standard heat transfer equation by incorporating the effects of metabolic heat generation and perfusion heat transfer [66]. PBHT is used to evaluate the tumor and healthy tissue temperature for hyperthermia physics as described in equation 2.1).

$$(\rho C_p)_{tis}\frac{\partial T}{\partial t} = \mathrm{k}_{tis}\nabla^2 T + \omega_b\left(\rho C_p\right)_b(T_a - T) + q_m + q_{es} \qquad 2.1$$

where ρ and C_p are the density and specific heat, respectively. The subscript 'tis' and 'b' represent tissue and blood properties, respectively. q_m and q_{es} are heat sources due to metabolism heat generation and external source supplied, respectively. k is the thermal

conductivity of tissue and ω_b is the time-dependent perfusion rate. T_a is the artery blood temperature that is considered $37°C$.

Owing to its simplicity and good accuracy, the PBHT model has been extensively utilized for predicting the temperature field in biological tissues [40,44,55,56]. However, the equation does possess certain limitations as it was not designed to account for various physical effects. The most notable drawback is its inability to consider the directionality of blood perfusion and, consequently, it does not describe any convective heat transfer mechanism [66]. In revisited Penne's article by Wissler [68], the justification of Pennes' equation was presented, acknowledging the identified flaws. The study concluded that *"those who base their theoretical calculations on the Pennes model can be somewhat more confident that their starting equations are valid"*[68].

2.2.2 Discretization of governing equation through FVM

As discussed in the previous section, the governing equation (equation 2.1) is discretized using the FVM. In the FVM, the physical domain is divided into minute elements that are named finite control volume (as shown in Figure 2.1) [69]. For discretization, the PBHT equation (as in equation (2.1)) is implicitly integrated, volumetrically and temporally, over each control volume in the 3D Cartesian numerical domain (equation (2.2)).

$$\underbrace{\int_{t,dV}^{t+dt} (\rho C)_{tis} \frac{\partial T}{\partial t} dV dt}_{\text{First term}} = \int_{t,dV}^{t+dt} \left(\underbrace{\mathrm{k}_{tis} \nabla^2 T}_{\text{Second term}} + \underbrace{\omega_b \left(\rho C_p\right)_b (T_a - T)}_{\text{Third term}} + \underbrace{q_m + q_{es}}_{\text{Fourth term}} \right) dV dt \qquad 2.2$$

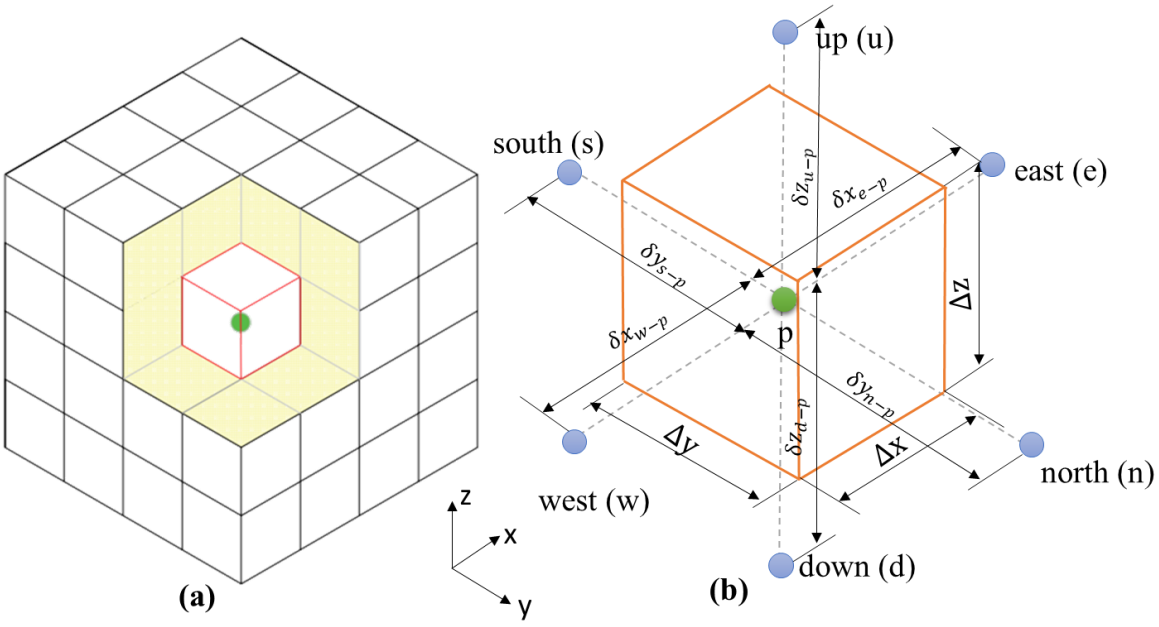

Figure 2.1. (a) Depiction of the 3D Cartesian grid **(b)** represents the unit cell or control volume of Cartesian grid and its terminology.

First term in equation (2.2) accounts for the rate of change in temperature in the tissue over time. After spatial and temporal integration, this term for arbitrary control volume 'p' yields the discretization form (equation (2.3)).

$$\int_{t,dV}^{t+dt} (\rho C)_{tis} \frac{\partial T}{\partial t} dV dt = (\rho C)_{tis} T|_{t}^{t+1} \Delta V = (\rho C)_{tis} \left(T_p^{t+1} - T_p^{t}\right) \Delta V \qquad 2.3$$

where T_p^{t+dt} and T_p^t are the temperature at time $t + dt$ and t, respectively. ΔV is the volume of control volume and Δt is the time step.

Second term in the equation (2.2) allows to conduct the heat energy within the tissue, it is also known as the conduction or diffusion term. The three-dimensional discretization form of this term by integrating spatially and temporally is shown in equation (2.4)

$$\begin{aligned}\int_{t,dV}^{t+dt} k_{tis} \nabla^2 T \; dV dt &= \int_{t,dV}^{t+dt} k_{tis} \left(\frac{\partial^2 T}{\partial x^2} + \frac{\partial^2 T}{\partial y^2} + \frac{\partial^2 T}{\partial z^2}\right) dV dt \\ &= \left(k_{tis} \left(\frac{T_e^{t+1} - T_w^{t+1}}{\delta x_{e-p}} - \frac{T_p^{t+1} - T_w^{t+1}}{\delta x_{w-p}}\right) A_x \right. \\ &+ k_{tis} \left(\frac{T_n^{t+1} - T_p^{t+1}}{\delta y_{n-p}} - \frac{T_p^{t+1} - T_s^{t+1}}{\delta y_{s-p}}\right) A_y \\ &\left. + k_{tis} \left(\frac{T_u^{t+1} - T_p^{t+1}}{\delta z_{u-p}} - \frac{T_p^{t+1} - T_d^{t+1}}{\delta z_{l-p}}\right) A_z \right) \Delta t\end{aligned} \qquad 2.4$$

where δx_{e-p}, δx_{w-p}, δy_{n-p}, δy_{s-p}, δz_{u-p}, and δz_{d-p} are the distance between the neighbouring nodes and control volume 'p' node in the east-west, north, south, up, and down direction, respectively (as shown in Figure 2.1). A_x, A_y, and A_z are the surface area of control volume ('p') perpendicular to the $x, y,$ and z directions. For the rectilinear grid structure, the surface area is such that $A_x = \Delta y \Delta z$, $A_y = \Delta x \Delta z$, and $A_z = \Delta x \Delta y$. Where, Δx, Δy, and Δz is the size of control volume 'p' in x, y, and z direction, respectively, as showm in Figure 2.1.

The third term incorporates heat transfer due to blood perfusion. It acts as heat sink during heating the tissue. The last term represents the heat generation in tissue by the metabolic process and external heat sources. The spatial and temporal integration of these terms give the following discretization form.

$$\int_{t,dV}^{t+dt} (\omega_b(\rho C)_b(T_a - T) + q_m + q_{es})\ dVdt = \left(\omega_b(\rho \mathrm{C})_b T_a + q_m + q_{es} - \omega_b(\rho \mathrm{C})_b T_p^{t+dt}\right)\Delta V \Delta t \quad 2.5$$

Solving and simplifying equation (2.2) leads to the system of algebraic equations of the following generalized form.

$$A_p T_p^{t+1} - \sum A_{nb} T_{nb}^{t+1} = B_p \quad 2.6$$

where, subscripts 'p' represents the position of the control volume where the solution is computed by using its neighbouring nodes 'nb' (as described in two-dimensional Figure 2.2). The adjacent nodes of control volume 'p' in three-dimensional rectilinear grids are denoted as eastern (e) - western (w), northern (n) - southern (s), and upper (u) - lower (l), in x, y, and z direction, respectively. The coefficients of A_p and A_{nb}, and the source B_p include the following terms.

$$A_e = k_t A_x/\delta x_{e-p}\ ,\ A_w = k_t A_x/\delta x_{w-p}\ ,$$

$$A_n = k_t A_y/\delta y t_{n-p}\ ,\ A_s = k_t A_y/\delta y_{s-p}\ ,$$

$$A_u = k_t A_z/\delta z_{u-p}\ ,\ A_l = k_t A_z/\delta z_{l-p}\ , \quad 2.7$$

$$A_p = A_e + A_w + A_n + A_s + A_u + A_l + \omega_b\left(\rho C_p\right)_b \Delta V + (\rho C_p)_t \Delta V\ /\Delta t$$

$$B_p = \ q_m + q_s + \ \omega_b(\rho C_p)_b \ T_a + \ (\rho C_p)_t \ T^t \Delta V/\Delta t$$

In the above-derived relations, A_x, A_y, and A_z are the surface area of control volume ('p') perpendicular to the $x, y,$ and z directions, respectively. δx, δy, and δz are the distance between the control volume node and its neighbouring nodes along the $x,\ y,$ and z directions, respectively. ΔV is the control volume, and Δt is the time step size. The discretized equation (2.6) is derived for all the finite volumes in the computational domain, which gives the linear set of equations in the matrix form $A.T = B$. where A is the coefficient matrix and B is the column vector. The solution T is evaluated using the Gauss-Seidel method.

2.2.3 Immersed Boundary method and its implementation

In Figure 2.2, an irregular 2D tumor enclosed by healthy tissue is depicted to elaborate on the implementation of the immersed boundary method. The computational domain is discretized using the rectilinear grid, and the node (where the field variable, like temperature, is assumed to be situated) is located at the center of each control volume (rectangular grid). The grids are not conformal to the interface of tumor and healthy tissue. Therefore, the interface boundary splits the control volumes into the tumor and healthy tissue cells (as shown in Figure 2.2). The healthy and tumor tissue nodes are flagged by the scalar value $v = \vec{l}_i.\hat{\eta}_j$. where $\vec{l}_i$ is the vector distance of nodes from the nearest boundary element S_j, and $\hat{\eta}_j$ is the unit outward normal vector at that boundary surface element (Figure 2.2). The boundary elements (as shown in Figure 2.3(a)) are generated by discretization of the boundary into small elements (line elements for 2D boundary & triangular elements for 3D boundary surface). For triangular surface elements, the information from STL file is utilized to generate 3D surface. The size of these boundary elements is smaller than a cell's size. Each node is associated with the nearest boundary element, and this information is used to flag healthy and tumor tissue nodes [59,70]. If $v \geq 0$, the node lies in the healthy region; otherwise, the node lies in the tumor region (as described with the help of nodes $'p_2'$ and $'p_3'$ in Figure 2.3). Similar methodology have been described in literature to identify the inside and outside nodes with respect to the boundary of a domain [70,71].

Based on the flagging as described above, nodes in the tumor and healthy tissue are identified and represented as round and square nodes, respectively (Figure 2.2). The nodes have at least one neighbour node that lies in another region, is termed as immersed nodes, and the respective control volume is named the immersed boundary cells (IB cells). The unfilled nodes

(as shown in Figure 2.2 circle and square) in the tumor and healthy tissue domain represent the immersed nodes (N_1 to N_{15} in tumor side and N_1 to N_{19} in healthy tissue domain). The tumor side immersed node is denoted as IB-tumor, and the healthy region IB node is named IB-healthy. The intersection point between the boundary surface and the line joining the two adjacent IB- tumor, and IB- healthy is depicted as a 'cross' mark lies on one of the boundary elements, S_j. Like boundary element S_2 lies on the line joining IB-tumor node, rank 1 and IB-healthy node, rank 2, as shown in Figure 2.2. The discretized governing equation (2.6) is directly applied for each control volume except the IB cells in the tumor and healthy region. For IB cells, the coefficients of the neighbouring nodes that lie in another region are modified by implementing boundary conditions using the immersed boundary method, as discussed in the later sections.

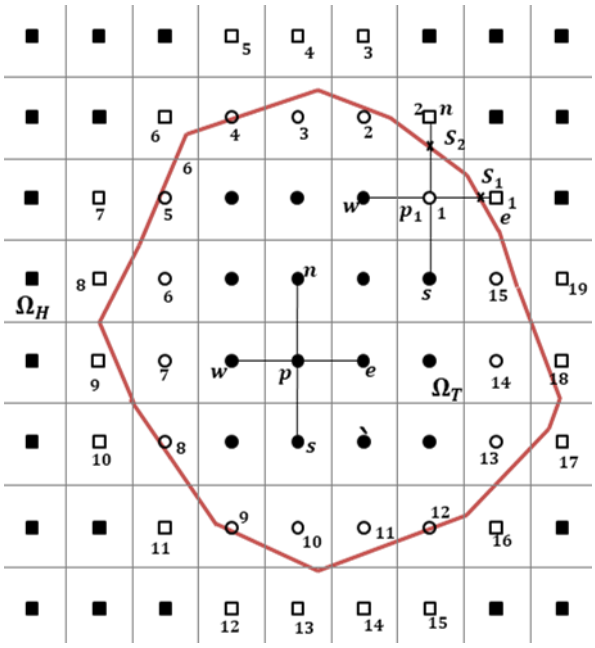

Figure 2.2. Implementation of IBM in the rectilinear grid.

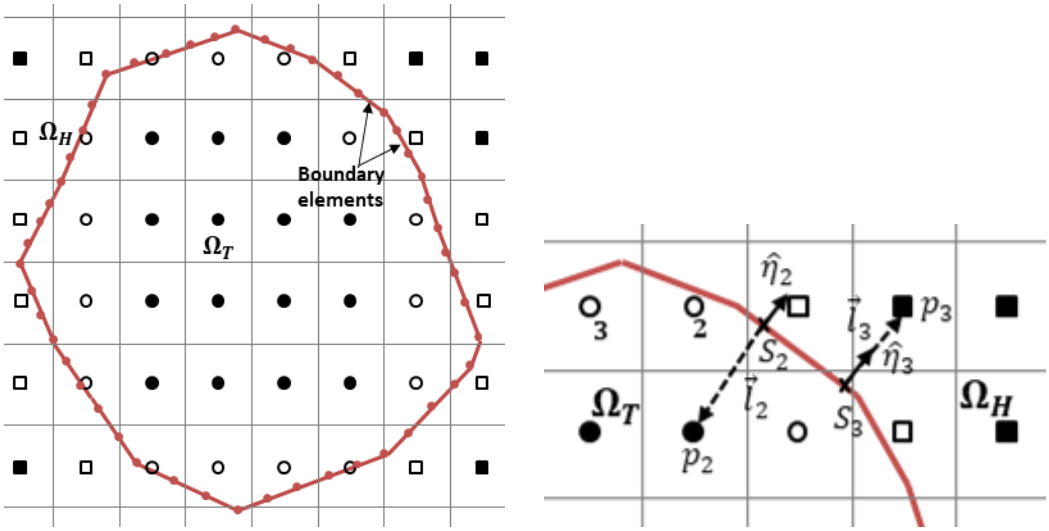

(a) **(b)**

Figure 2.3. Depiction of **(a)** the discritized boundary surface **(b)** the flagging of tumor and healthy tissue nodes

2.2.3.1 Implementation of Dirichlet boundary condition

Figure 2.4 describes the implementation of the Dirichlet boundary condition in one-dimension of the proposed IBM framework for the bio-heat application. The boundary surface (curve or line for 1D) intersects and divides the control volume into two parts. 'S' is the intersection point (lies on the boundary element) at the interface. The normalized distance between the boundary and the immersed node is $\overline{x_p S}/\delta x$. For the implementation of the Dirichlet boundary conditions, the IB-healthy (represented as a square node at 'e') temporarily works as a 'virtual or ghost tumor node' of the corresponding IB-tumor node to complete the relevant neighbouring node conditions. The boundary condition is enforced by calculating the field variable (such as temperature) using the forcing function that satisfies the boundary condition at the boundary surface 'S' (as shown in Figure 2.4). The value of the field variable at IB-virtual is extrapolated using the following expression (equation (2.8)).

$$T_e = \alpha_e T_p + \beta_e T_w + \gamma_e \qquad 2.8$$

where α_e, β_e and γ_e are the coefficients for the east-direction ghost node that are evaluated by applying the quadratic fit between the node $e - S - w$. In some IB nodes, when the boundary is very close to an immersed node such that $\eta \to 0$, the singularity arises by interpolating with the quadratic fit. Therefore, for that IB nodes, the linear fit is applied between the virtual node 'e' and 'w'. The linear fit affects the accuracy of the solution; however, the overall accuracy

remains the same because of the fewer such IB cells. Mark et. al. [72] have also reported nearly second order accurate scheme using linear fit for reconstruction the boundary for the simulation of complex fluid flow. The value of α, β and γ is expressed in the following generalized form (equation (2.9)).

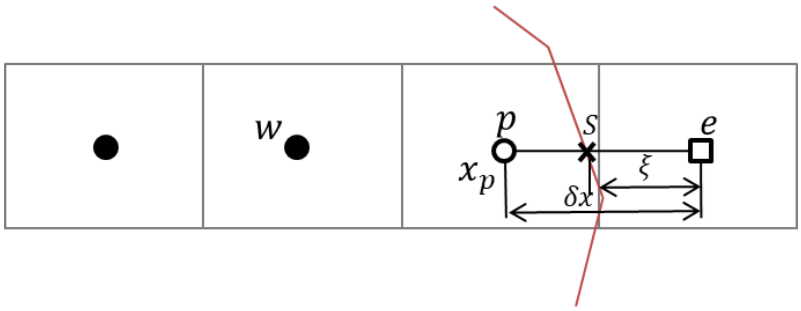

Figure 2.4. Depiction of the implementation of the boundary condition

$$\alpha = \frac{-2\xi}{1-\xi};\ \beta = \frac{\xi}{2-\xi}\ ;\ \gamma = \frac{T_s}{(1-\xi)(2-\xi)}\ \ (0 \le \xi \le 0.999)$$
$$\alpha = 0;\ \beta = -\frac{\xi}{2-\xi}\ ;\ \gamma = \frac{2\,T_s}{(2-\xi)}\ \ (\xi \to 1) \qquad 2.9$$

where $\xi = 1 - \overline{x_p S}/\delta x$, defines the normalized distance of the virtual node from the boundary (as shown in Figure 2.4). Accordingly, the coefficient of IB cells A_p, B_p and A_{nb} (A_e and A_w) are modified as follows (equation (2.10)):

$$\bar{A}_p = A_p - \alpha_e A_e$$
$$\bar{A}_w = A_w + \beta_e A_e$$
$$\bar{A}_e = 0 \qquad 2.10$$
$$\bar{B}_p = B_p + \gamma_e A_e$$

where $\bar{A}_p$, $\bar{A}_e$, $\bar{A}_w$ and $\bar{B}_p$ are the modified coefficients for the IB nodes. Similarly, the Dirichlet boundary condition on immersed healthy nodes is implemented by converting the corresponding neighbouring node in the tumor cell into a virtual node. In the literature, Das et al. [61] have discussed a similar methodology for different boundary conditions.

For implementing FV-IBM methodology, all nodes (both IB and regular nodes) and their corresponding neighboring nodes are stored in a data structure. IB and regular nodes are distinguished by tagging with distinct numbers. In tagging, the IB nodes in the tumor region

are labelled as '0', while the regular nodes are tagged as '1'. Following that, the normalized distance $'\xi'$ for each IB node with respect to its neighbouring virtual (ghost) nodes is evaluated. For two or three-dimensional geometry, the virtual (ghost) node may be more than one for each IB node. For example, the two-dimensional domain, as shown in Figure 2.2, IB node (p_1) has two ghost nodes, one on the east side and another on the north side. The normalized distance, ξ_e and ξ_n are calculated for p_1 with respect to east and north ghost node, respectively. Using the ξ values in each direction, the corresponding coefficients (α, β, and γ) of quadratic fit (equation (2.8)) are evaluated for each IB node. The α, β, and γ for each IB node are used to modify the coefficients of equation (2.6) using the description given in equation (2.10). The modified discrete equation of FV-IB for regular as well as IB nodes is illustrated in the equation (2.11). The stencil of this equation (2.11) is valid for any node (regular or IB) in two-dimensional domain as shown in Figure 2.2. Similarly, a general discrete equation implementing the FV-IB methodology could also be developed for the three-dimensional domain. The value of χ in equation (2.11) helps to incorporate the boundary conditions by modifying the coefficients of IB nodes. The value of χ is 1 if a neighbouring node in any direction lies outside the boundary (for IB nodes). Otherwise, the value of χ is 0 to produce the discrete equation for any regular node. Thus for $\chi = 0$, the stencil of the discrete equation is reduced to equation (2.6) (the discrete FV equation for any regular node in a cartesian domain). For the IB node like $'p_1'$ as shown in Figure 2.2, its neighboring east and north direction nodes are outside the boundary, while the west and south direction nodes are inside. Therefore, the east and north χ values which are denoted by. χ_e and χ_n, respectively is one, while the χ for west and south i.e. χ_w and χ_s, is 0. The simplified form of the discretized equation for the 'p_1' IB node is shown in equation (2.12). Conversely, the value of χ will be zero in all directions for the regular nodes like p (Figure 2.2), and its reduced discrete form is shown in equation (2.13). It can be seen that stencil of equation (2.13) is same as the equation (2.6).

$$\begin{aligned}\big(A_p - \chi_e\alpha_e\, A_e - \chi_w\alpha_w\, A_w - \chi_n\alpha_n\, A_n - \chi_s\alpha_s\, A_s\big)T_p^{t+1} \\ = ((1-\chi_e)A_e + \chi_w\beta_w\, A_w)T_e^{t+1} + ((1-\chi_w)A_w + \chi_e\beta_e\, A_e)\, T_w^{t+1} \\ + ((1-\chi_n)A_e + \chi_s\beta_s\, A_s)T_n^{t+1} + ((1-\chi_s)A_s + \chi_n\beta_n\, A_n)\, T_s^{t+1} \\ + B_p + \chi_e\gamma_e A_e + \chi_w\gamma_w A_w + \chi_n\gamma_n A_n + \chi_s\gamma_s A_s\end{aligned} \qquad 2.11$$

For p_1 IB node (as shown in Figure 2.2)

For east and north nodes: $\chi_e = 1$ and $\chi_n = 1$

For west and south nodes: $\chi_w = 0$ and $\chi_s = 0$

$$\begin{aligned}\left(A_p - \alpha_e\, A_e - \alpha_n\, A_n\right) T_p^{t+1} \\ = \left(A_w + \beta_e\, A_e\right) T_w^{t+1} + \left(A_s + \beta_n\, A_n\right) T_s^{t+1} + B_p + \gamma_e A_e + \gamma_n A_n\end{aligned} \quad 2.12$$

For regular node, the χ value in all direction is zero ($'p'$ node, shown in Figure 2.2)

$$A_p T_p^{t+1} = A_e T_e^{t+1} + A_w\, T_w^{t+1} + A_n T_n^{t+1} + A_s\, T_s^{t+1} + B_p \quad 2.13$$

2.2.3.2 Implementation of Conjugate heat transfer & Neumann boundary condition in biological medium

The conjugate heat transfer (CHT) is applied at the tumor and healthy tissue interface surface. The boundary condition is implemented at the surface point ('S_i', as shown in Figure 2.5). The following conjugate heat transfer equation is satisfied between tumor and healthy tissue using the IBM.

$$T_T|_S = T_H|_S \text{ and } -k_T \left.\frac{\partial T_T}{\partial \eta}\right|_S = -k_H \left.\frac{\partial T_H}{\partial \eta}\right|_S \quad 2.14$$

The interface temperature at the surface node is calculated with the help of four mirror nodes perpendicular to the surface element (two probes each in the tumor and healthy tissue region), as shown in Figure 2.5. These mirror nodes are positioned in the healthy and tumor tissue at a distance shown in equation (2.15). In equation (2.15), $\vec{d}_1$, $\vec{d}_2$, $\vec{d}_3$ and d_4 are the positions of m_1, m_2, m_3 and m_4 mirror nodes (as shown in Figure 2.5), respectively with respect global coordinate reference point. These mirror nodes are a distance of Δn and $2\Delta n$ on either side in the healthy and tumor zone. The position vector of mirror nodes is evaluated with the help of the position vector ($\vec{d}_{S_i}$) of the corresponding surface point 'S_i'(as shown in Figure 2.5) and is determined with the following equation (2.15).

$$\begin{aligned}\vec{d}_1 = \vec{d}_{S_i} - \Delta\eta \cdot \vec{\eta}_i \quad \vec{d}_2 = \vec{d}_{S_i} - 2\Delta\eta \cdot \vec{\eta}_i \\ \vec{d}_1 = \vec{d}_{S_i} - \Delta\eta \cdot \vec{\eta}_i \quad \vec{d}_2 = \vec{d}_{S_i} - 2\Delta\eta \cdot \vec{\eta}_i\end{aligned} \quad 2.15$$

where $\vec{n}_i$ is the normal vector of the respective surface element. The distance Δn can choose equal to grid size 'Δx'. The variation of distance Δn from Δx to $2\Delta x$ is reported by Das et al. [61] and shows that there are negligible effects on the solution by this variation. The surface

temperature is computed by expanding equation (2.14) with the Taylor series, as shown by the following relation (equation (2.16)).

$$T_S = \frac{k_H(4T_1 - T_2) + k_T(4T_3 - T_4)}{3(k_H + k_T)} \qquad 2.16$$

where T_1, T_2, T_3 and T_4 are the interpolated temperature at the mirror nodes m_1, m_2, m_3 and m_4, respectively. The field variable value at mirror nodes is evaluated with bilinear interpolation using the field variable value of each mirror node's surrounding four neighbouring nodes (enclosed by the dashed square boxes in Figure 2.5). For the 3D computational domain, trilinear interpolation is used to evaluate the value of field variables at the mirror node using the values of eight surrounding nodes. The details of the trilinear interpolation for a 3D domain have been described in the literature [73].

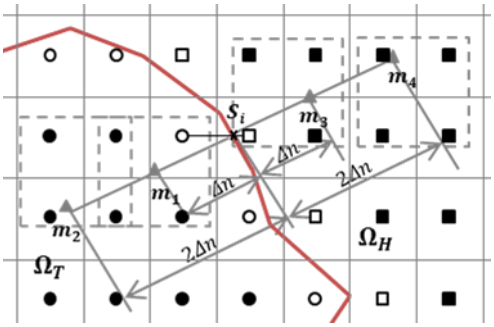

Figure 2.5. Illustration of the implementation of CHT conditions at the interface boundary.

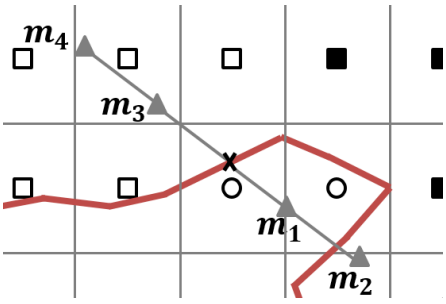

Figure 2.6. Depiction of the position of the mirror node for the special case.

For the sharp edges tumor-healthy tissue interface, the second mirror node for the tumor or healthy tissue side may lie in another region (as shown in Figure 2.6, m_2 lie in a healthy region). Thus, for this special case, the surface temperature is evaluated using the single mirror node on each side by equation (2.17). In the previous work, Das et al. [61] have also described

linear interpolation for complex geometries. Similarly, boundary reconstruction has also been reported by Municchi et al.[74] for fluid-particle interactions. They have applied the quadratic, linear and zeroth order interpolation based on the positions of mirror nodes [74].

$$T_S = \frac{k_H T_1 + k_T T_3}{(k_H + k_T)} \tag{2.17}$$

Once the value of surface elements is calculated, the implementation of the CHT boundary condition becomes similar to Dirichlet boundary conditions. Similarly, constant heat flux at the boundary and Neumann boundary condition is implemented with two mirror nodes normal to the boundary surface towards the computational domain. The discrete equation used to evaluate the surface temperature for constant heat flux at the boundary is given by equation (2.18).

$$\begin{gathered} -k \left.\frac{\partial T}{\partial \eta}\right|_s = \dot{q_S} \\ T_s = \frac{(4T_1 - T_2 - 2(\dot{q_S}/k)\Delta n)}{3} \end{gathered} \tag{2.18}$$

Similarly, for the special case, when the second mirror node lies in other regions for sharp surfaces, then the boundary condition is implemented with the single mirror node; the expression is described in equation (2.19).

$$T_s = \left(T_1 - (\dot{q}_{es}/k)\Delta n\right) \tag{2.19}$$

For the Neumann boundary condition, i.e., adiabatic boundary, the value of $\dot{q_S}$ become zero in equation (2.19). Thus, implementation of all the relevant boundary conditions using the sharp interface immersed boundary method and FVM methodology discussed to generate discretization methodology (FV-IBM). This FV-IBM is used to simulate bio-heat transfer (hyperthermia physics) in the complex tumor shape.

2.2.4 Implementation of external heat source (q_{es})

The distribution of an external heat source within tissue is dependent on the concentration and spatial spread of MNP. Previous computational studies for MNPH have used both uniform and Gaussian distributions of MNP in the tissue [32,40,44,54,64]. However, achieving perfectly uniform or Gaussian distributions in practice is challenging. However, many experimental

studies [9,19,30] have indicated that the distribution of MNP after injection tends to be heterogeneous.

Nevertheless, certain in-vitro and in-vivo experiments have indicated that a reasonably low injection rate of MNP can result in a distribution within the soft tissue that approximates a Gaussian profile [9,30]. The *in-vitro* study by Salloum et al. [30] on gel mimicking the soft tissues like liver has predicted that with low injection rate, a nearly uniform 3D Gaussian distribution of MNP can be achieved. Further, the *in-vivo* experimental studies by Salloum et al. [9] on animal tissue (nanoparticle injection in the muscle tissue of rat hind) have demonstrated that the curve fitted Gaussian distribution of SAR (Specific absorption rate) is in good agreement with experimental data during magnetic hyperthermia. Similarly, the *in-vivo* investigation by Attaluri et al. [19] on prostatic tumors in mice for magnetic nanoparticle hyperthermia obtained the bell-like temperature profile as a function of radial distance. The three-dimensional micro-CT image of tumor containing the nanoparticles by Attaluri et al. [19] shows that most of the MNP is confined near the injection site.

The power deposited in the tissue by the MNP is obtained by the product of SLP with the MNP spatial mass concentration $m(x_i, y_j, z_k)$ (equation 2.20). The SLP depends on both the frequency (f) and the amplitude of the magnetic field (H). In this study, the SLP for MNPH in the targeted tissue is considered based on an empirical model reported by Soetaert et al. [54] for bionized nanoferrite (BNF-starch nanoparticles). Soetaert et al. [54] (equation 2.21) derived the SLP(H) relationship by fitting a sixth-order polynomial approximation to the experimental data reported by Bordelon et al. [28], which involved a fixed frequency and variable magnetic field. Thus, the empirical model depends solely on the magnetic field strength.

$$q_{es} = SLP \times \frac{m(x_i, y_j, z_k)}{\Delta V} \tag{2.20}$$

where $m(x_i, y_j, z_k)$ denotes the MNP mass concentration in each control volume in rectilinear discretised tissue domain. Here, x_i, y_j, and z_k correspond to the positions of the center points of these control volumes in the global coordinate system along the *x*, *y*, and *z* directions, respectively.

$$SLP(H) = -1.5207e^{-8}H^6 + 5.1705e^{-6}H^5 - 6.2314e^{-4}H^4 + 0.0299H^3 - 0.3746H^2 + 2.2897H - 4.0033 \tag{2.21}$$

In our present research, we evaluated the SLP for a fixed frequency ($150kHz$) and varying magnetic field such that it ensures the safe application of MNPH. To maintain safety, the product of magnetic field strength and frequency should not exceed $5 \times 10^9\ Am^{-1}s^{-1}$ [26]. Further, the numerical formulation of external heat source distributions, which relies on the distribution pattern of MNP, is outlined for both uniform and Gaussian MNP distribution profiles as follows in Figure 2.7.

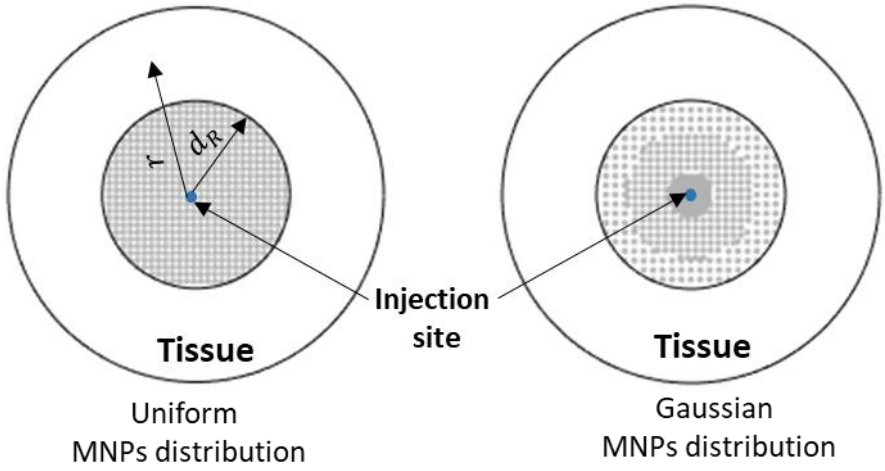

Figure 2.7. Depiction of the uniform and Gaussian MNP distribution profile in two-dimensional domain.

In the uniform MNP distribution, the mass of MNP in each control volume within the distributed region is same.

$$m(x_i, y_j, z_k) = \begin{cases} M.\dfrac{\Delta V}{V_d} & r \leq d_R \\ 0 & r > d_R \end{cases} \qquad 2.22$$

The total mass of MNP 'M' is distributed in a tissue volume 'V_d'. The total MNP distributed in the radial direction 'r' from the injection site is denoted by d_R. For the Gaussian MNP distribution profile, the following Gaussian function is used to model MNP mass, $m(x, y, z)$ in tumor models.

$$m(x_i, y_j, z_k) = M. \iiint_{\Delta V} \frac{1}{\sqrt{(2\pi)^3}\sigma_x.\sigma_y.\sigma_z} exp\left[\frac{-1}{2}\left\{\left(\frac{x_i - \overline{x}}{\sigma_x}\right)^2 + \left(\frac{y_j - \overline{y}}{\sigma_y}\right)^2 + \left(\frac{z_k - \overline{z}}{\sigma_z}\right)^2\right\}\right] dV \qquad 2.23$$

where, $\overline{x}, \overline{y}$, and $\overline{z}$ denote the location of MNP injection. σ_x, σ_y, and σ_z are the standard deviation along *x, y,* and *z* directions, respectively. The integrand can be expressed in the simplified form as follows.

$$m(x_i, y_j, z_k) = M. \iiint_{\Delta V} G(x, y, z) dV \tag{2.24}$$

The integration of equation (2.24) in each rectilinear control volume using the 4-point Gauss quadrature method yields the algebraic form as follows.

$$m = M.\frac{\Delta V}{8} \sum_{i=1}^{4} \sum_{j=1}^{4} \sum_{k=1}^{4} w_x(i) w_y(j) w_z(k) G(x_\lambda(i), y_\lambda(j), z_\lambda(k)) ;$$

$$x_\lambda = xi - \frac{\Delta x}{2} + (1+\lambda)\frac{\Delta x}{2};\ y_\lambda = yi - \frac{\Delta y}{2} + (1+\lambda)\frac{\Delta y}{2}; \tag{2.25}$$

$$z_\lambda = zi - \frac{\Delta z}{2} + (1+\lambda)\frac{\Delta z}{2}$$

where 'w' represents the weighing factors and 'λ' denotes the sample points. The subscript 'x', 'y' and 'z' denotes three-dimensional spatial direction.

2.2.5 Temperature-dependent blood perfusion coefficient (ω_b)

The blood perfusion term (ω_b) in the PBHT model varies with the temperature in tissue. The temperature-dependent blood perfusion is modelled using the first-order Arrhenius kinetic vascular stasis, as shown in equation (2.26) [75].

$$DS = 1 - \exp(-\Omega) \tag{2.26}$$

where, DS, the degree of vascular stasis that depends on the non-dimensional thermal damage parameter 'Ω' that is calculated by using the Arrhenius equation [76] is given as.

$$\Omega = \int_0^\tau A_a . exp\left(\frac{-E_a}{\mathrm{R}_u T(t)}\right) dt = ln\frac{C(0)}{C(\tau)} \tag{2.27}$$

where, A_a is the pre-exponential factor, which is the collision frequency of the molecules, and E_a is the activation energy barrier to activate and excite the molecules to initiate the reaction required for tissue damage. $\mathrm{R}_u = 8.314\ \mathrm{Jmol^{-1}K^{-1}}$ is the universal gas constant. $C(0)$ is the initial survival fraction, and $C(\tau)$, is the survival fraction after the heating time τ. The two

points trapezoidal numerical method (equation 2.28) is utilized to integrate the equation (2.27) and to evaluate the thermal damage and then a degree of vascular stasis by equation (2.26).

$$\Omega = \frac{\Delta t}{2} A_a \left[exp\left(\frac{-E_a}{\mathrm{R}_u T_p^t}\right) + exp\left(\frac{-E_a}{\mathrm{R}_u T_p^{t+\Delta t}}\right)\right] \quad 2.28$$

The temperature effect on perfusion coefficient relies on the value of the degree of vascular stasis (DS). The mathematical model proposed by Schutt et al. [77] for variation in perfusion rate (ω_b) with degree of vascular stasis (DS), is given as follows:

$$\omega_b = \begin{cases} \omega_{bi}(30DS + 1), (DS \leq 0.02) \\ \omega_{bi}(-13DS + 1.86), (0.02 < DS \leq 0.08) \\ \omega_{bi}(-0.79DS + 0.884), (0.08 < DS \leq 0.97) \\ \omega_{bi}(-3.87DS + 3.87), (0.97 < DS \leq 1) \end{cases} \quad 2.29$$

where, ω_{bi} is the initial perfusion rate (at core body temperature) before the application of MNPH. This relationship is utilized to estimate the effect of temperature on the blood perfusion rate of tissues during MNPH. Table 2.1 contains the value of ω_{bi} for tumors as well as healthy tissue. The blood perfusion in the tumor as well as healthy tissue is considered as homogeneous. Many investigations have described the non-uniform vascularisations in the tumor. Studies describe that dead (necrotic) cell regions develop at the tumor core with tumor proliferation [78,79]. Soni et al. [79] investigated the influence of non-uniform blood perfusion on heat transfer. It shows the negligible heat transfer difference for moderate heterogenous and homogenous blood perfusion rates ($0.0017\ \mathrm{s}^{-1}$). The blood perfusion considered in this study is $0.0025\ \mathrm{s}^{-1}$ (liver tumor) [78], which is close to the moderate perfusion rate. Thus, considering homogeneous blood perfusion is a reasonable assumption for considered blood perfusion rate in the tumor tissue.

2.2.6 Thermophysical properties of tissue

The simulation of Penne's bioheat model predicts the spatial and temporal temperature distribution in the tissue. The accuracy of the bio-heat simulation results depends on various input parameters of equation 2.1, which includes the thermophysical properties of tissues. Human soft tissue contains approximately 70-86% water content [80]. Owing to the high concentration of water, some of the thermophysical properties of tissue such as thermal capacity and thermal conductivity is similar to the water [21]. However, many studies have explored a linear relation between thermal properties of tissue and temperature. Review article

by Bianchi et al. [81], have reported that thermophysical properties of soft tissues remain relatively constant up to around 90 ℃. Thus, in the present study, thermophysical properties of healthy and cancerous liver tissue have been considered temperature independent as provided in Table 2.1.

Table 2.1. Thermophysical properties of tissue (tumor as well as healthy tissue), MNP and treatment parameters are considered in this study [28,54,78,82,83].

Parameter	Value	Parameter	Value
ρ^*	1060 $\mathrm{kgm^{-3}}$	$\omega_{bi-healthytissue}$	0.0064 $\mathrm{s^{-1}}$
C_p^*	3500 $\mathrm{Jkg^{-1}K^{-1}}$	$\omega_{bi-tumor}$	0.0025 $\mathrm{s^{-1}}$
k^*	0.53 $\mathrm{Wm^{-1}K^{-1}}$	A_a	2.984×10^{80} $\mathrm{s^{-1}}$
ρ_b	1000 $\mathrm{kgm^{-3}}$	E_a	5.064×10^5 $\mathrm{Jmol^{-1}}$
C_b	4180 $\mathrm{Jkg^{-1}K^{-1}}$	f	150 kHz
$q_{m-Healthytissue}$	4200 $\mathrm{Wm^{-3}}$	H	12 $\mathrm{kAm^{-1}}$
$q_{m-tumor}$	42000 $\mathrm{Wm^{-3}}$	MNP size (d_{MNP})	$15 - 20$ nm
T_a	310 K		

*value of these properties are the same for both tumor as well as healthy tissue.

2.3 Results

The proposed FV-IBM framework for the bioheat problem is first applied to solve the diffusion equation in the curvilinear domain. Then this methodology is applied to solve the steady and transient Penne's bioheat model in the spherical tumor. The numerical results generated FV-IBM methodology for the considered test cases are compared with the analytical and previously reported numerical solutions. The FV-IBM scheme is then utilized to compute the temporal-spatial temperature profile induced due to magnetic nanoparticle hyperthermia therapy in a complex tumor model. The tumor model is created from the DICOM images (from the repository of the cancer imaging archive (TCIA) [84]) for the liver tumor . The temperature distribution is commutated in the complex-shaped real liver tumor by applying the uniform and Gaussian heat distribution source.

2.3.1 Validations

2.3.1.1 Test case 1

The first test case chosen for the verification of the proposed FV-IBM framework is the diffusion equation ($\nabla^2 T(r,\theta) = 0$) in a 2D curvilinear domain, as shown in Figure 2.8a. The

boundary conditions on the surface AB, CD and BD are $T(r,0) = T(r,\pi/2) = 1$, and $T(r_2,\theta)$=0, respectively. The Neumann boundary condition on surface AC is $dT/dr\ (r_2,\theta) = 0$. The numerical results are compared with the analytical solution [85,86]. The difference between the analytical solution & numerical results (numerical error) by FV-IBM is calculated in terms of RMS (root mean square error) error, 'ε' as given by equation (2.30).

$$\varepsilon = \sqrt{\frac{\sum_{i=1}^{N}\left(T_{i,num} - T_{i,exact}\right)^2}{N}} \qquad 2.30$$

where 'N' is the total number of immersed and regular nodes in the computational domain. Subscript $'num'$ and $'exact'$ represent the numerical and analytical solution. The RMS error generated at different grid sizes ranging from 10×10 to 80×80 is tabulated in Table 2.2. From this Table, a plot between error versus grid size is generated (Figure 2.8(b)). The slope of the grid size versus the RMS error (ε) line (Figure 2.8b), is approximately 1.53. Thus, we can say, that the order of accuracy of the FV-IBM method for the diffusion equation in the curvilinear domain is close to 2.

Table 2.2. RMS error by comparing the analytical and numerical solution for test case 1.

Number of grids	Grid size (mm)	RMS error
10×10	0.1	0.1187×10^{-1}
20×20	0.05	0.4141×10^{-2}
40×40	0.025	0.135×10^{-2}
80×80	0.0125	0.476×10^{-3}

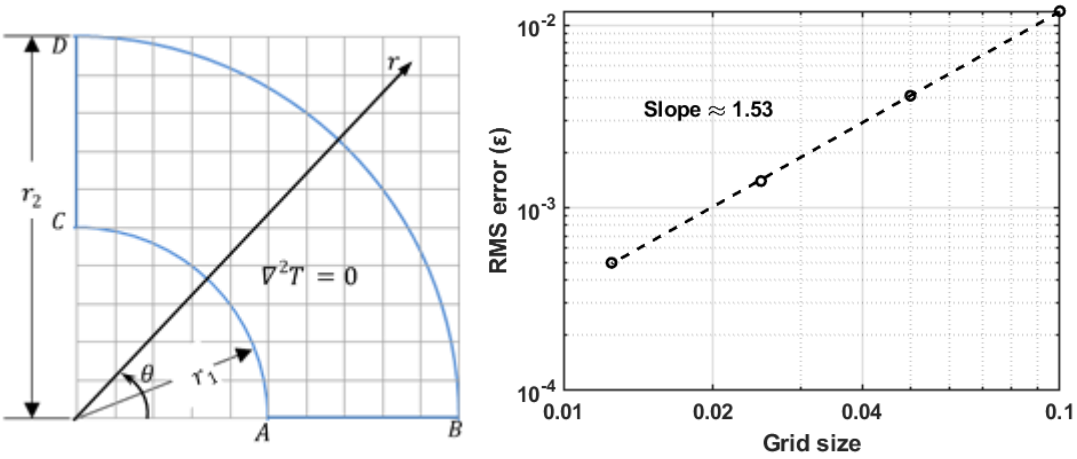

(a) **(b)**

Figure 2.8. **(a)** Depiction of the curvilinear domain and **(b)** order of accuracy of FV-IBM methodology in curvilinear geometry.

2.3.1.2 Test case 2

In test case 2, the FV-IBM framework is applied to solve the bioheat model in the spherical-shaped tumor enclosed by healthy tissue as shown in Figure 2.9. For the validation of developed methodology, results are computed with analytical and previously reported numerical results for steady as well as unsteady cases.

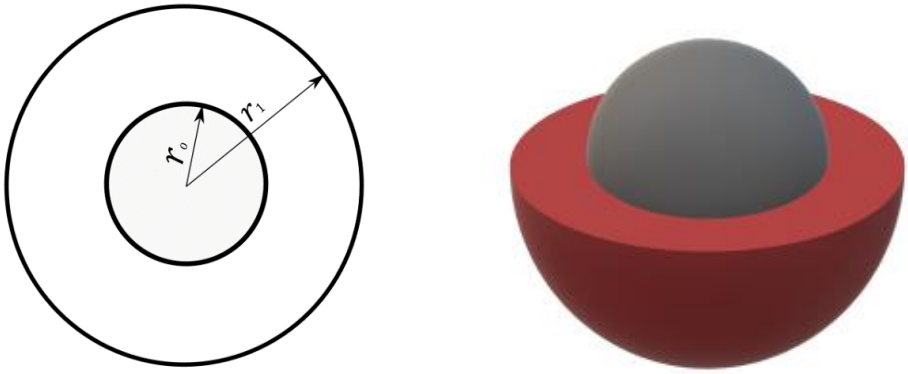

(a) **(b)**

Figure 2.9. Depiction of a tumor model in (a)- Section view; (b) perspective view

Steady test case

In this case, a Gaussian heat source (in terms of specific absorption rate (SAR)) as a hyperthermia applicator is applied to the tumor. The complete model (as shown in Figure 2.9) is composed of only tumor tissue. The size of the tumor tissue i.e., $r_0 = r_1$ is 30 mm. The

boundary surface temperature is given 37 ℃. The details of its analytical solution are provided by Salloum et al. [20]. The SAR equation in the spherical tumor tissue is given as:

$$SAR = B.e^{-r^2/R^2} \tag{2.31}$$

where $B = 800\,\mathrm{kW/m^3}$ and $'R' = 5$ mm is the maximum radial distance up to which the heat source is distributed.

The steady-state temperature profile developed in the tumor model due to heat source varies in the radial direction. It depends upon the value of SAR and its distribution in the tumor tissue (equation (2.31). The steady-state temperature profile along the radial direction from the tumor centre is shown in Figure 2.10a for the mesh of $64 \times 64 \times 64$. The comparison reflects that the numerical results are in good agreement with the analytical solution. The variation of the numerical solution from the analytical is again computed in terms of RMS error for different grid sizes. The slope of the RMS error line indicates that the FV-IB scheme is nearly the second-order accurate scheme for solving the bioheat model (as shown in Figure 2.10b).

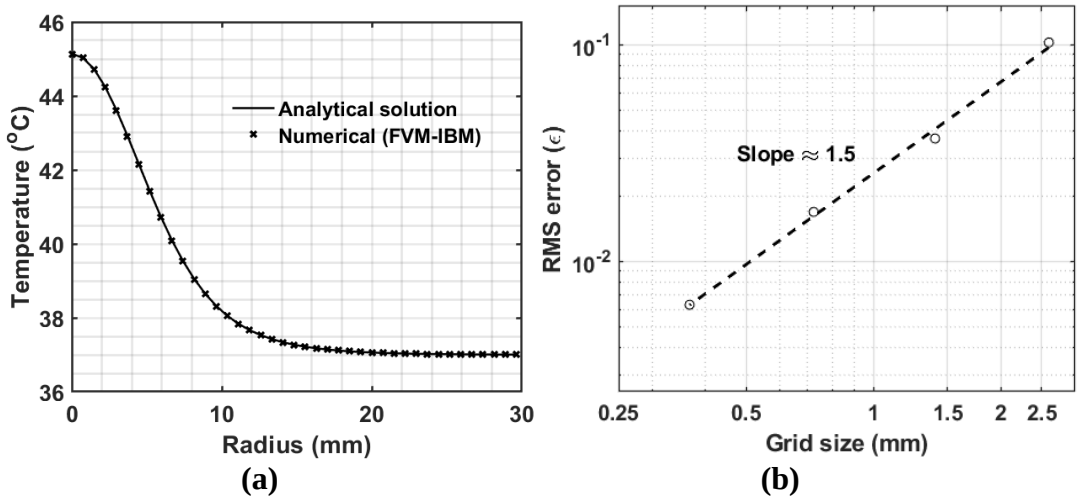

Figure 2.10. (a) Comparison of temperature with analytical solution [20] for steady-state case **(b)** Depiction of the variation of RMS error with grid size for bioheat model using FV-IBM scheme

Unsteady test case

In this problem, uniformly distributed magnetic nanoparticles (MNP) under the action of an alternate magnetic field in the tumor tissue work as hyperthermia applicators. The surface of surrounding healthy tissue is maintained at core body temperature, i.e., 37℃. The tumor and healthy tissue radius (i.e., r_0 and r_1) is 5 mm and 15 mm, respectively (as shown in Figure

2.9). Two types of MNP (9nm FCC FePt and 19nm magnetite) are used as magnetic heating sources. The thermophysical properties of the tumor, as well as healthy tissue and perfusion rate, are given in Lin & Liu [87]. The volume fraction Ø (ratio of MNP volume to the MNP distributed tumor volume) for both MNP is 2×10^{-5} [87]. The magnetic field parameters with 50 mT field strength and 300 kHz frequency are applied for MNPH. The resulting heat generation by each type of MNP is calculated using the Rosensweig model [88]. Under the action of external magnetic field MNP work as a heat source, and the temperature in the tumor model increases with time. Results are produced with a grid size of $64 \times 64 \times 64$and compared with the previous work [87] for two-time positions 50 and $100s$. Again, the results are plotted along the radial direction of the tumor model (Figure 2.11) for both the MNP as a heat source. For both the times 50 and $100s$, the temperature plots are in good agreements with the results of Lin and Liu [87]. Thus, developed methodology is also successfully applied for tumor models having time-dependent temperature increments.

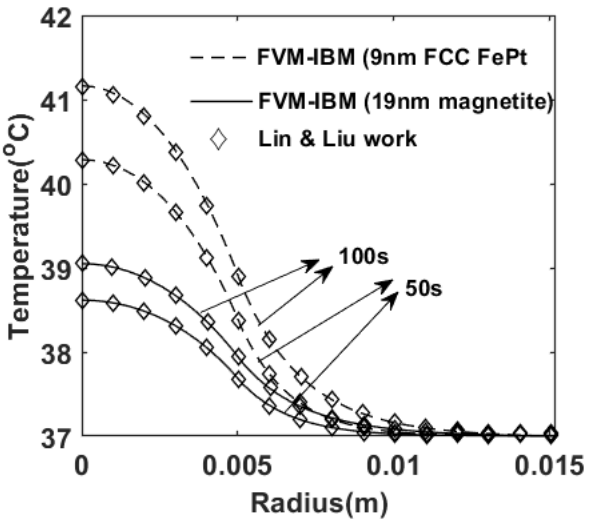

Figure 2.11. Comparison of temperature in the radial direction with Lin and Liu [87] for test case 2 (transient problem)

2.3.2 Implementation of the present numerical scheme in the 3D liver tumor model

The FV-IBM framework is now used to simulate magnetic nanoparticle hyperthermia in a real 3D liver tumor. The open-source 3D slicer software is used to extract the tumor (pale yellow color) as well as the surrounding healthy portion of the liver (blue color) from the CT images of the abdomen [84], as shown in Figure 2.12. This software (3D slicer) is used for the segmentation and then manual smoothing of the surfaces of the liver and tumor. The tumor and surrounding liver model surface mesh are stored in stereolithography (STL) format. An in-

house MATLAB function is used to read the STL file to apply the FV-IBM framework. The intestine fluid is considered around the liver vicinity (Figure 2.13). The properties of the intestine fluid are considered the same as blood. Figure 2.13 shows that the tumor is developed on the surface of the healthy liver. The geometric parameters of the tumor are described in Table 2.3. The L_{max-x}, L_{max-y}, and L_{max-x} is the maximum tumor length along the x, y and z-axis, respectively. The total volume of the tumor is nearly $2.52\ \text{cm}^3$. For magnetic hyperthermia application, a total amount of 25.2 mg of bionized nano ferrite (BNF-starch) MNP material is injected into the centroid of the tumor mass. This MNP mass is with reference to in-vivo work by Attaluri et al. [19] for MNPH on prostate tumor in mice.

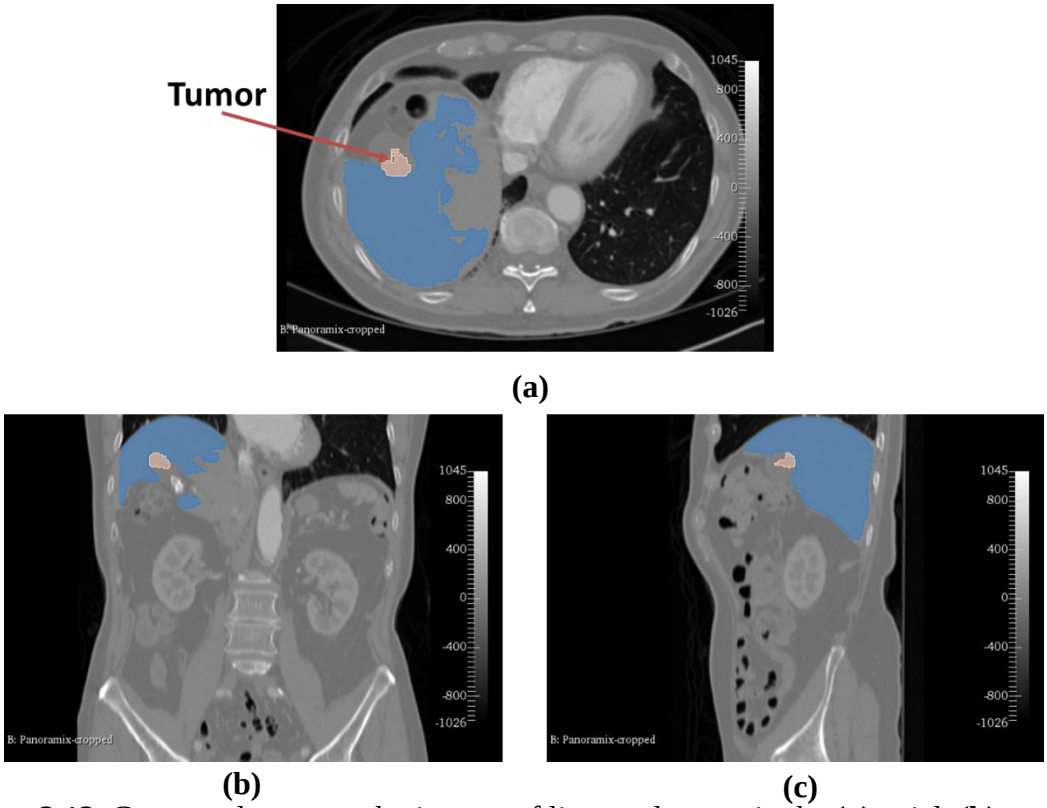

Figure 2.12. Computed tomography images of liver and tumor in the **(a)** axial, **(b)** coronal, and **(c)** sagittal plane

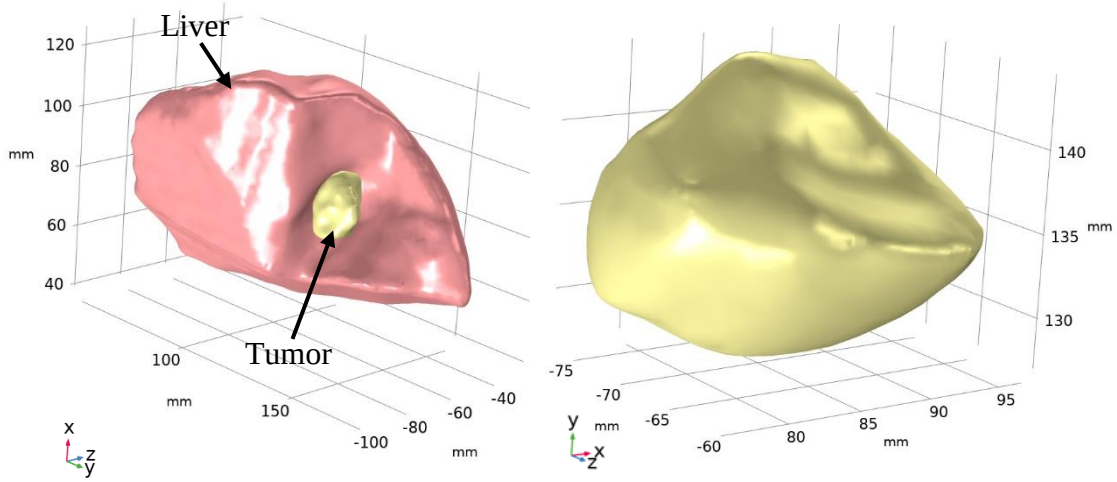

(a) **(b)**

Figure 2.13. The 3D image of **(a)** tumor and surrounding liver **(b)** tumor, extracted with 3D slicer software

Two MNP spread (uniform and Gaussian) are considered for this liver tumor model during magnetic hyperthermia. For uniform MNP distribution, the MNP volume fraction Ø is constant, and its value is 0.0346 within the 140 mm^3 volume. In the second scenario, we have considered the isotropic Gaussian distribution pattern with MNP spread parameterized with $3\sigma = 3.2$ mm, which makes more than 98% of MNP within the 140 mm^3 of tumor volume. The heat produced by the MNP hyperthermia propagates to the liver and intestine fluid. The conjugate heat transfer as a boundary condition is applied at the interface of tumor-liver tissue and tumor-intestine fluid. The outer surface of the surrounding intestine fluid is at core body temperature i.e., 37 ℃.

Table 2.3. Geometric properties of tumor

Volume	Surface area	L_{max-x}	L_{max-y}	L_{max-z}
2.52 cm^3	9.93 cm^2	2.1 cm	1.74 cm	1.64 cm

2.3.3 Comparison of results with COMSOL Multiphysics

The therapeutic time is 20 minutes for both the uniform as well as the Gaussian source distribution cases [19]. The application of MNPH therapy produces heat in the tumor tissue. The numerical solution of the FV-IBM solver is compared with fine grid computational results produced by COMSOL Multiphysics 5.6 for the simulation of MNP hyperthermia on the same tumor model & hyperthermia parameters. The computational grid structure for the FV-IBM solver is uniform and non-conformal to the physical domain (tumor, tissue, and intestine

fluid).as shown in Figure 2.14a. The grid size of each cubical element is 0.6 mm. The boundary condition (conjugate heat transfer) between the interface of the tumor and healthy tissues as well as between intestinal fluid and liver tissue, is implemented through IBM framework. However, in COMSOL an unstructured tetrahedral body-fitted mesh is used to discretize the complex physical domain (as shown in Figure 2.14b). The non-uniform, unstructured grid size varies from minimum to maximum in the tumor region is 0.029 to 5.04mm.

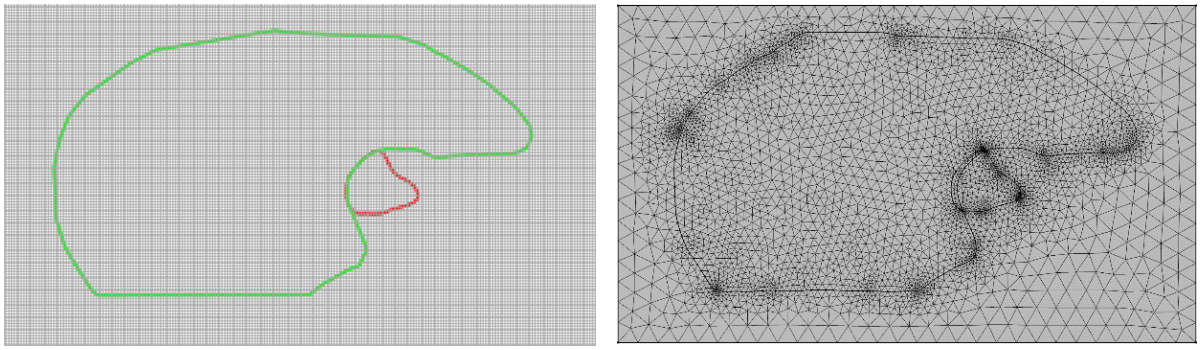

(a) **(b)**

Figure 2.14. Depiction the meshing in tumor **(a)** non-conformal in FV-IBM and **(b)** conformal in COMSOL.

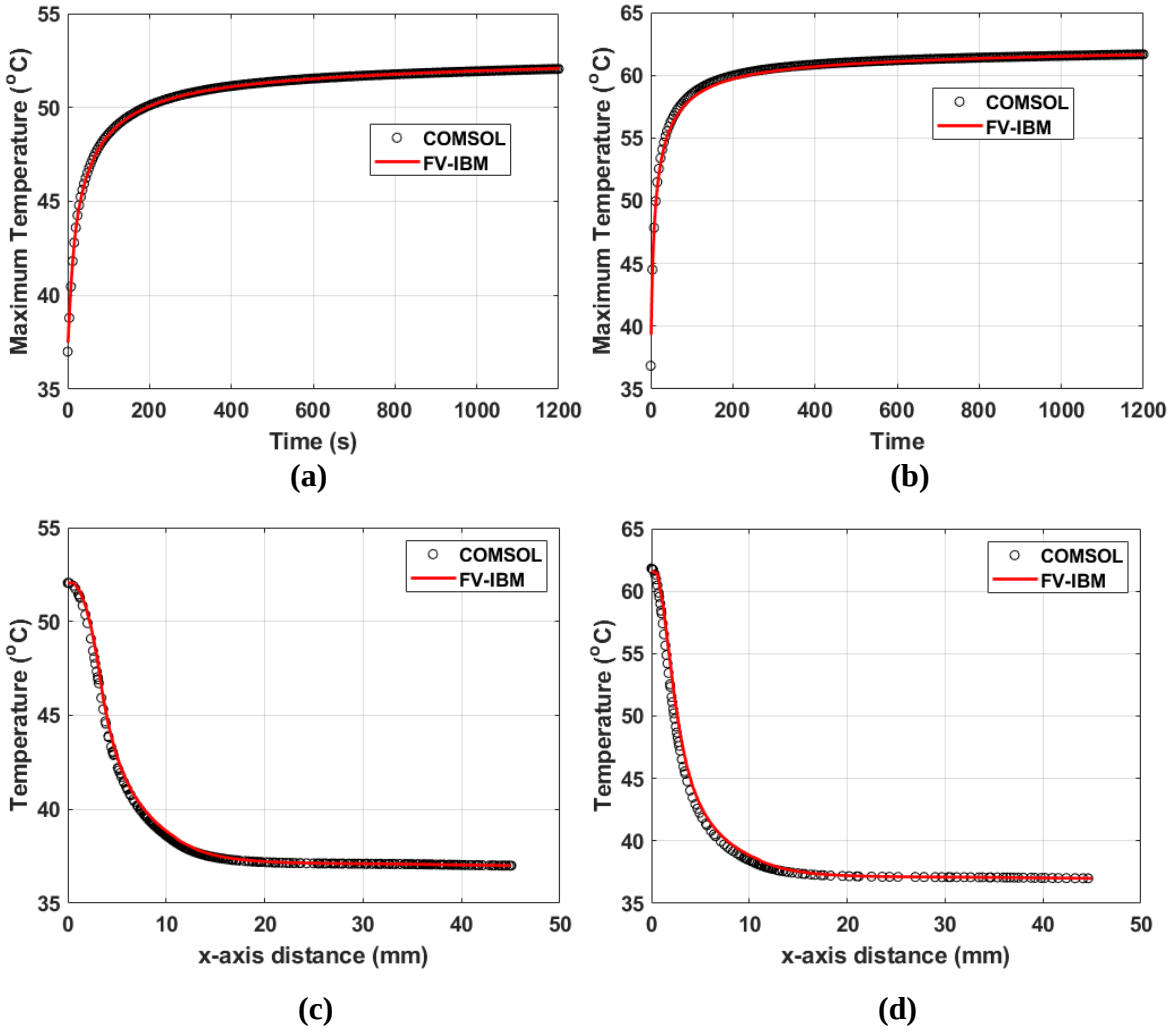

Figure 2.15. Comparison of temperature elevation produced by FV-IBM and COMSOL **(a**, **c)** uniform **(b**, **d)** Gaussian source at the injection site and along the x-axis line, respectively.

Figure 2.15 compares temporal and spatial temperature elevation for uniform and Gaussian MNP distribution by FV-IBM methodology and COMSOL solution. The comparison shows that the FV-IBM solver's temperature profile agrees well with the temperature profile produced by fine grid COMSOL Multiphysics software for both uniform and Gaussian sources.

2.3.4 Spatial Temperature profile in the tumor by FV-IBM methodology

The steady-state temperature isotherms produced by FV-IBM after the 1200s for both cases are shown in Figure 2.16. The temperature contours are presented on the axial, coronal, and sagittal planes that pass through the centroid of the tumor (injection site). The tumor and healthy surface are distinct, with red and green colors, respectively, as shown in Figure 2.16.

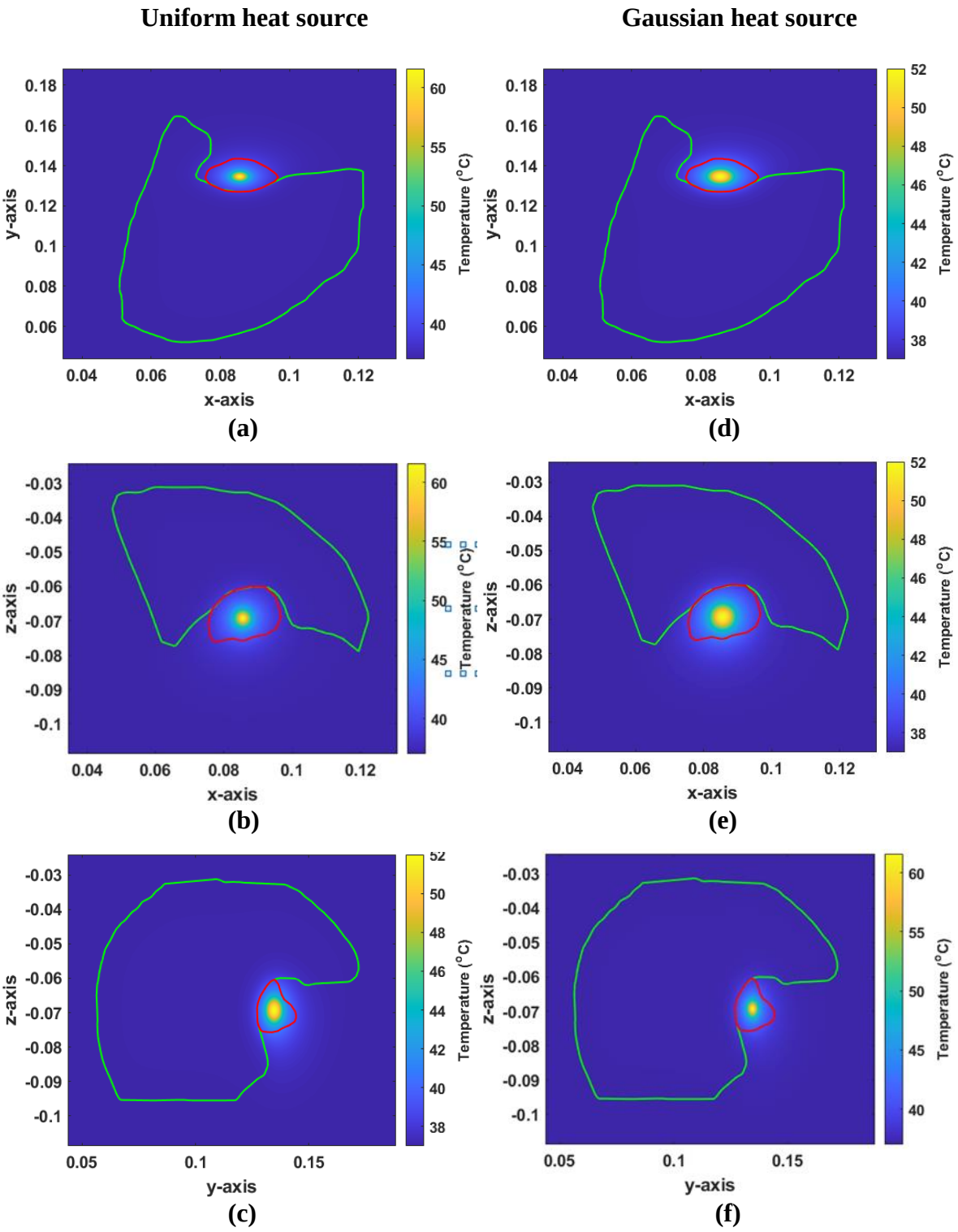

Figure 2.16. Depiction of the isotherms in the mutual perpendicular plane passes to the injection site of the tumor in **(a**, **b**, **c)** uniform and **(d**, **e**, **f)** Gaussian distribution source.

The maximum temperature in uniform and Gaussian distribution sources at the injection site is approximately 52.08℃ and 61.64℃, respectively. The temperature asymptotically reduces from the injection site to the core body temperature. The higher temperature in the Gaussian source than in the uniform is because of the dense MNP

concentration near the injection site. However, the MNP concentration reduces sharply from the injection site in the Gaussian source.

A detailed quantitative description of the heat penetration extent in the tissue is shown in Figure 2.17. Plots in Figure 2.17 describe the steady-state spatial temperature variation along $x,\ y,$ and z-axis, respectively, from the injection site. The tumor boundaries (TB) in the plots are shown by the vertical dotted lines and represented as TB_x, TB_y, and TB_z along $x,\ y,$ and z-direction, respectively. The horizontal dotted line in these Figure 2.17(a-c) describes the tumor volume above the minimum therapeutic temperature (MTT), which is 43℃. The MTT is the threshold temperature limit to initiate the thermal damage to the tissue.

It can be observed that the temperature near the injection site in the tumor in both cases is above the therapeutic range. After the 1200s, nearly 20% of total tumor volume in uniform source and 16.2% in Gaussian distribution source is above the MTT line. The Gaussian and uniform heat source distribution patterns are isotropic and ideal. However, in real tissue, MNP distribution is affected by various factor and have anisotropic and heterogenous pattern [30]. It is also shown in Figure 2.18 by comparing the temperature profiles of the present study and the experimental work of Attaluri et al. [19]. The authors have conducted *in-vivo* investigation of MNPH on the prostatic tumor in mice. The tumor volume in mice is $2.57\ \mathrm{cm}^3$ with a standard deviation of $\pm 1.26\ \mathrm{cm}^3$. A total amount of 25.2 mg of MNP has been injected at different infusion rates. Heat is produced for 20 min in a tumor by $3\ \mathrm{kA/m}$ magnetic fields and 190 kHz frequency. However, the pattern of MNP distribution with its quantity and estimation of SAR generation in the tumor is not elaborated. The temperature profile reported by Attaluri et al. [30] at an injection rate of $20\ \mu\mathrm{L/min}$ in mice during therapy is reproduced in Figure 2.18. Similar MNP volume distribution at an injection rate of $20\ \mu\mathrm{L/min}$ is considered in the present work. It can be observed from Figure 2.18 that the maximum temperature of Attaluri work lies between the Gaussian and uniform heat source distribution, and the maximum temperature variation is close to the Gaussian source. However, the error associated with the idealized SAR and MNP distribution considered in this study causes a difference between the numerical and experimental temperature profiles. Nevertheless, the temperature distribution obtained from FV-IBM is able to capture the nature of the temperature profile during MNPH. Concluding, the comparisons show that the FV-IBM framework for the bioheat model can be efficiently applied to any complex-shaped tissue.

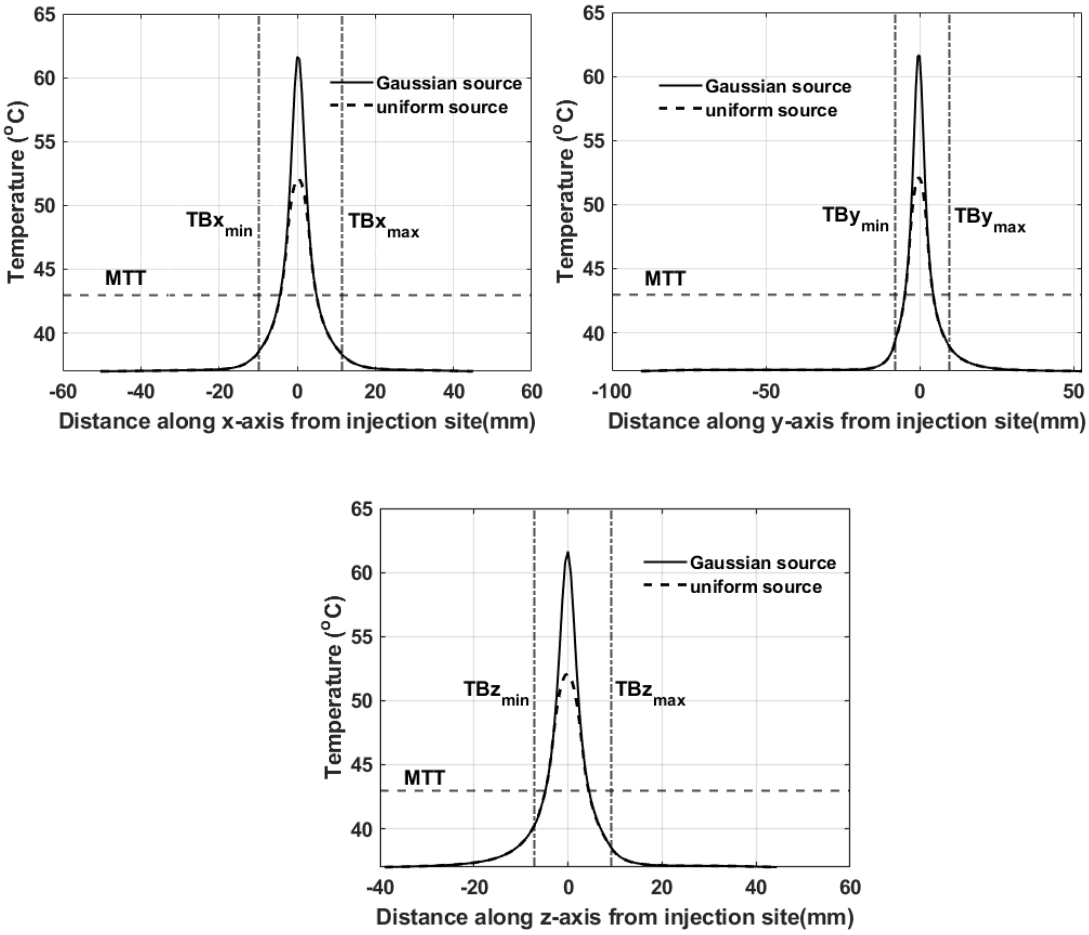

Figure 2.17. Comparison of temperature variation along the x, y, and z axis from the injection site for Gaussian and uniform heat source

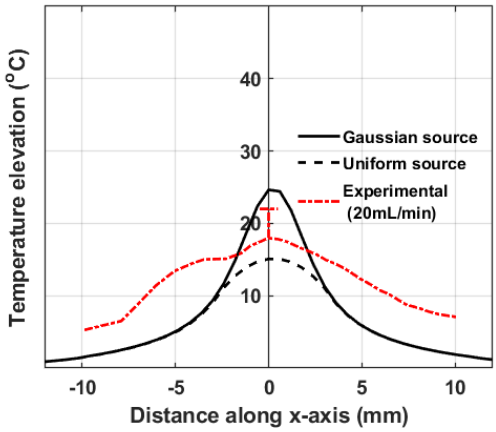

Figure 2.18. Comparison of the temperature profile of the Gaussian and uniform distribution heat source and Attaluri et al. [19] experimental work

2.4 Discussion and Conclusion

The coupled FV-IB method has been developed to discretize Penne's bioheat model for investigating MNPH therapy in complex 3D tumors. The developed scheme is nearly second-

order accurate. The developed framework for solving the bioheat model produces quite accurate results for cases with different heating sources that produce steady and transient temperature distribution in the spherical tumor model.

The investigation of MNPH therapy using the FV-IBM framework in a real liver tumor model is done with both uniform and Gaussian distribution MNP sources. The comparison of temperature profile produced by FV-IBM methodology with results produced by fine grid COMSOL Multiphysics demonstrates the efficacy of FV-IBM methodology for bio-heat applications. The comparison of the results with experimental work shows that results produced by FV-IBM can capture the physics of bio-heat transfer in complex-shaped tumors. Thus, a numerical scheme based on the FV-IBM methodology is derived and successfully applied for bio-heat application in complex tumor tissue morphology.

2.5 Closing Remarks

In the present work, we have developed the FV-IB framework for computing the bioheat equation in a 3D complex tumor model with non-body conformal Cartesian grids. Extensive validation studies are performed by comparing the FV-IB solution with analytical and other solutions. It shows the scheme is nearly second-order accurate and is successfully applied for steady and transient cases. The scheme is also applied successfully to simulate MNPH in the 3D real complex tumor model imported from the CT scan image.

Chapter 3

Parameterizing the effects of tumor shape in magnetic nanoparticle thermotherapy through a computational approach

3.1 Introduction

In this chapter, the effects of tumor morphology on MNPH, has been extensively analysed. To investigate the effect of tumor shape, an array of tumors having different tumor morphology are generated using 2D symmetric and asymmetric profiles. The morphology of the considered tumors are changed by altering their aspect ratio. Therefore, for a fixed tumor volume, various tumor shapes having different surface areas are generated. These tumors are kept under similar MNPH applicator conditions (MNP dose and AMF intensity). The heat transfer in tumor phantoms during MNPH is estimated using PBHT equation (equation 2.1). The PBHT equation is numerically solved using the developed FV-IB framework in the tumor models to evaluate the spatial and transient rise in the temperature field due to MNPH. The distribution of MNP mass in tumor tissue after its injection is considered to be as Gaussian at the centroid of tumor. The specific power loss (SLP) of the MNP in the targeted tissue during MNPH is based on the model reported by Soetaert et al. [54] for bionized nano ferrite (BNF-starch nanoparticles).

3.2 Material and Methods

3.2.1 Physical model

Tumors can have any irregular shape, however, tumor masses are broadly categorized into round, oval, and irregular shapes [39,89]. A Recently reported study by Byrd et al. [39] characterising the shape of breast cancer based on supine MRI data, shows that most of the tumors are not spherical. Using geometrical equations for 3D reconstruction, they found that 34% of tumors were discoidal (oblate), 29% segmental (prolate), 19% spherical and 18% irregular, based on the supine MRI of 83 breast cancer patients [39]. The classification of tumor morphology is defined by fitting each tumor shape into the smallest possible ellipsoidal [39] (as shown in Figure 3.1). Geometrical parameters used to categorised the tumor shapes are sphericity ($\psi = \pi^{1/3}(6V_{tumor})^{2/3}/A_{tumor}$) and isocentricity (Isocentricity = $(d_{max} - d_{min})/d_{max}$ [39]. Where, *V* is the computed tumor volume, *A* is the corresponding surface area, and d_{max} and d_{min} are the maximum and minimum tumor extents from the center of the tumor, respectively. Therefore, in line with the broad category of tumor shapes, both symmetrical (spherical and ellipsoidal), as well as asymmetrical (egg) shapes, as shown in Figure 3.2, are

considered for the investigation of effects of tumor morphology on MNPH. The ellipsoidal category of tumor is further sub-categorized into oblate (disc type) and prolate (rod type) shaped tumors (Figure 3.2). The volume of all these tumors is equal to the reference spherical tumor model, represented as '*S*' in Figure 3.2. The radius (R_s) of the referenced spherical tumor model is 1 cm i.e., its size is 2 cm. This size is in reference to the first stage of malignant liver tumors [90]. However, the maximum length of other tumors is greater than 2 cm. Tumors can be invasive in any direction due to several reasons [91]. As per Gibbs Thomson's relation, the nutrient concentration gap across the tumor-tissue interface is proportional to the curvature of the tumor. Nutrients act as a source of energy and this energy is required by the cell on the interface to preserve the cell-to-cell adhesion to maintain the compactness of the tumor. Reduction in the cell-to-cell adhesion forces makes tumor invasive and produces the rough surface at the tumor boundary [92,93]. Thus, the tumor with high local curvature such as egg, prolate, and oblate would most likely be more aggressive and invasive. In the considered tumor models (as shown in Figure 3.2), spheroid tumor proliferates in different directions, symmetrically (prolate and oblate) as well as asymmetrically (egg-shaped). However, different degree of invasion changes the morphology of tumors.

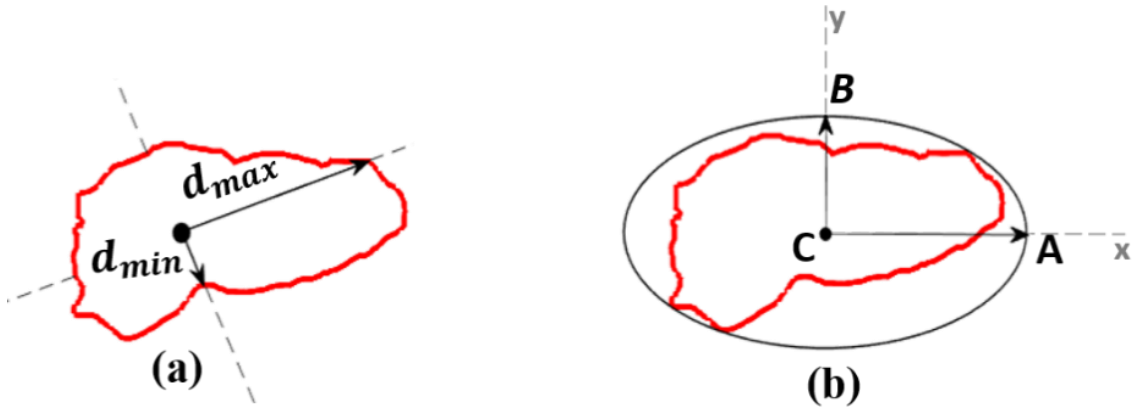

Figure 3.1. (a) d_{max} and d_{min} is the maximum and minimum tumor extent from central point, respectively **(b)** Ellipsoidal fit to an arbitrary tumor shape with measured CA and CB diameter along two primary axes.

Changing the morphology (aspect ratio) of the tumor increases its surface area. This morphological aspect of the tumors is quantified in terms of the shape factor (ζ). The definition of shape factor is based on the criteria established by the World Health Organization (WHO) to measure a tumor's size, which states that " Measurement of the size of a tumor or lesion that is used to evaluate the result of a therapy is based on the maximum diameter(s) and second transverse diameter(s), at a right angle to the first and in the same plane" [94]. Therefore, in

our study, it is defined as the ratio of the maximum to the minimum spread of tumor tissue $(i.e. \zeta = AC/BC)$ along the longitudinal and transverse axis, from the centroid, as shown in Figure 3.2. The definition of shape factor is similar to the geometrical parameter 'isocentricity' that was used to define the shape of tumor in the previous study [39]. An array of tumor shapes (see Figure 3.2) is produced to investigate the effects of shape on MNPH. In each category of tumors, the surface area of the tumor is successively increased by changing the shape factor (ζ). However, the limiting tumor model in all the categories has a maximum increase of 20% surface area with respect to the spherical reference model.

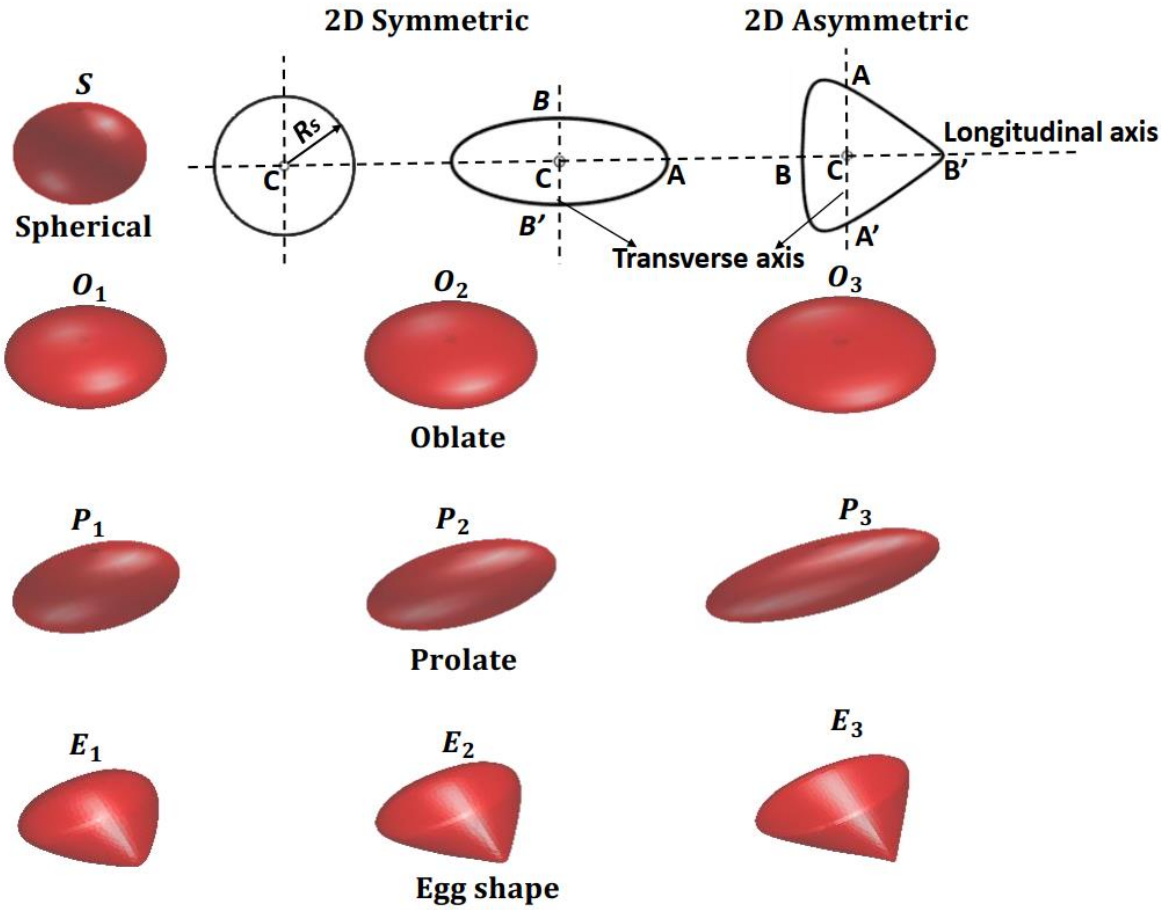

Figure 3.2. Depiction of symmetric and asymmetrical tumor models in 2D and 3D representations

The selected tumors have $5\%, 10\%$, and 20% increase in surface area in comparison to the reference tumor model. Therefore, a total of 10 tumor models (one spherical, three oblate, three prolate, and three asymmetric) are generated for this investigation (see Figure 3.2). The volume, surface area and shape factor for each category of stated shapes, i.e., oblate, prolate, and egg (asymmetric) shape, are enlisted in Table 3.1. It should be noted from the table that

the surface area of each tumor is with respect to the surface area (A_s) of the referenced spherical tumor. The notations 'O,' 'P,' and 'E' in Figure 3.2 represent the oblate, prolate, and egg (asymmetric) shaped tumor models, respectively. The subscripts $1, 2$, and 3 in these notations describe the increase in surface area by $5\%, 10\%$, and 20%, respectively, with respect to the spherical tumor. The symmetric tumor models (oblate and prolate) are generated by changing the major and minor axis of their base ellipse (2D symmetric in Figure 3.2). These axes are correlated with each other in terms of eccentricity(e), which varies from 0 to 1. As the eccentricity increases from zero, the circle changes into an ellipse [95]. The rotation of the ellipse (Figure 3.2) about one of its principal axes generates the prolate and oblate models. The eccentricity is suitably selected to generate tumors having an incremental increase of surface area ($5\%, 10\%, 20\%$) for the fixed volume (mass) of the tumor. Similarly, the asymmetric tumor model (egg-shaped) is generated by the rotation of the 2D oval base profile (represented as 2D asymmetric in Figure 3.2) about its longitudinal axis [96]. Again, three different 2D asymmetric oval profiles are generated by a suitable selection of functions generating the oval. Details of the generation of the asymmetric shape are not given for the sake of brevity and can be referred from [96]. It should be noted from Table 3.1 that with an increment in the surface area of each category of tumor, the shape factor of the tumor also increases. However, the increment of the shape factor for different categories of tumors is different. Furthermore, the maximum value of the shape factor ($\zeta = 3.17$) is for P_3 type tumor, while it is minimum ($\zeta = 1.0$) for the spherical tumor (S). Thus, the maximum diameter (size) range of chosen spherical, prolate, oblate, and egg shape tumor model is $2,\ 2.9 - 4.3,\ 2.4 - 2.8$ and $2.22 - 2.56$ cm, respectively. This tumor diameter range is comparable to pathological data of maximal tumor diameter from MRI scans, which are $2.04,\ 2.65, 2.49,$ and 2.55 cm for spherical, segmental, discoidal, and irregular tumors, respectively [39]. However, the generated extreme case of prolate diameter in the current work is higher than that of the maximum diameter of segmental tumors reported by Byrd et al. [39]; this is because in order to evaluate the effect of surface area in the present study, the tumor surfaces are equally increased in each case.

Table 3.1. Details of volume, surface area, and shape factor of the symmetric and asymmetric tumors.

Parameter	Tumor type									
	Symmetric tumor							Asymmetric tumor		
	Sphere	Oblate			Prolate			Egg-shape		
	S	O_1	O_2	O_3	P_1	P_2	P_3	E_1	E_2	E_3
Volume	V_s									
Surface Area	A_s	$1.05A_s$	$1.1A_s$	$1.2A_s$	$1.05A_s$	$1.1A_s$	$1.2A_s$	$1.05A_s$	$1.1A_s$	$1.2A_s$
ζ	1	1.67	2.03	2.67	1.75	2.22	3.17	1.44	1.7	1.87

Figure 3.3 illustrates the physical tumor model used to simulate MNPH with different tumors (Figure 3.2) considered in this study. In the model, the tumor is centrally located, surrounded by healthy cubical tissue. The size of the cubic physical model (including the tumor as well as the healthy tissue) is four times the size of the spherical tumor. Size of the healthy tissue domain is selected in such a way that its boundaries are not thermally affected due to the thermotherapy.

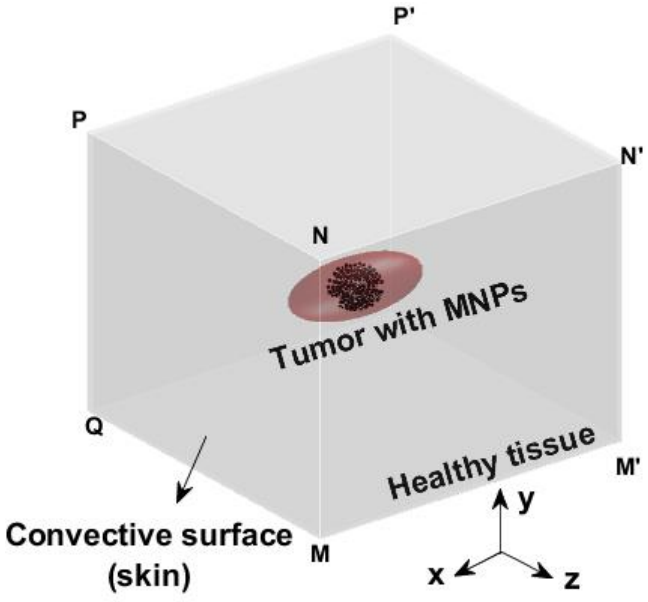

Figure 3.3. The 3D physical model consisting of tumor tisuue with injected MNP, surrounded by a cubic shaped healthy tissue.

3.3 Mathematical model

The Penne's bioheat model (equation 2.1, described in previous "Chapter 2") has been utilized to evaluate the spatial and temporal temperature variations within various tumor shapes, as depicted in Figure 3.2, as well as within the surrounding healthy tissue. To compute Penne's bioheat model for different tumor models, we have employed an in-house algorithm based on the finite volume-immersed boundary (FV-IB) numerical scheme, which we have extensively detailed in Chapter 2. Furthermore, information regarding the external heat source and the distribution of magnetic nanoparticles (MNP) is provided in the subsequent sections.

3.3.1 Heat generation due to MNP in tissues

Various experimental, as well as theoretical studies [25,28], have documented SLP for MNP. In the current study, we have considered the BNF-starch nanoparticles as the MNPH inducers [28]. The SLP of BNF-starch MNP is calculated using a sixth-order polynomial relation reported by Soetaert et al. [54] based on experimental data of Bordelon et al. [28]. In this work, magnetic field strength and frequency are chosen as $20.5\ \mathrm{kAm^{-1}}$and 150 kHz, respectively. The simulated results predict that more than 95% of the referenced spherical tumor is thermally damaged at these magnetic field parameters. It should be noted that for the safe application of MNPH, the product of magnetic field strength and frequency should not be more than $5 \times 10^9\ \mathrm{Am^{-1}s^{-1}}$ [26]. Thus, the selected electromagnetic field parameters for this study are within the safe limit. The value of SLP for selected field strength and frequency is $50.64\ \mathrm{W/(gm\ of\ MNP)}$.

3.3.2 MNP dose and particle distribution in the tumor model

Previous works [9,97] have suggested that the amount of iron above 4 mg per gram of wet liver weight causes hepatotoxicity. Therefore, a total of 16.755 mg of MNP mass, which is equivalent to 3.77 mg per gram of wet liver tumor, is used as the MNP dose in all the tumor phantoms. MNP are injected at the centroid of each tumor model (see Figure 3.3). The Gaussian distribution of MNP in tumor tissues (Figure 3.3), which is a reasonable assumption for MNP distribution in the tissue, is used in this study (details of Gaussian distribution (equation 2.13) is described in "Chapter 2").

The total mass of injected MNP is 16.755 mg. For isotropic Gaussian distribution of MNP in tissue, the standard deviations σ_x, σ_y, and σ_z is chosen as $3\sigma = 5.62$ mm. The selection of this σ-value is based on the *in-vitro* experimentations reported by Salloum et al.

[30] in agarose gel having a concentration of 0.2% with the infusion (injection) rate of $4\ \mu l/min$. Based on the spatial distribution of MNP mass $m(x, y, z)$ and using heating value 50.64 W/ (gm of MNP) , the spatial heat generation (q_{es}) in the tumor models is calculated. The calculated spatial heat generation (q_{es}) is used in PBHT (equation (2.1)).

3.3.3 Thermal dosimetry

The thermal damage in tumor or healthy tissue is estimated based on the parameter Ω as described by equation (2.27). The value of Ω equal to 1 is chosen as the criterion for thermal damage to the tissue and it corresponds to 63% of tissue damage [36]. The revival probability of cells is negligible at this value [76]. Though in literature few limitations of the Arrhenius thermal damage model is also illustrated [99]. However, each mathematical model inherits certain error associated with its assumptions and simplifications. Another thermal dosimetry parameter is the thermal iso-effect dose ($CEM43$) in terms of the cumulative equivalent minutes at $43^{o}C$, which is defined as (equation 3.1),

$$CEM43 = \sum_{n=1}^{N} {R_{CEM}}^{43-T_n} t_n \qquad 3.1$$

where, T_n is the temperature at the n-th time interval (t_n), N is the total time step for which the tissue is exposed to heating during the therapy. The value of R_{CEM} depends upon the reference temperature, $43^{o}C$ [40,100]. The value of $CEM43$ equal to or above 60 minutes is considerd as effective for the thermotherapy and is represented by $(CEM43)_{60}$ [101]. The quantification of thermal dosimetry, i.e., the percentage of tissue volume thermally damaged, is done using parameters C_D and $(CEM43)_{60}$ [40,44] given as (equation 3.2 and 3.3):

$$C_D(\%) = \left(\frac{Tumor\ or\ \ healthy\ tissue\ volume(\Omega \geq 1)}{Tumor\ volume}\right) \times 100 \qquad 3.2$$

$$CEM43_{60}(\%) = \left(\frac{Tumor\ or\ healthy\ tissue\ volume(CEM43 \geq 60)}{Tumor\ volume}\right) \times 100 \qquad 3.3$$

MNPH is considered effective if the values of thermal dosimetry parameters C_D and $(CEM43)_{60}$ exceed 90% of the tumor volume [40,102]. Additionally, thermal damage to the healthy tissue should be minimum and not more than 10% of the equivalent tumor volume [20]. The heterogeneity index (HI), which describes the temperature inhomogeneity [103] in the tumor, is evaluated using the relation $HI = (T_{10} - T_{90})/(T_{90} - T_c)$; where T_{90} and T_{10} are

the maximum temperatures within 90% and 10% of the tumor volume, respectively, and T_c is core body temperature i.e. 37°C.

3.4 Results

The computational results are susceptible to change in grids or mesh used to simulate the physics. Thus, a grid independence test is conducted to make the temperature profile independent of the grid structure. The mesh size ranging from $41 \times 41 \times 41$ to $241 \times 241 \times 241$ are chosen to discretize the physical tumor model (see Figure 3.3). The changes in temperature at specific locations from the centroid of tumors with different grid sizes are measured in the spherical model (as shown in Table 3.2). The relative change in temperature at these locations becomes less than 0.05% when the grid size is increased to $241 \times 241 \times 241$ from $161 \times 161 \times 161$. Thus, all the simulations for MNPH on different tumor models are done with a grid size of $241 \times 241 \times 241$.

Table 3.2. Relative change in temperature with grid sizes

Grid size	L2 norm error (%)
$41 \times 41 \times 41$	-
$81 \times 81 \times 81$	0.786
$161 \times 161 \times 161$	0.1596
$241 \times 241 \times 241$	0.0398

3.4.1 Spatial temperature profile in tumor models

The therapeutic period considered for all the simulations is of 1 hour [102]. The heat source (q_s) from the MNP is switched off after 1 hour and thereafter, tumor model is allowed to cool naturally for 15 more minutes. Application of MNPH induces heat in the tumor model, which leads to a sharp rise in the temperature, especially closer to the MNP injected tissue volume.

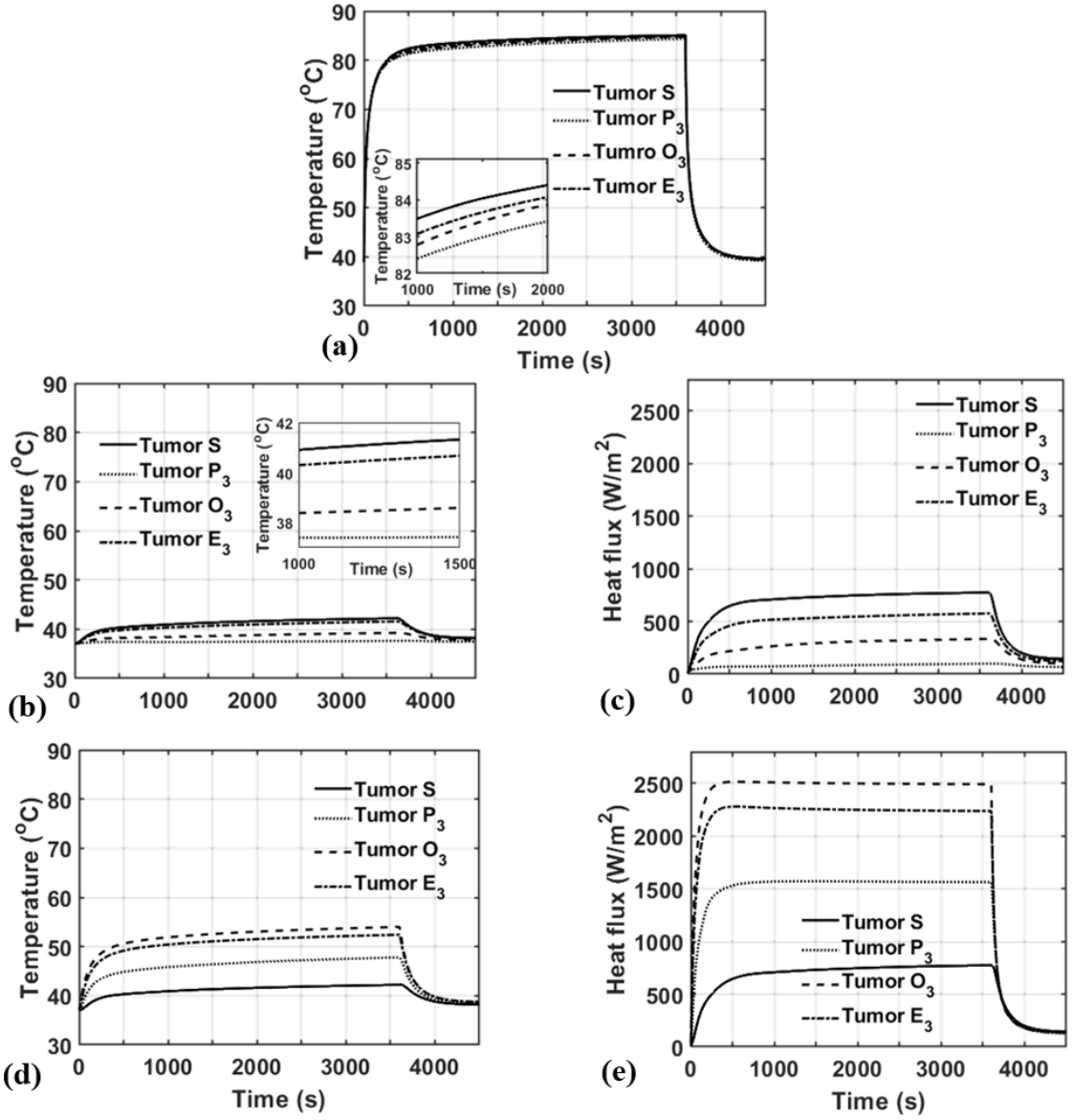

Figure 3.4. Comparison of transient temperature and heat flux profile in tumor shapes S, O_3, P_3 and E_3; **(a)** at the injection site of the tumor; **(b, c)** at tumor –tissue interface point 'A'**; (d, e)** at tumor-tissue interface point 'B'.

Figure 3.4 shows the transient temperature and heat flux plots for three different spatial locations (at the point of injection, at a tumor-tissue interface at point 'A and B along the longitudinal and transverse axis (as shown in Figure 3.2) within the four tumor models (S, O_3, P_3, E_3). It should be noted that maximum temperature is at the point of injection for all tumor models, and the temperature successively reduces with an increase of distance from it. Furthermore, the transient temperature profile in these plots becomes asymptotic nearly after 600 seconds from the beginning of the therapy. When the heat source is turned off after 3600 seconds, the temperature decreases sharply and returns to nearly core body temperature after 4000 seconds. The corresponding plots of heat flux profile at interfacial points 'A' and 'B'

(Figure 3.4c and Figure 3.4e) have similar behaviour as the temperature profile at these points. The point closer to the injection site (like point B of O_3) have higher heat flux as well as temperature in comparison to a faraway point like point A of P_3 . At the interface of spherical tumor, the steady-state heat flux is about $700\ \mathrm{W/m^2}$ and temperature is about $41°\mathrm{C}$. The heat flux rises rapidly as the interface gets closer to the injection point; in the O_3 tumor interface (at point B), the maximal heat flux is approximately $2500\ \mathrm{W/m^2}$ as well as temperature increases to $54°C$. As the tumor border moves away from the injection site, the heat flux decreases, and the minimum heat flux of about $100\ \mathrm{W/m^2}$ is encountered at point A of the P_3 tumor.

The rate of temperature increment is maximum at and around the site of MNP injection. This is due to the presence of a higher MNP concentration at and near the site of injection. However, the concentration of heat generating MNP reduces with distance from the injection site. Thus, the temperature also reduces with distance from the injection site, which is visible in Figure 3.4. The *in-vivo* animal experiment performed Attaluri et al. [19] on implanted prostatic tumors in mice, has also demonstrated that maximum temperature is observed at close to the injection site and temperature successively reduces in a radial direction. The other experiments [9,30] also shown a similar temperature profile during the MNPH application. The steady-state temperature contours in all considered tumor models are shown in Figure 3.5. The presented temperature distribution is along the plane passing through the centroid of tumors and parallel to the plane MNPQ (see Figure 3.3). It should be noted that the nature of the temperature contour is similar in all the tumor shapes (Figure 3.5). This is due to the fact that similar spatial distribution (Gaussian) of MNP which is responsible for heat generation used in all analysed tumor models. The tumor tissue boundary is marked with red color. The variation in tumor shape affects the extent of heat penetration in tumor mass as well as healthy tissue. Maximum temperature (approximately $85°\mathrm{C}$) is reached at the injection site. The temperature asymptotically reduces to the core body temperature of $37°\mathrm{C}$ nearly at a distance of $1.5R_s$ from the site of injection, which is also evident in Figure 3.4(d). However, due to the difference in tumor shapes, the distribution of tumor mass with respect to the isotherm contours changes. Thus, Figure 3.5 qualitatively describes the heat penetration in the tumor as well as the healthy tissue volume in different tumor models.

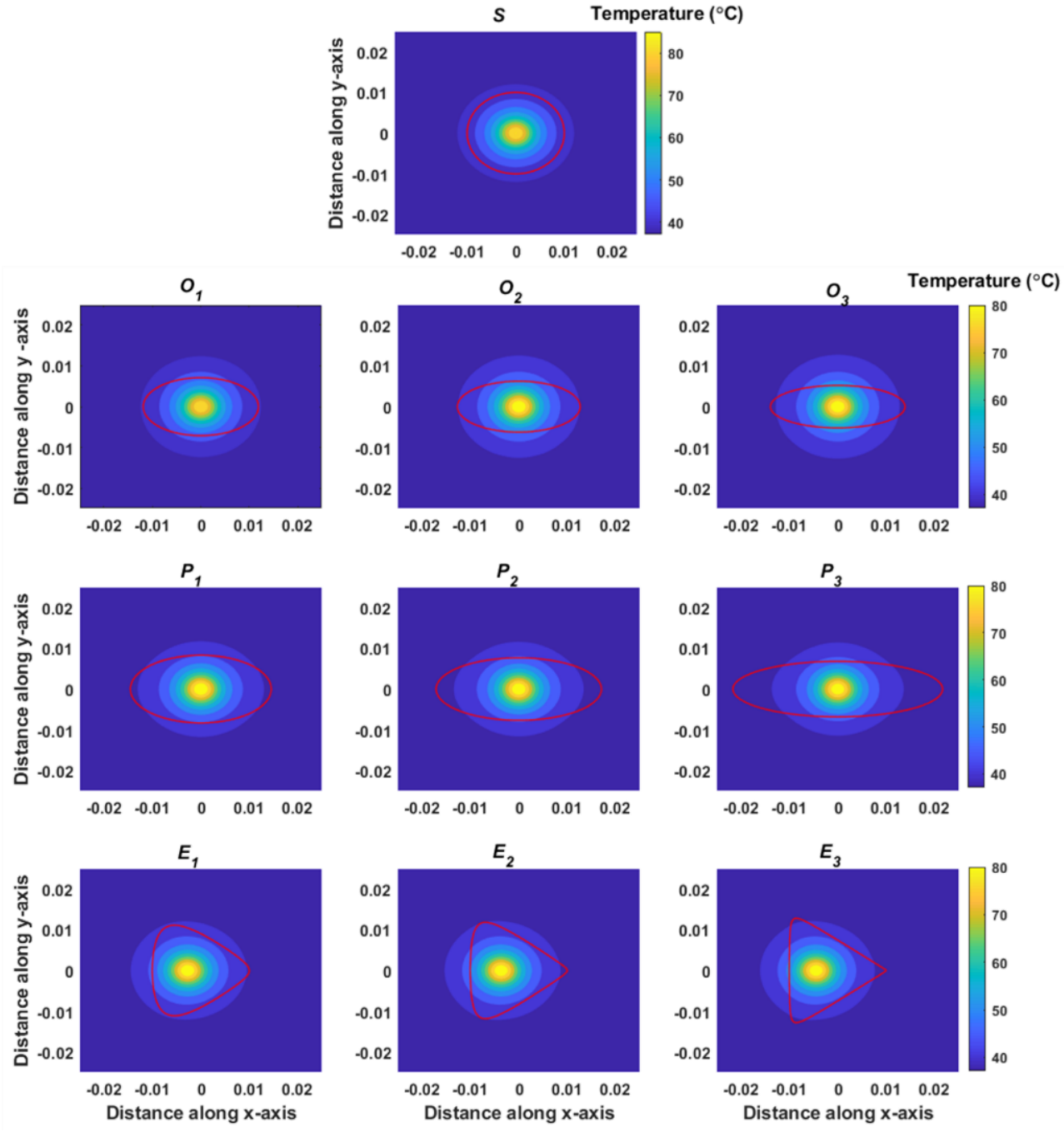

Figure 3.5. Spatial temperature distribution in different tumor models due to MNPH with MNP injection at the centroid of the tumors.

3.4.2 Thermal dosimetry to the tumor as well as healthy tissue

The spatial temperature plots presented in the previous section demonstrate the effect of shape on the heat-affected zone in the tumor as well as healthy tissue during MNPH. However, therapeutic effects in terms of thermal dosimetry need to be quantified due to the rise in temperature during MNPH. The thermal dosimetry of treated tissues is calculated using the

Arrhenius thermal damage parameter (C_D) and $CEM43$ as described before in the subsection Thermal dosimetry. Figure 3.6 describes the extent of thermal damage in terms of C_D for all analyzed tumors again along the plane that passes through the centroid of tumor and parallel to MNPQ (see Figure 3.3).

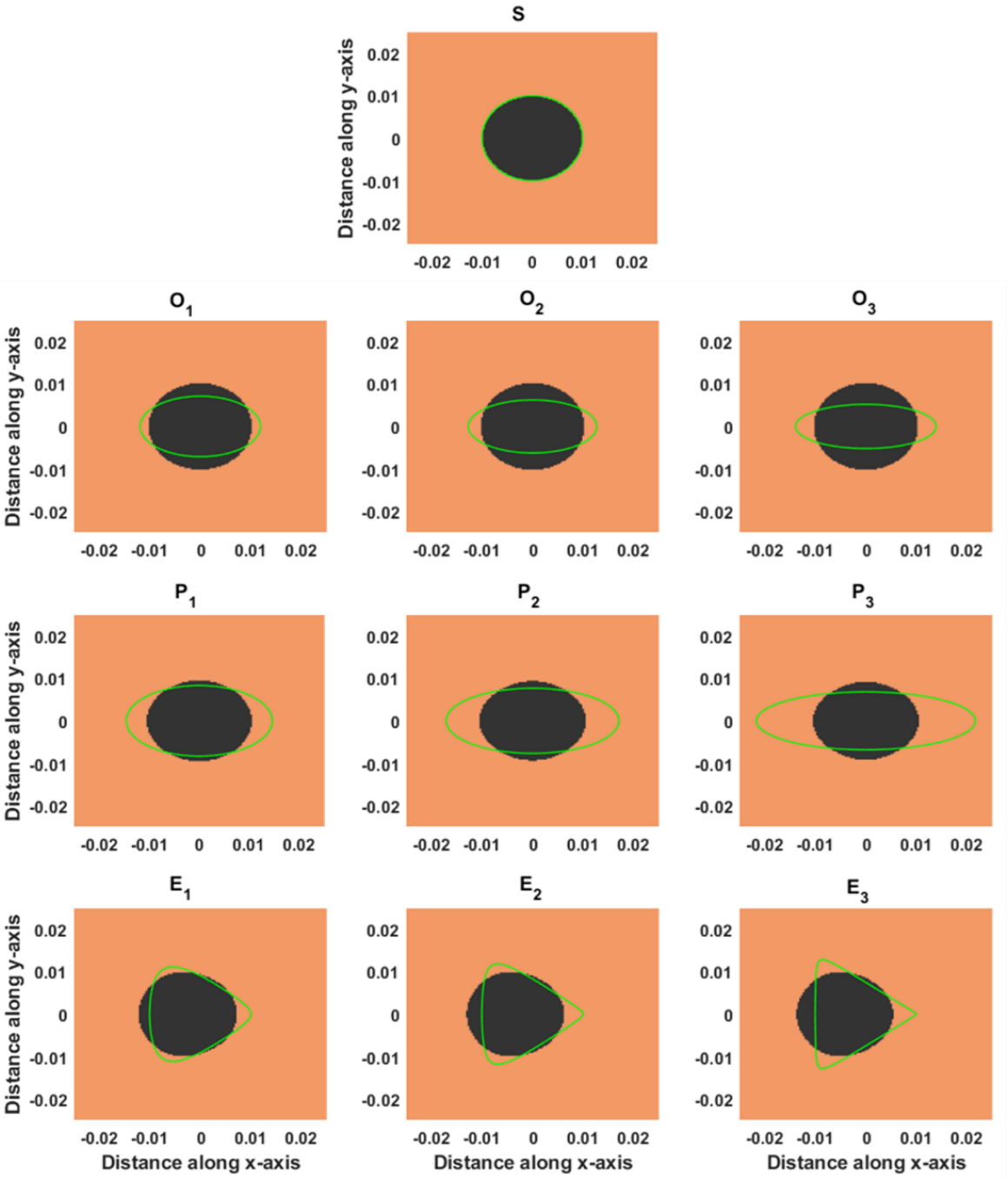

Figure 3.6. Spatial spread of thermal damage in the tissue due to MNPH with MNP injection at the centroid of the tumors.

The black-colored region in all tumor shapes depicted in Figure 3.6 represents the thermally damaged tissues (including tumor and healthy regions). The interface of tumors and healthy tissues are marked with green color in Figure 3.6. It should be noted from this figure that the spherical tumor undergoes maximum thermal damage, while the healthy tissue surrounding it suffers negligible damage. However, as the tumor shape is distorted by increasing the shape factor, thermal damage to the tumor tissue reduces at the cost of an increase in thermal damage to the healthy tissue. Therefore, tumors having the maximum shape factor in each category (oblate, prolate, or egg-shaped) undergo minimum thermal damage, whereas at the same time, the healthy tissue surrounding them suffers maximum thermal damage.

The quantitative details of the therapeutic effects of MNPH in different categories of tumor shapes are enumerated in Table 3.3. This table lists the percentage of tumor and healthy tissue volumes undergoing thermal damage in terms of C_D and $(CEM43)_{60}$ parameters. It also enlists the heterogeneity in the tumor temperature profiles in terms of T_{90}, T_{10}, and HI (heterogeneity index) parameters.

Table 3.3. Heterogeneity, thermal dosimetry parameters attained in the considered shapes of tumors due to MNPH.

		Tumor shapes									
	Parameter	Sphere	Oblate			Prolate			Egg –shape		
		S (1)	O_1 (1.67)	O_2 (2.03)	O_3 (2.67)	P_1 (1.75)	P_2 (2.2)	P_3 (3.17)	E_1 (1.44)	E_2 (1.7)	E_3 (1.87)
Tumor tissue	T_{90}℃	42.77	41.69	41.07	40.26	41.12	40.01	38.75	42.01	41.50	40.76
	T_{10}(℃)	57.57	57.46	57.38	57.25	57.38	57.13	56.76	57.37	57.27	57.20
	HI	2.57	3.36	4.00	5.21	3.95	5.69	10.29	3.07	3.51	4.38
	$\%C_D$	96.96	81.69	74.75	65.37	80.13	71.36	58.94	86.00	81.65	76.06
	$\%(CEM43)_{60}$	71.98	65.90	60.52	52.74	66.83	60.32	50.28	68.36	65.40	61.71
Healthy tissue	T_{max}(℃)	42.30	46.92	49.70	53.51	44.68	45.83	47.73	46.90	49.09	51.04
	C_D(%)	0.00	13.96	19.71	27.43	13.64	18.98	26.73	9.32	12.86	16.50
	$\%(CEM43)_{60}$	0.00	5.02	9.42	15.11	2.59	6.38	12.44	2.40	4.59	7.09

In the context of the thermal dosimetry parameters C_D and $(CEM43)_{60}$, the maximum tumor volume damage is achieved in the referenced spherical tumor model (S), which is nearly 97%. and 72% respectively. As the shape factor for each category of tumor increases, the percentage of tumor tissue volume damage in terms of C_D and $(CEM43)_{60}$ decreases. However, the amount of healthy tissue damage increases with the increase in shape factor of the tumors. It should be noted from Table 3.3 that the percentage of tumor volume damage (58.94% for C_D and 50.28% for $(CEM43)_{60}$) is minimum for P_3 tumor. On the other hand, the percentage of healthy tissue volume damage for P_3 tumor is relatively high (26.73% for C_D and 12.44% for $(CEM43)_{60}$). Similarly, tumors having higher shape factor in other shape categories have similar thermal effects. Furthermore, the egg-shaped tumor E_1 with shape factor (ζ) equal to 1.44, has maximum tumor volume damage, i.e., 86.00% for C_D and 68.36% for $(CEM43)_{60}$, amongst all the three tumor types considered in this study. The shape factor for this tumor is closest to the reference tumor ($\zeta = 1$); thus, the thermal damage induced in E_1-tumor model is also closer to the spherical tumor. This behaviour of lower damage to tumor tissue along higher collateral damage (damage to the surrounding healthy tissue) with the increase in aspect ratio is also demonstrated by Tehrani et al. [99], for microwave ablation.

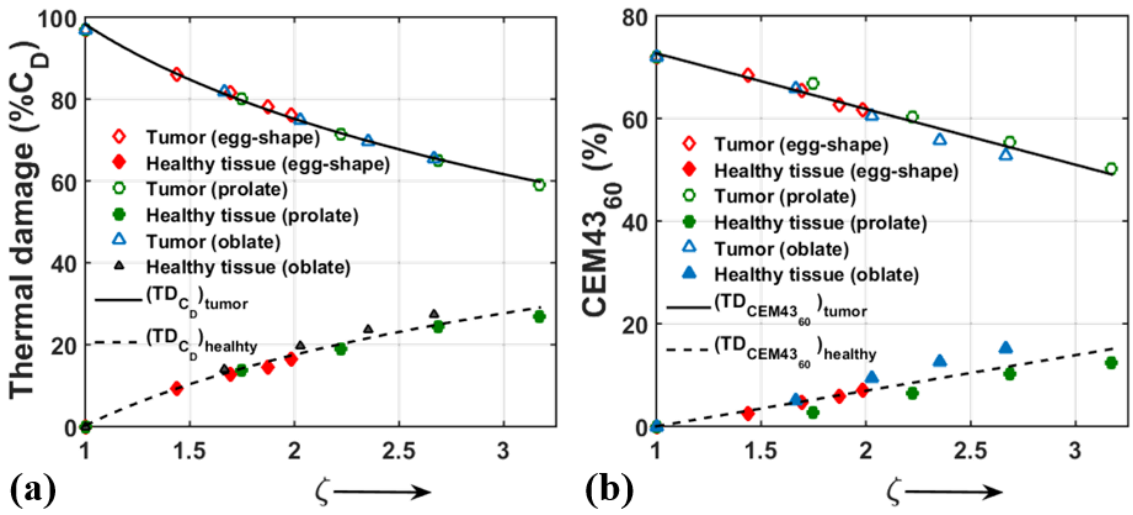

Figure 3.7. Plot between thermal dosimetry (TD) **(a)** in terms of thermal damage $C_D$and shape factor (ζ) **(b)** in terms of thermal dose $(CEM43)_{60}$ and shape factor (ζ), in healthy and tumor tissue due to MNPH.

Concludingly, it can be inferred from this table that tumors having similar volume as well as surface area have thermal damage based on their shape factor. Thus, the shape of a tumor is one of the crucial parameters that affect the therapeutic efficacy of MNPH. Again, the highest heterogeneity HI = 10.29 is observed in P_3 type prolate tumor. However, for the same

tumor surface area as well as tumor volume, the heterogeneity of temperature in O_3 type oblate tumor is approximately half of that of prolate tumor (P_3). Therefore, a detailed computational investigation of MNPH in various tumor shape models gives us an insight into how the shape and direction-specific spread of tumor mass can significantly influence the therapeutic effects of MNPH.

The effects of tumor shape in terms of thermal dosimetry (C_D and $(CEM43)_{60}$) in the tumor, as well as healthy tissue for all the considered tumor models, are summarised in Figure 3.7. Figure 3.7(a) illustrates the plot of the percentage of tissue (tumor and healthy) damage in terms of C_D with respect to the shape factor (ζ). Similarly, Figure 3.7(b) describes the percentage of thermal dose in terms of $(CEM43)_{60}$ with respect to the shape factor (ζ). It is evident from Figure 3.7(a) and Figure 3.7(b) that the thermal dosimetry (C_D and $(CEM43)_{60}$) to the tumor volume decreases, and healthy tissue volume increases, with an increase in the shape factor.

Based on these plots, empirical relations are developed to model thermal damage ($\%C_D$) and thermal dose $(CEM43)_{60}$ for both tumor and healthy tissue as a function of the shape factor (ζ) during MNPH, which is given as (equation 3.4 and 3.5): The value of coefficients of these models (equation 3.4 and 3.5) are given in Table 3.4.

$$\%TD_{C_D}(\zeta) = \alpha.\ln(\zeta) + \beta \quad 3.4$$

$$\%TD_{(CEM43)_{60}} = \alpha\zeta + \beta \quad 3.5$$

Table 3.4. Value of curve fitting coefficients based on equation 3.4 and 3.5.

Parameters	Tissue	α	β	Coefficients of determination
TD_{C_D}	Tumor	-33.36	98.38	99.6%
	Healthy	-25	0.2048	96.16%
$TD_{(CEM43)_{60}}$	Tumor	-10.86	83.54	96.18%
	Healthy	6.94	-6.94	80%

These thermal dosimetry models (TD_{C_D} and $TD_{CEM43_{60}}$) inherit the useful information for the therapeutic effects of MNPH thermotherapy for a wide range of tumor shapes and can be used to predict the therapeutic effect due to MNPH for irregularly shaped tumors based on its shape factor.

3.5 Discussion

Magnetic hyperthermia is one of the promising hyperthermia applicators that reach clinical trials [35]. Many experimental and computational studies addressing wide aspects of this therapy have been published [9,19,20,30,40,44,54,55,104,105]. Despite this, limited studies have been done on the effects of tumor shape on the treatment [20,44,54,55]. Thus, attempts have been made in this study to quantify the relation between therapeutic effects and tumor morphologies. The selected shapes (spherical, ellipsoidal, and egg shape) are within the broad category of tumor shapes as classified in literature [39]. The effect of above mentioned shape are also investigated for drug delivery and microwave thermotherapy [95,99,106]. The previous works by Sefidgar et al [106] shows that for systematic administration, spheroid shape (prolate and oblate), the drug delivery is higher than the spherical shapes [93,95,99]. The thermotherapy with microwave ablation shows that the tumor shapes significantly affects the treatment [99]. Therefore, in the present work, the therapeutic effects induced due to a single MNP injection on the tumors with varying morphologies and surface areas having constant tumor volume are investigated. Tumor shape/morphology is altered by changing the governing parameters associated with the geometry of the tumor. For simplicity, both tumor and healthy tissues are considered homogeneous, isotropic, and not close to any major blood vessel. The properties of the liver tissues (tumor & healthy) are used in the tumor model. In all tumor models, an MNP dose of 3.77 mg per gram of wet liver tumor tissue is injected. Post injection, the distribution of MNP in the tissue is considered as Gaussian and remains invariant to the shape of the tumor. Though the distribution of MNP is hypothetical in nature, however, few experiments have supported the claim that in soft tissues like the liver with a lower injection rate, a nearly uniform 3D Gaussian distribution of MNP can be achieved [9,20,30]. In general, the tissues are heterogeneous in nature and MNP distribution post-injection depends upon tumor physiology and injection rate [9,40]. However, simplifications considered in the tumor model make it more tractable and computationally less expensive. With this framework, the temperature profile and therapeutic effects of MNPH (with a therapeutic time of 1 hour) are computed for considered tumor models in terms of parameters C_D and $CEM43$. Computational results show that temperature in the tissue is maximum at the point of injection, and it reduces in a radial outward direction. Similar temperature profiles are also observed in the previously reported computational works on MNPH with Gaussian MNP distributions [20,40,44,54,55]. Even, the bell-shaped temperature profile, where the temperature reduces radially from the

point of injection is also reported in the *in-vivo* on mice by Attaluri et al [19]. Though, the shape of the bell depends upon the ferrofluid infusion rate in the tissue [19].

Therapeutic effects primarily depend on the elevation of temperature above the therapeutic temperature $(43℃)$ inside the tumor tissue. However, the heated tissue volume depends on the MNP distribution and the AMF parameters. Furthermore, depending upon the tumor size, shape, and MNP injection site, the extent of heat penetration within the tumor and its surrounding healthy tissue is quite unpredictable. As can be seen from the results, tumors having a high degree of geometrical distortion (high shape factor) like P_3 and O_3 tumors have very less thermal damage inflicted on their volume. The high value of heterogeneity of temperature in these P_3 and O_3 tumor models (reflected in the *HI* parameter) is the cause of inadequate thermal damage to the tumor volume. For a tumor volume having greater asymmetry in terms of the spread of tumor in different directions, a higher amount of heat penetrates the healthier tissue from the location where the tumor periphery is closer to the MNP injection site. Such heat penetration into the healthy tissue causes substantial thermal damage to healthy tissue, which is observed for extreme cases of tumor models P_3, O_3 and E_3. The results of thermal dosimetry reflect that the maximum tumor volume that is thermally damaged is the referenced spherical tumor because of its dimensional symmetricity. The obtained results also show that an equivalent increment of surface area in the different tumor shapes (prolates, oblates, and egg-shaped type tumors) will not result in similar thermal dosage or damage to the tumor tissue. This is primarily due to the difference in the extent of heat penetration in the tumors with different shape factors. Therefore, the spatial tumor tissue distribution is one of the critical parameters of MNPH. As real tumors can have any geometrical shape, thus it can be quantified in terms of the shape factor (ζ). The shape factor provides a simple and effective way to describe the spatial spread of a tumor. The concluding results, as presented in Figure 3.7, indicate that as the shape factor of the tumor increases, the efficacy of MNPH decreases. The generic correlations developed between the thermal dosimetry to the tumor and shape factor can be used as a tool to estimate the therapeutic effects based on the geometrical features of the tumor with respect to an ideal spherical tumor mass. Even though, these correlations inherit the inaccuracies associated with the simplifications and assumptions used in the computational models. However, future studies can consider more realistic parameters based on the tumor physiology, MNP distributions, and shape to generate correction factors for these correlations.

3.6 Closing Remarks

Due to the geometrical complexity associated with real tumors, the effectiveness of MNPH is relatively difficult to assess. The effectiveness of MNPH treatment using intratumoral MNP injections is numerically investigated in this work for different tumor shapes (spherical, oblate, prolate, and egg-shaped). The simulated results show that the shape of the tumor has a significant effect on the efficacy of MNPH. Correlations developed in this work will aid to assess the therapeutic effects of MNPH on real complex-shaped tumors.

Chapter 4

Estimation of the injection criteria for optimizing the magnetic hyperthermia therapy based on tumor morphology

4.1 Introduction

In the previous chapter, we have examined the tumor morphological effects on the efficacy of MNPH therapy. The results predict that increasing the aspect ratio of tumor shape, reduces the therapeutic effects of MNPH therapy during a single MNP injection. However, a single injection leads to uneven thermal damage inflicted on the tumor volume, especially at the portions where dissemination of heat-generating MNP is less [30]. Thus, the spread of heat generating MNP in the tumor tissue plays an important role besides other factors like tumor physiology and magnetic field parameters. Experimental studies (clinical and animal experiments) have shown that the dispersion patterns of MNP in the tissue after their injection are non-uniform [9,19,34]. As tumors can have any irregular shape, tumor morphology proliferates irregularly and migrates with persistent protrusion [107,108]. Thus, the distribution of MNP by single intra-tumoral injection may not be good enough to produce an optimum therapeutic effect throughout the complex-shaped tumor volume [9,35,109]. The chances of inadvertently heating surrounding healthy tissue are high for tumours with a high aspect ratio (as seen in Chapter 3). Also, the geometrical irregularities associated with the tumor, increase the complexity of devising a suitable intratumoral injection protocol for MNPH. To enhance the MNP distribution throughout the tumor volume many multi-site injection strategies have been proposed [20,44–46,49]. Intratumoral multi-injection strategy enhances the efficacy of magnetic nanoparticle hyperthermia therapy (MNPH) [20,44,46,110]. In this study, criteria for the selection of injections and their location depending on the tumor shape/geometry are developed. Developed strategy is based on the thermal dosimetry results obtained on different invasive 3D tumor models during MNPH simulation. MNPH simulations are conducted on physical models of tumor tissue encased within the healthy tissue. Primary & secondary injections are used to inject MNP fluid based on the invasiveness of the tumor. Optimizing strategy is devised based on the zone of influence of primary & secondary injection. The algorithm for this strategy is based on the numerical experiments simulating MNPH, conducted on the tumor models with varying aspect ratios and protrusion in a specific direction. In the tumor models, MNPH is computed using Pennes' bioheat model with temperature-dependent perfusion rate (as discuss in the previous chapter) to determine temperature distribution for

single and multi-injection strategies. Finite volume- immersed boundary (FV-IB) numerical methodology [111] is used to solve the governing mathematical model of MNPH.

4.2 Methodology

4.2.1 Injection strategy

Tumor morphology depends on the spatial growth of malignant cells. Most of the tumor morphology is irregular and migrates with continuous protrusions [107]. Tumors are broadly categorized into spherical, oblate, prolate, ellipsoidal, and irregular [39] in shape. Mostly spheroid tumors develop thin branches of invasive cells that protrude from the main tumor mass. To quantify the protrusion, Hou et al. [107] have defined a "core radius" that encloses the main tumor mass, and an "invasive radius" that encases the extent of a protrusion (as shown in Figure 4.1(a)). Figure 4.1(a) represents the morphological properties of spheroid tumors [107] (Figure reproduced under a Creative Commons Attribution 4.0 International License). We have used similar terminology and concepts in the present work to develop the multi-injection strategy, as illustrated in Figure 4.1(b-c). Figure 4.1(b) represents a star-shaped tumor that protruded in three directions. The core radius, a circle having a maximum size (green dashed curve), is inscribed within the tumor model. The portion of the tumor enclosed by the core radius 'r_o' (center O), is the tumor core. The protruding branches are estimated by the distance between tumor core center (O) and extreme point on the protruded surfaces. Like the distance r_1 (between branch point 'c_1' and $'O'$) quantifies the extent of tumor protrusion in specific direction. Considering branch point 'c_1' as center, an arc is drawn that intersects tumor boundaries at a_1b_1. The region covered by this arc with branch point 'c_1'is the zone of protruding branch. Similarly, from other branch points c_2, and c_3 zone of influence of other protruding branches is quantified with radius , r_2, and r_3, respectively. In this example only three protruding branches are considered, however, an arbitrary shaped tumor can have more protruding branches.

As discussed in the introduction, multi-injection induces a more uniform temperature profile. Thus, in addition to having an injection in the core tumor, additional MNP injection to each protruding branch may induce higher therapeutic effects. In this manuscript, injections injected into the protruding branches are named secondary injections, and injection to the tumour's core is called primary injection. However, the position of the secondary injection point needs to be located to induce higher therapeutic effects. This location of the secondary

injection is considered within a distance kr_i from the branch point along the tumor center. Where r_i, is the radial distance for i^{th} protruding mass and k is a factor that ranges from 0 to 1. If k is 0, the protruding volume merges with the main tumor, and the k equal to 1 represents the total protruding tissue volume under secondary injection. The region inscribed by kr_i as shown in Figure 4.1(c), represent the zone of influence by secondary injections. The suitable selection of the factor $'k'$ is key to positioning the location of secondary injection in each protruding branch.

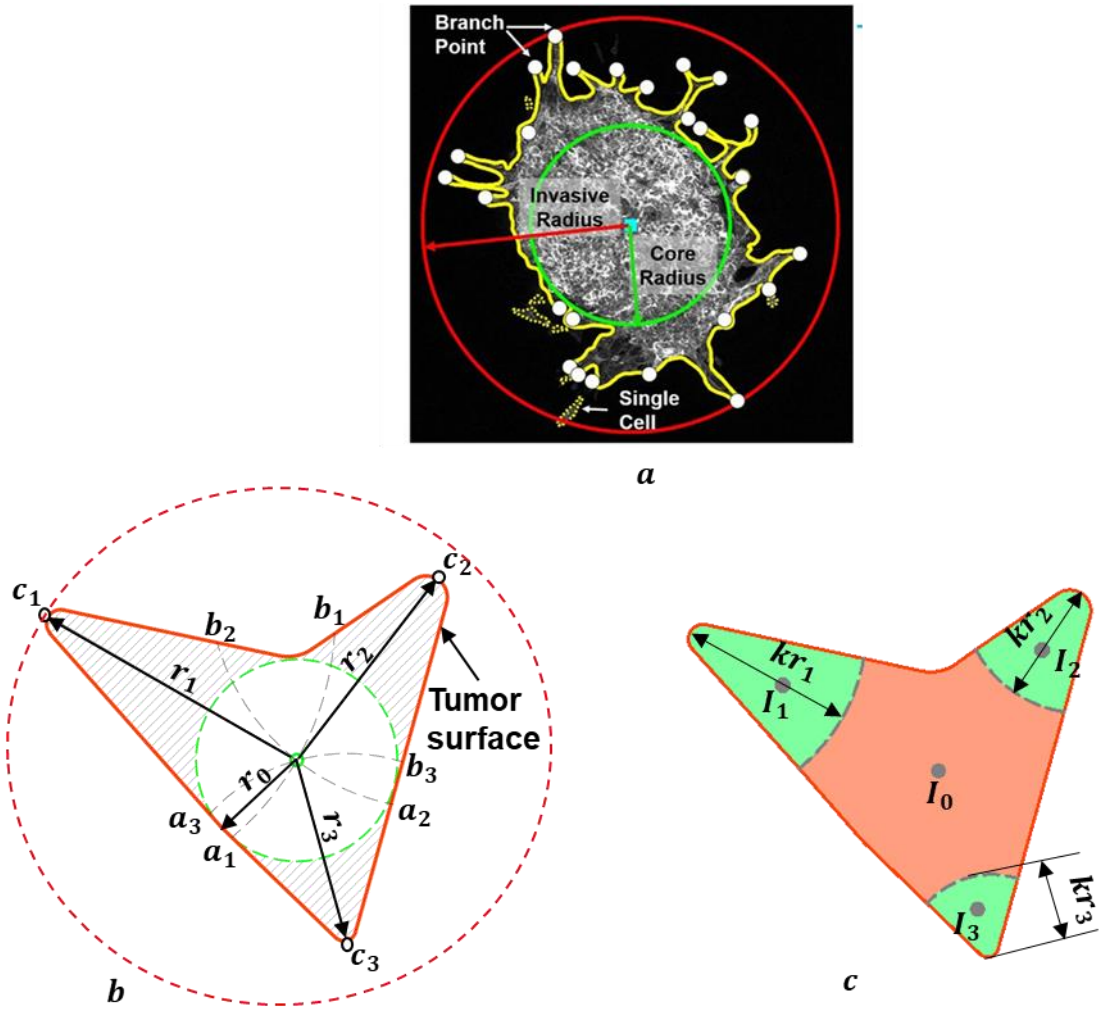

Figure 4.1. (a) Shows the morphology features, invasive and core radius of spheroid tumor [107]; **(b)** Depicts the multi-injection strategy in 2D star-shaped tumor model; **(c)** illustrates the injection locations and zones of influence of secondary injection.

Figure 4.1(c) also depicts the secondary injection locations I_1, I_2 and I_3, which is the centroid of the zone of influence (within the distance kr_1, kr_2 and kr_3 , respectively). The primary injection $'I_o'$ is applied at the centroid of the remaining tumor (total tumor volume minus the volume under kr_1, kr_2 and kr_3). However, the distance factor 'k' is still unknown.

Computational experiments are conducted on tumors with varying degrees of invasion or protrusion size to evaluate the optimized distance factor '*k*'.

4.2.2 Tumor models

The aim of optimizing the multi-injection MNPH treatment is to increase the therapeutic effect in the tumor volume while causing minimal or negligible damage to healthy tissue. The location of primary and secondary injections in the tumor, as well as its dependency on factor 'k', is discussed in the previous section. In order to evaluate the optimum value of k, the computational experiments are conducted on the 3D tumor model, as shown in Figure 4.2. These tumor models are created by superimpositions of spherical and ellipsoidal volumes. The categorization of tumors based on their geometrical properties is described in detail by Byrd et.al.[39]. The classifications depend on the maximum and minimum tumor extent from the center point of tumor, which is r, and r_0 respectively as depicted in Figure 4.2(a). The selected tumors fall under the category of spherical (M1, M2, and M3) and segmental i.e., rod like (M4, M5, and M6) tumors. Three-dimensional view of these tumors are shown in Figure 4.2. The tumor volume of all the tumor models is same, and it is equal to the volume of spherical shape tumor having a radius 1 cm. This spherical tumor size is with reference to first stage liver cancerous tissue size [90]. However, the maximum size of the selected tumor models ranges from nearly 2.5 to 3 cm. This range of liver tumor models has been considered in the second-stage tumor category [90].

In the considered tumor models (M1 to M6), the base tumor (core) is spherical, and its surface protrudes in one direction. It should be noted that the degree of protrusion, as well as aspect ratio (defined as the ratio of maximum to the minimum spread of tumor tissue), are different for the selected tumor shapes. For the multi-injection strategy, two injections are chosen: primary injection ('I_p') for the main tumor and another secondary injection ('I_s'') for the protruded portion. The locations of both injections vary with change in the value of 'k'. It is illustrated in Figure 4.2(b), the two arcs $A1$ and $A2$ are drawn with two different values of 'k'. The primary and secondary injection location change from I_{p1} to I_{p2} and I_{s1} to I_{s2}, respectively as a zone of influence of secondary injection changes from $A1$ to $A2$ (as shown in Figure 4.2(b)). The MNP dose administered at the secondary and primary injections site is in proportion to the zone of influence of secondary injection and the remaining tumor volume, respectively.

Table 4.1. Geometric properties of tumor models

Tumor model	M1	M2	M3	M4	M5	M6
Aspect ratio	1.5	1.5	1.5	2	2	2
Total volume	V					
	3.34	4.94	6.21	8.54	13.13	16.45

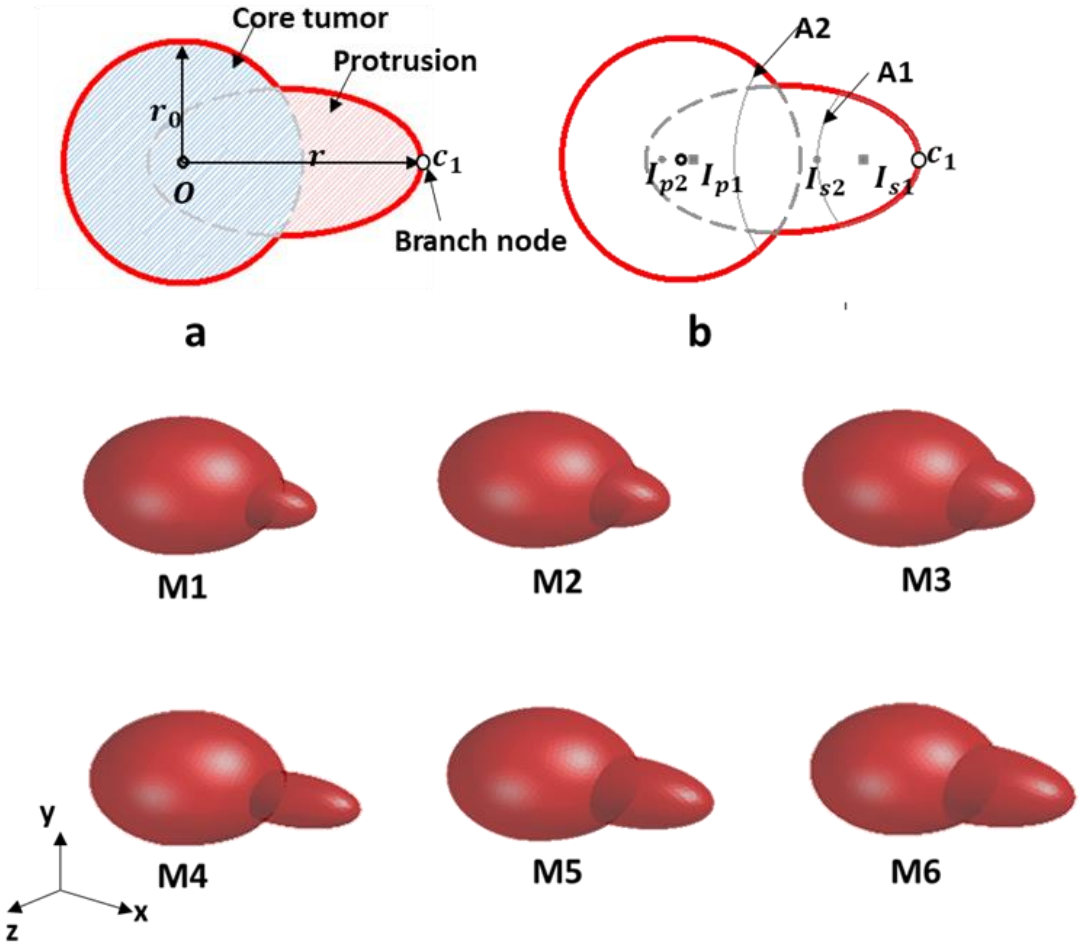

Figure 4.2. Depiction of tumor models having different degree of unidirectional protrusion in 2D and 3D representations.

The invasiveness of the tumor is calculated by the aspect ratio. The aspect ratio of the tumor is the ratio of the distance of branch node (point) from the tumor core center i.e., $'r'$ to the main/core tumor radius (r_0) as depicted in Figure 4.2(a). The two groups of tumors having an aspect ratio of 1.5 and 2 are considered to generate tumor shapes with different morphology. Tumors having an aspect ratio greater than 2 will generate highly invasive thin tumor, in which clinical restriction may arise for intratumoral MNP injection. The percentage volume of protruding mass to the total volume V_p/V is varied approximately from 3.34 to 6.2%

and 8.5 to 16.4% for the protruding tumors having aspect ratios 1.5 and 2, respectively, as depicted in Table 4.1. Each tumor model is enclosed within the healthy cubic tissue (as shown in Figure 4.3). The length of healthy cubic tissue is four times the equivalent spherical radius of a tumor. A similar type of tumor model, containing tumor mass surrounded by the healthy tissue, is also utilized in work reported by Singh et al. [44] as well as other researchers [40,54] working on MNPH. It should be noted that, in a realistic scenario, there may be multiple protrusions as discussed in Figure 4.1. However, results obtained using a single protrusion can be applied to complex tumor morphology having many branches.

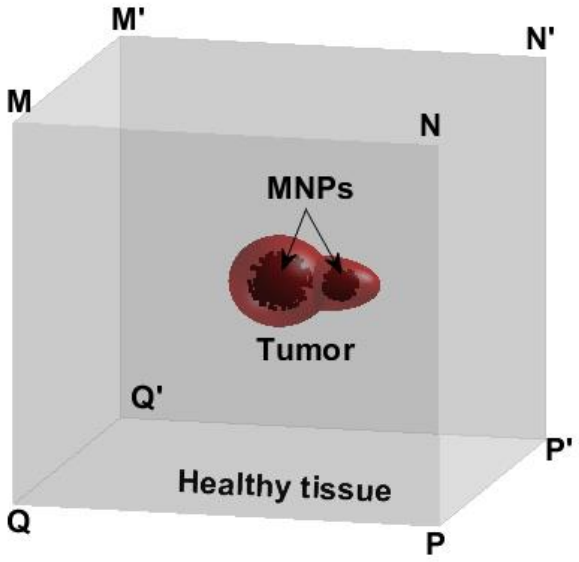

Figure 4.3. The 3D physical tumor model with MNP injection and surrounded by healthy tissue.

4.2.3 Mathematical model

FV-IBM based in house solver of Penne's bioheat model as illustrated in the previous "Chapter 2" has been utilized to simulate the multi-injection MNPH therapy. The simulation of MNPH therapy provides the spatial and temporal temperature profile within the different protruding tumors. Again, the temperature profile depends on the amount of MNP and its distribution in both the single and multi-injection strategies. In the following section, the injection amount and its distribution by the primary and secondary injections sites are described.

4.2.4 MNP dose and particle distribution in the tumor model

The total MNP dose 16.775 mg mass of BNF, having a $15 - 20$ nm particle size, is injected into each tumor model, which is equal to 3.77 mg per gram of wet liver tumor. This total mass

of MNP is injected into the tumor with single or multiple (primary and secondary) injections. The representative distribution of MNP by the two injections in the tumor volume is depicted in Figure 4.3. The location of the primary injection (I_p) is at the centroid of tumor tissue volume obtained by deducting the zone of influence of secondary injection from total tumor volume i.e., area left of $A1$ or $A2$ curve in Figure 4.2(b). The secondary injection point (I_s) is the centroid of zone of influence of secondary injection, along the OC_1 line. The amount of MNP dose in primary and secondary injections depends on the factor 'k'.

The Gaussian distribution is assumed to be isotropic in all directions, thus the standard deviations σ_x, σ_y, and σ_z are equal. However, the values of standard deviation are considered based on the quantity of the injected MNP at primary and secondary injection. For the total MNP dose, the 3σ is considered as 5.62 mm and it is assumed linearly decreasing as the MNP dose reduces. This σ-value has been chosen based in line with the in-vitro experimentations reported by Salloum et al. [30] in agarose gel with a concentration of 0.2% and infusion rate of 4 $\mu l/min$. The spatial heat generation (q_s) in the tumour models has been calculated based on the spatial distribution of MNP mass $m(x, y, z)$ and using heating value $50.64\ \mathrm{W/(g\ of\ MNP)}$. The calculated spatial heat generation (q_{es}) has been used in PBHE (equation (2.1)).

4.2.5 Heat generation due to MNP in tissues

In the current study, the BNF-starch nanoparticle is considered as the MNPH inducer. The SLP of BNF-starch MNP is calculated with a sixth-order polynomial relation proposed by Soetaert et al. [54], which is based on the experimental data of Bordelon et al. [28]. Magnetic field parameters, i.e., frequency and field strength of 150 kHz and $20.5\ \mathrm{kAm^{-1}}$ respectively are used for the simulation of MNPH in the considered tumor models. The value of SLP for selected field strength and frequency is $50.64\ \mathrm{W/(g\ of\ MNP)}$.

4.3 Results

4.3.1 Spatial temperature profile in tumor models

The therapeutic period is chosen as 1 hr [102] for all the tumor models used in this study to simulate MNPH. Due to the application of MNPH, the temperature rises in the tumor tissue. The temperature distribution on one of the tumor models (M6) using single and multi-injection is shown in Figure 4.4. The isotherms line in Figure 4.4 is illustrated on the plane parallel to MNPQ (as shown in Figure 4.3) and intersects the centroid of tumor. It should be noted from

this figure that the temperature profile is more uniform with two injections (Figure 4.4(b) in comparison to a single injection (Figure 4.4(a)) applied during MNPH). The temperature profile is in line with the nature of the expected temperature profile using single and multi-injection strategies [20,44–46,49]. The temperature increment and spread in the tumor tissue rely on the MNP dose and distribution. The temperature is higher near the injection location and lowers as one approaches the tumor boundary [19,30,40,44].. This is because of the high concentration of MNP surrounding the injection site. Thus, multi-injection strategy is found to be more effective to produce higher therapeutic effects during MNPH. However, further investigation is needed to optimize the location of secondary injection with respect to primary injection. This is done by the variation of k and evaluating its effects on the temperature profile induced due to MNPH in all the tumor models in terms of heterogeneity Index (HI). Figure 4.5 demonstrates the variation of HI with factor k for two tumor groups having aspect ratio ($r/r0$) i.e., 1.5 and 2. It should be noted from this figure, the maximum heterogeneity in temperature is induced for single injection ($k = 0$) in all tumor models, during magnetic hyperthermia therapy. Furthermore, *HI* also increases with the increasing the protrusion volume with respect to total tumor volume i.e. (V_p/V) for both aspect ratios. For all the tumors as the secondary injection is induced i.e., $k > 0$, the *HI* in the tumor starts reducing. The minimum value in heterogeneity achieved between 'k' 0.7 and 0.8 for all the considered tumor in this study. Thus, the results say that if the zone of infuance of secondary injection is in between $0.7r_i$ to $0.8r_i$, higher theraupetic effects will be produced due to MNPH. Therefore, the factor (*k*) associated with the zone of secondary injection is chosen as 0.75 to have higher thermal effects during MNPH.

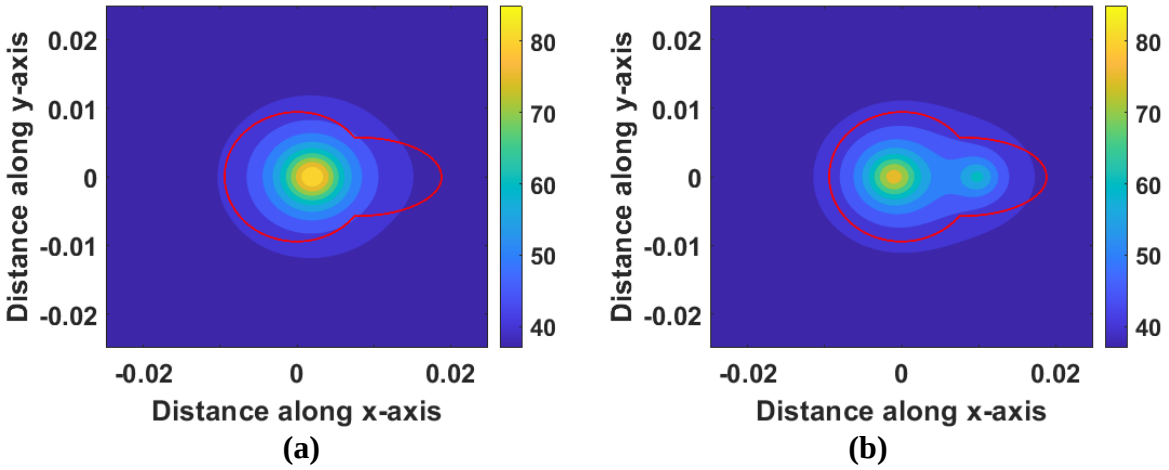

Figure 4.4. Isotherms produced due to **(a)** single and **(b)** multi injection strategy during MNPH.

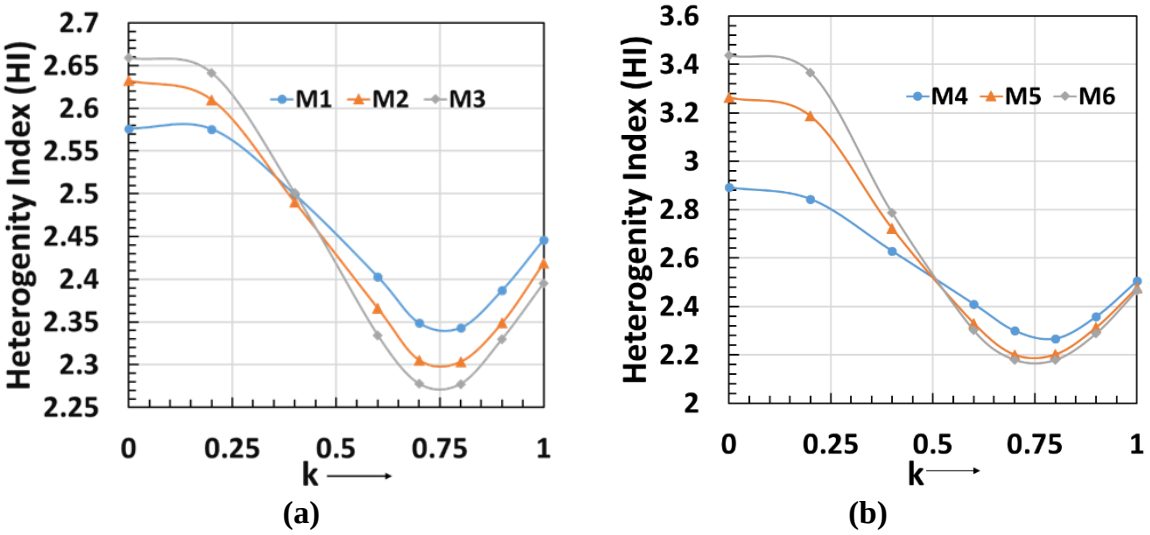

Figure 4.5. Plot between the factor '*k*' and heterogeneity index (*HI*) **(a)** at aspect ratio 1.5 **(b)** at aspect ratio 2.

Further numerical experiments are performed to establish criteria for the selection of a multi-injection strategy over a single injection. Figure 4.6 illustrates the temperature profile produced by single and two-injection approaches in the tumor models (M4 and M4) during MNPH. Temperature is plotted along the line that passes through the centroid and x-axis in the tumor model. The distance along the x-axis in Figure 4.6 is represented as R^*, which is normalized by the spherical tumor radius. As discussed above, to have higher therapeutic effects, the value of k is chosen as 0.75 to get the location of the secondary injection with respect to the primary injection for the multi-injection strategy. The tumor boundaries in the x-direction are represented by TB-min and TB-max in these plots along the x-axis.

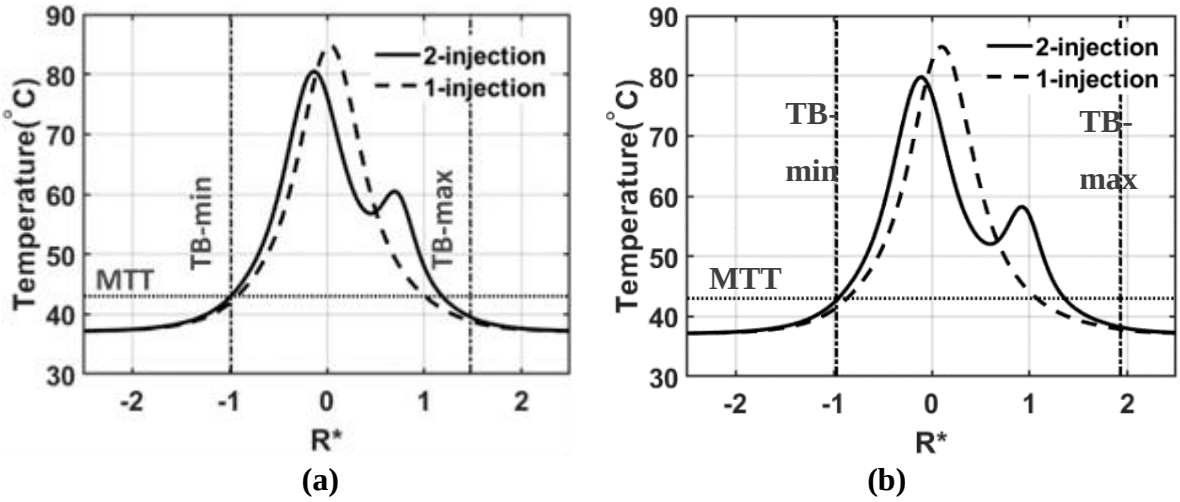

Figure 4.6. Comparison of single and multi-injection strategies in tumor models $(\boldsymbol{a})\ M1\ (\boldsymbol{b})\ M4$

The MTT line represents the minimum therapeutic temperature which is 43℃. It is visible in Figure 4.6, two injections produce two distinct bell-shaped temperature curves, whereas a single injection produces only one temperature hump in the tumor during MNPH. Again, the maximum temperature for these humps is at the injection sites. This is owing to the presence of a higher amount of MNP concentration at and near the injection sites. Furthermore, the width of the bell-shaped temperature profile is bigger in the case of multi-injection for both tumor models. Because the spread of MNP in tumors tissue is higher with two injections in comparison to a single injection. Thus, more tumor volume is above the MTT line, in multi-injection cases, compared to single injection.

Figure 4.7 shows the steady-state temperature contours induced during MNPH in three tumor models ($M1$, $M4$, and $M6$) with single and multi (two) injections. The presented isotherms are along the plane that passes through the centroid and parallel to MNPQ (in Figure 4.3). The tumor-healthy tissue interface is marked with a red line. Results show that the multi-injection temperature profile is more uniform than the single injection in all tumor models. The variation of tumor shape in terms of (r/r_0) and (V_p/V), affects the extent of heat penetration in the tumor as well as healthy tissue.

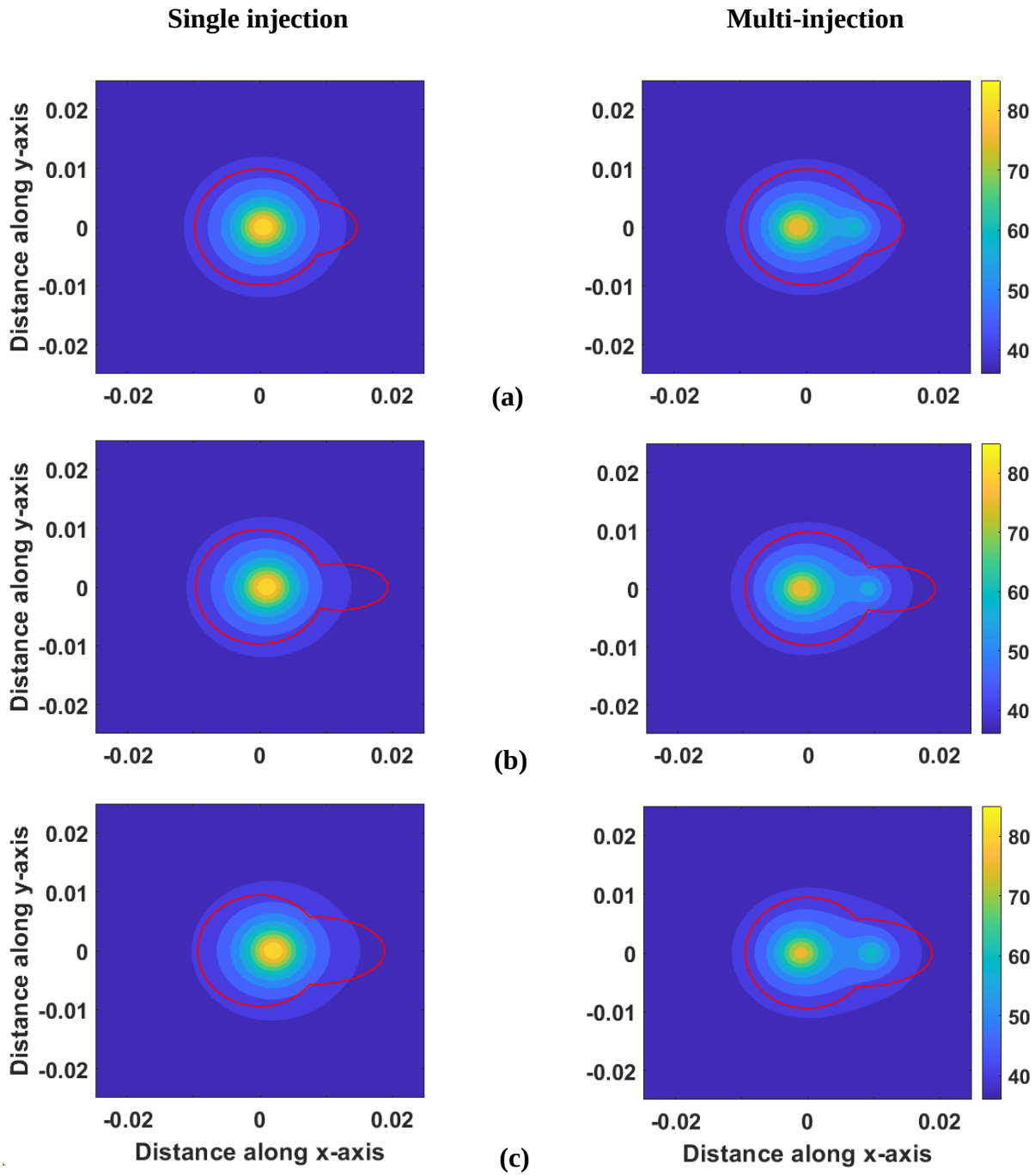

Figure 4.7. Comparison of spatial temperature in single and multi-injection approach in tumor model **(a)** $M1$ **(b)** $M4$ and **(c)** $M6$

4.3.2 Thermal dosimetry to the tumor as well as healthy tissue

The spatial temperature plots presented in the previous section demonstrate the comparison of two injection approaches on the tumour's heat-affected zone and healthy tissue during MNPH. However, therapeutic effects during MNPH, in terms of thermal dosimetry, is calculated using the Arrhenius thermal damage parameter (C_D) and $CEM43$ as described in **Chapter 3**. Figure 4.8 describes the extent of thermal damage in terms of C_D for three tumor models having

secondary tumor volume varies from 3.34% to 16.54%. Again, the thermal damage is shown along the plane that passes through the centroid of the tumor and parallel to MNPQ (see Figure 4.2). The black-colored region in all tumor shapes in Figure 4.8 represents the thermally damaged tissues (including tumor and healthy regions). Similar to Figure 4.7, the interface of tumors and healthy tissues is marked with red in Figure 4.8. It should be noted that from this figure for the tumors having smaller secondary tumor volume (V_p/V) like '$M1$' the tumor damage is comparably similar in single and multi-injection approaches. The thermal damage caused by single injection decreases as the secondary tumor size increases, whereas the damage caused by the multi-injection approach remains more or less constant. Additionally, when the protrusion volume ratio increases, the thermal damage to the surrounding healthy tissue also increases with a single injection. However, in the multi-injection approach, damage to the healthy tissue is not severe compared to a single injection, even for the tumors having a higher protruding volume ratio i.e., M4 and M6. Thus, multi injection strategy is more effective for arbitrarily shaped tumors having high protrusion volume.

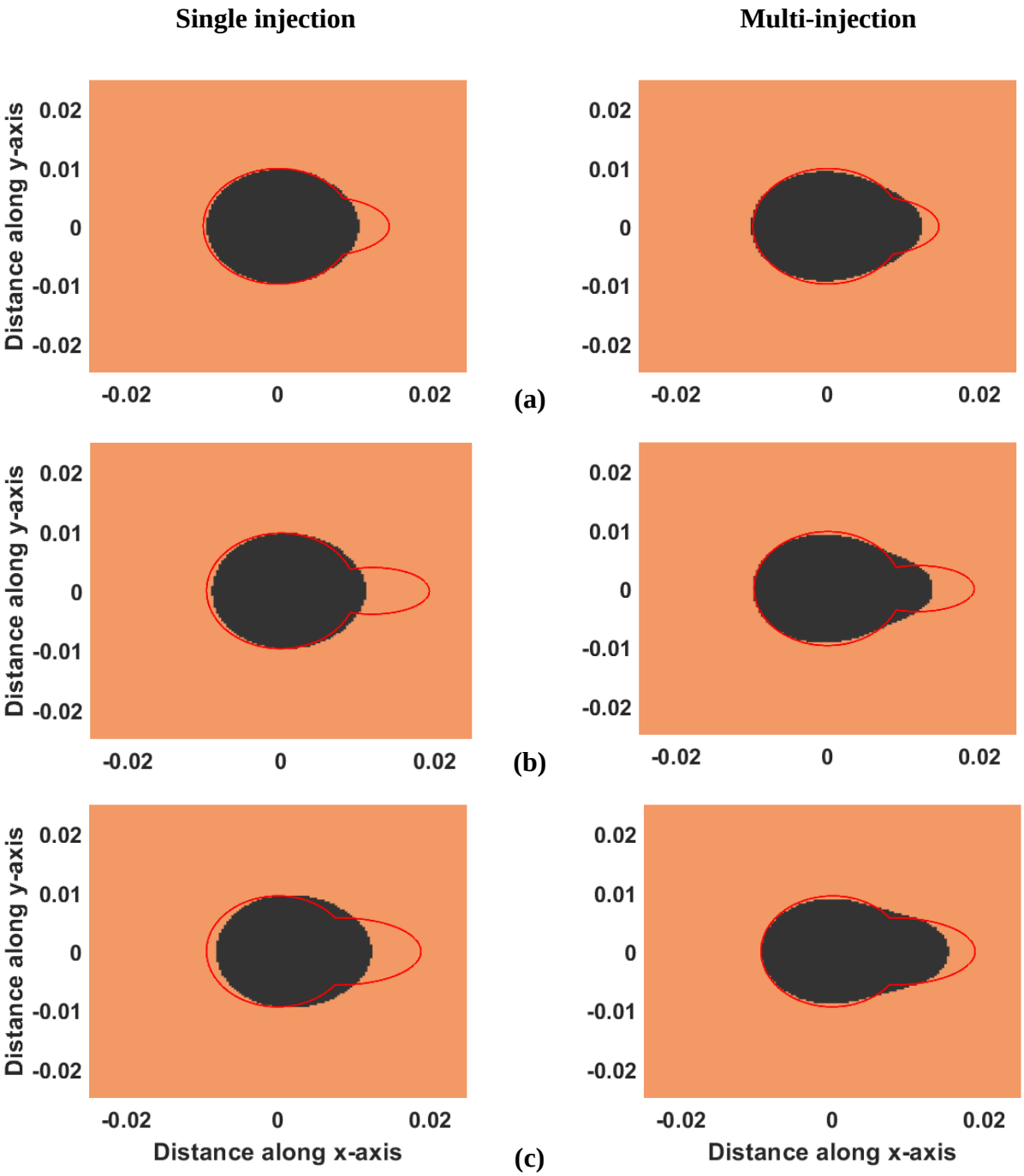

Figure 4.8. Comparison of spatial spread of thermal damage in tumor model **(a)** M1 **(b)** M4 **(c)** M6

The quantitative details of the therapeutic effects of MNPH in different categories of tumor shapes with single and multi-injection approaches are enumerated in Table 4.2. The table summarises the percentage of tumor and healthy tissue volumes undergoing thermal damage in terms of C_D and $(CEM43)_{60}$ parameters. Additionally, HI parameters, as well as the percentage tumor volume above the MTT is also enumerated in the Table 4.2. It can be noted from this table that the thermal damage induced due to single and multi-injection is

comparatively similar in the tumors having small protrusion branches such, M1 and M2. As the volume of the protrusion branch increases, the thermal damage to the tumor tissue with a single injection reduces in terms of. C_D and $(CEM43)_{60}$. Similarly, other damaging parameters decrease with the increase in protrusion volume of the tumor with single injection during MNPH. However, with two injections, the decrement in thermal damage is smaller, even for tumors with a higher protrusion ratio.

Table 4.2. Heterogeneity, thermal dosimetry parameters attained in the considered shapes of tumors due to MNPH.

		Tumor Tissue					Healthy tissue	
Tumor models	$V_p/V\%$	Injections	HI	$(TV > 43)(\%)$	$\%C_D$	$\%(CEM43)_{60}$	$C_D\%$	$\%(CEM43)_{60}$
$M1$	3.34	1	2.58	86.23	92.44	72.14	2.39	0
		2	2.34	84.85	91.3	71.48	3.2	0.15
$M2$	4.94	1	2.63	85.98	91.75	72.31	3.61	0
		2	2.3	84.86	91.78	71.39	2.87	0.03
$M3$	6.21	1	2.66	85.42	91.16	72.11	2.56	0
		2	2.27	84.71	92.12	71.13	4.35	0
$M4$	8.54	1	2.89	82.57	86.61	71.57	7.57	0.02
		2	2.27	82.23	88.77	69.01	4.22	0.8
$M5$	13.13	1	3.26	79.25	83.55	69.55	10.79	1.75
		2	2.2	81.37	88.6	68.6	3.78	0.29
$M6$	16.4	1	3.44	77.17	81.77	67.95	12.19	2.84
		2	2.18	81.57	88.37	68.15	3.59	0.03

The quantitative comparison of single injection and multi-injection is demonstrated in Figure 4.9. The comparison of single and multi-injection approaches is shown with the plot of percentage tumor volume above the MTT i.e., 43℃ versus protrusion ratio (V_p / V). For better comparison, an additional case of tumor model with 20 % of the protrusion volume with an aspect ratio of 2.2 is also included in the plot. As can be seen from this plot that upto tumor protrusion ratio of 10% both single, as well as multi-injection strategies, have near similar therapeutic effects. However, when the volume of protrusion exceeds 10%, the percentage volume above MTT reduces sharply in a single injection. On the other hand, the therapeutic effect with multi- injections does not reduce substantially and approximately remains constant

even for high protrusion volume ratio. Thus, this figure indicates that when the protrusion volume becomes higher than 10%, the secondary injection should be considered in addition to the primary injection to enhance the therapeutic effects during MNPH.

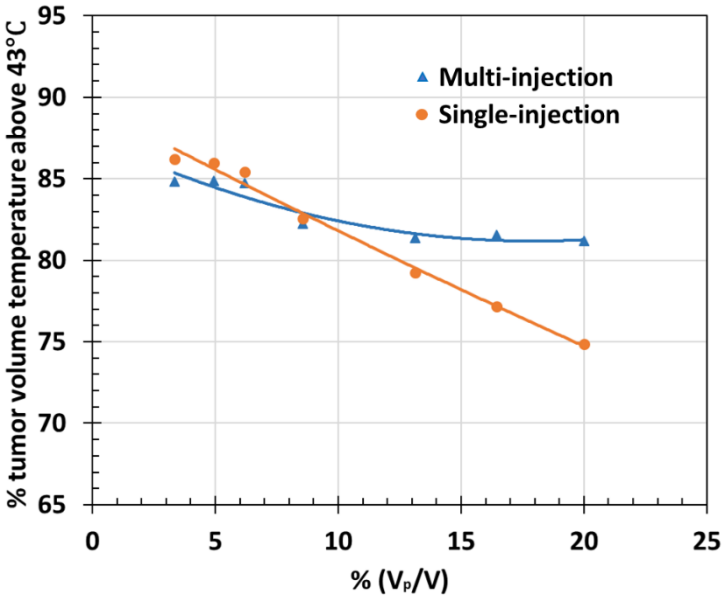

Figure 4.9. Plot between the percentage of tumor volume temperature above 43℃ and V_p/V (%) in single and muti-injection approach

Concluding, it can be inferred from the Table 4.2 and plot (Figure 4.9) that multi-injection strategy is more effective than a single injection during MNPH. However, the effectiveness of the multi-injection also depends upon the size of the protrusion branch. The tumors with the protrusion volume ratio (V_p / V) less than 10% show comparatively similar therapeutic effects with multi and single-injection approaches. However, when the protrusion branch volume ratio exceeds 10% of (V_p / V) the therapeutic effect with a single injection reduces significantly, while the multi-injection strategy retains its efficacy.

4.4 Discussion

The effectiveness of MNPH therapy is influenced by many factors, such as the shape/morphology of tumor volume, MNP distribution, physiology of tumor tissues, and magnetic field parameters. However, this chapter primarily focused on devising some criterion for injection strategy based on the shape or morphology of tumors. In general, the tumors are complex in shape and irregular in geometry. Thus, a portion of the tumor, especially the tumor periphery, remains below the therapeutic temperature [20,30] during MNPH therapy. Therefore, the therapeutic efficacy is greatly influenced by the shape of tumors. Several

investigations have shown that a single injection usually does not produce adequate thermal damage throughout the tumor volume [19,30,44] due to the limitation in uniform distribution of MNP. For large-sized and irregular tumors, a multi-site injection is more suitable in order to get a sufficient thermal effect throughout the entire tumor volume [9,20,30]. However, the multi-injection strategy introduces additional complications regarding injection site selection and clinical delivery of the required MNP dose at several injection points in the tumor [20]. Therefore, in this study, attempts have been made to predict the location of the injection point based on the tumor morphology and to develop a criterion for the selection of multi-injection over single injection strategy for MNPH. In the current work, injections are categorized into primary and secondary injections. The optimum tumor volume under secondary injection and its location is evaluated based on computational analysis on the 3D tumor models that have unidirectional spatial growth of tumor mass. However, the size and shape of the protrusion vary in each tumor model. The secondary injection dose is delivered at the centroid of a zone of influence. The zone of influence of secondary injection is within distance $'kr'$ from the branch node. Results indicate that a value of $'k'$ between 0.7 and 0.8 gives the minimum heterogeneity of temperature in tumor tissue. However, this prediction is based on the MNPH simulations conducted on the tumors having unidirectional protruding branch. The other assumptions include the idealizations of the parameters such as Gaussian distribution of MNP after its injection in the tissue, isotropic tissue properties, homogeneous magnetic field intensity, and the location of the tumor away from any major blood vessels. The comparison of single and multi-injection strategies show that the multi-injection approach is effective in case of the protrusion volume is approximately more than 10% of total tumor volume. Furthermore, the current computational results also contain error associated with the mathematical approximations, however, results may work as a guiding tool for experimental works and clinical trials.

4.5 Closing Remarks

In this work, a guiding criterion has been established for an intratumoral multi-injection strategy for irregularly shaped tumors. The optimum locations of primary and secondary injection are evaluated with computational analysis using MNPH in 3D tumor models. The comparison of multi and single injection shows that secondary injection is effective in case the protrusion volume is greater than 10% of total tumor volume.

Chapter 5

Effect of the position of tumor with respect to blood vessel on the magnetic hyperthermia therapy

5.1 Introduction

In previous chapters, attempts have been made to investigate the effects of tumor morphologies on MNPH and to devise an MNP injection criterion for arbitrary shaped tumor. In both studies, position of the tumor is considered far from any major BVs (blood vessels). Thus, the BVs are not included in the tumor model. However, if BV is present near the tumor, it will affect the thermo regulation of the tissue during hyperthermia therapy. The large BVs can significantly remove the induced thermal energy from the treatment region [112–114]. Few previous works have reported the effect of BVs on hyperthermia therapy [112–115]. It has been reported that high blood velocity or large BVs can significantly influence the therapeutic region [47,51,53,114]. Paul et al. [112] have investigated that increasing the BVs size from 0.6mm to 3mm drops the tumor surface temperature nearly 1℃ with laser assisted thermotherapy. Similarly, Astefanoaei et al. [116] have also reported the drop in peak temperature nearly 1℃ with varying the BVs diameter from 0.4 to 1mm during MNP based hyperthermia. Also, the author investigated that the peak temperature in the tissue is 2℃ higher in the absence of any blood vessel near the tumor during hyperthermia therapy, incomparison to the presence BV near the tumor. Therefore, poor vascular system and low blood velocity are favorable conditions for the treatment. However, most of these studies [47,51,113,114] modelled hypothetical cylindrical BVs embedded in randomly shaped tumors and simulated hyperthermia therapy by varying the BV size and flow rate. Also, there is limited research on the quantitative analysis of thermal dose and cooling effect by the BVs on MNPH. Thus, in this work, the effects of proximity of BVs on MNPH are investigated. For this investigation, tumor model is constructed from DICOM images of actual liver tissue [117]. For the high-fidelity simulation of magnetic hyperthermia therapy, we have utilized the 3D-Slicer software [118] to extract the actual liver model, containing tumor and BVs. In this analysis the bio-heat transfer and fluid flow simulations are done in the actual liver model through COMSOL Multiphysics. The proximity of the BV with respect to the tumor is one of the key parameters that will affect the thermoregulation of the heat during MNPH. Thus, the effect this parameter on the MNPH therapy (temperature elevation and thermal dose) is investigated through MNPH simulation.

5.2 Material and methods

5.2.1 Physical model

Solid tumors can grow in various organs throughout the body [119]. In this study, we have utilized DICOM images of the liver, which are part of the sample data provided by the open-source 3D Slicer software [63]. The DICOM image of the liver comprises a solid tumor, the primary BVs (portal and hepatic) and the surrounding healthy tissue. The images undergo processing with the 3D Slicer software, enabling the extraction of the tumor, major BVs, and the surrounding healthy section of the liver. The 3D Slicer software is used for segmenting and refining the liver, BVs, and tumor surfaces for accurate representation [118]. Figure 5.1 illustrates the image of the liver model, encompassing both the tumor and the BVs in the axial, coronal and sagittal plane. The tumor is represented in pale yellow, the hepatic BV in blue, the portal BV in light red, and the remaining liver tissue in bronze. Figure 5.2 illustrate the 3D model of liver, including tumor and BVs. Individual 3D model of the tumor and BVs (portal and hepatic veins) are also shown in this figure. Each segment of the tumor model is colour-coded for differentiation. Additionally, each segment undergoes individual manual smoothing, and the resulting surfaces are saved in the STL (stereolithography) format. The intricate and complex vascularization of the complete liver is extensive and unnecessary. Thus, only a significant portion of the wide hepatic and portal BVs, measuring approximately 11 cm and 10 cm in length, respectively, in close proximity to the tumor, is extracted, and their surfaces smoothed (as depicted in Figure 5.2). The tumor model is irregular in shape and is divided into two distinct portions labelled T1 and T2 (Figure 5.2(b)). The volume of T1 is 3.61 cm^3, while the volume of T2 is 1.45 cm^3. The geometrical properties of both tumors are described in Table 5.1. The intestinal fluid surrounds the physical models, forming a cubic enclosure.

Table 5.1. Geometrical properties of tumor

Tumor	Lx-max (cm)	Ly-max (cm)	Lz-max (cm)	SA (cm^2)	V (cm^3)
T1	2.32	2.53	2.7	12.86	3.61
T2	1.76	1.58	1.33	6.73	1.45

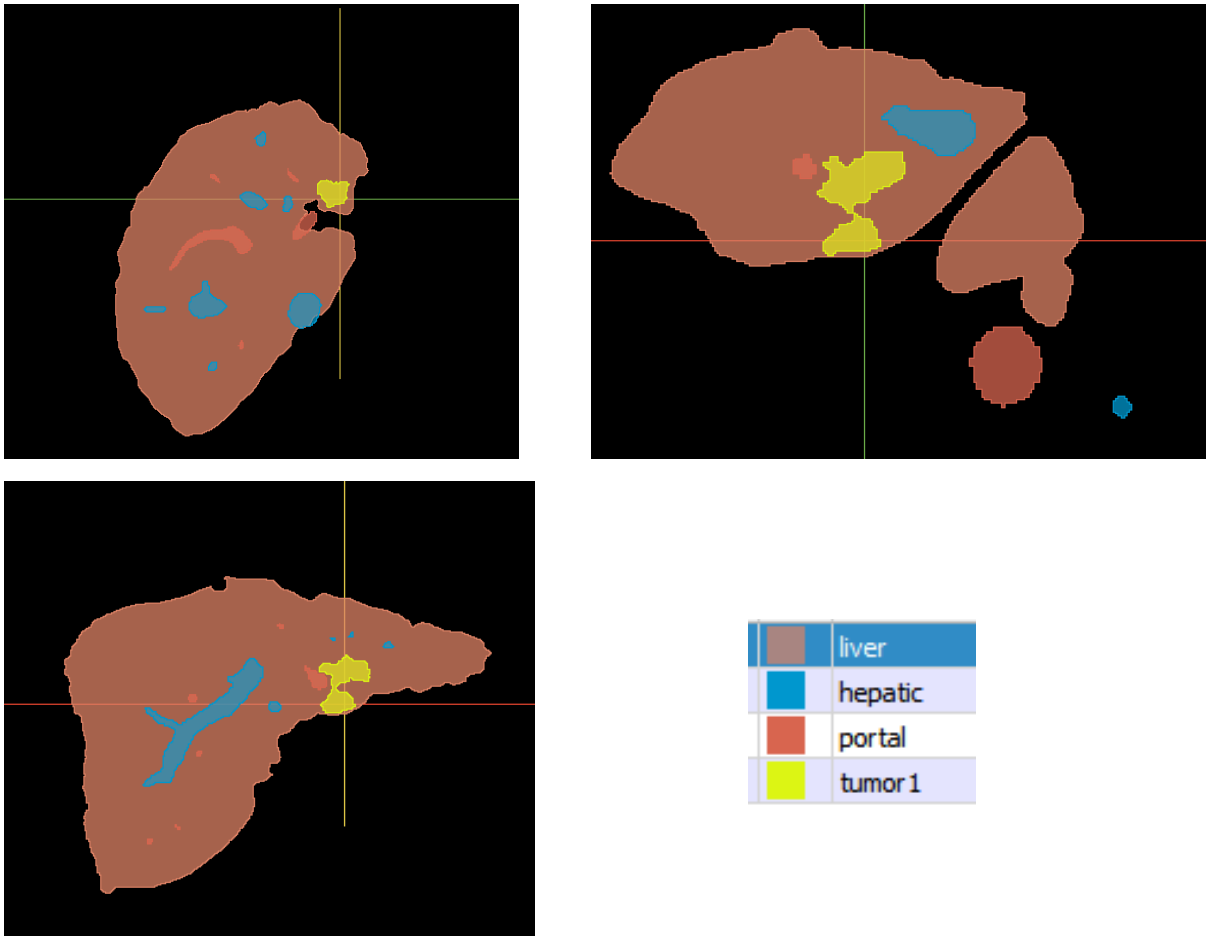

Figure 5.1. Depicts the tomography images of liver, tumor, portal and hepatic BV in the axial, coronal and sagittal plane.

The distance between the tumor model and the portal BV is approximately 6mm, while the distance from the tumor to the hepatic BV is approximately 36mm (as shown in Figure 5.3a). Both the hepatic and portal BV models have variable radii and are divided into two branches (lobes). The portal BV is situated in close proximity to the tumor. The proximity of this BV is parameterized with a d/R ratio. Here, 'd' represents the distance from the center of the portal BV to the tumor (as depicted in Figure 5.3), and 'R' denotes the portal BV radius corresponding to the tumor location. For the purpose of conducting a parametric analysis on MNPH four values of d/R ratio ranging from 1 to 2.6 are considered in this work. At ratio '1', the tumor surface (Figure 5.3b) coincides with the portal BV surface. During the parametric investigation of cooling effect using laser assisted thermotherapy by Paul et al. [112] have found that beyond the distance of 3.5 mm of tumor surface from BV, the cooling effect becomes negligible. According to their geometric model as radius of BV 1.5 mm, the calculated d/R is 2.33. Thus, we have considered four cases of different d/R ratio are shown in Figure 5.6 (from P1 to P4) and the value of d/R is given in Table 5.2.

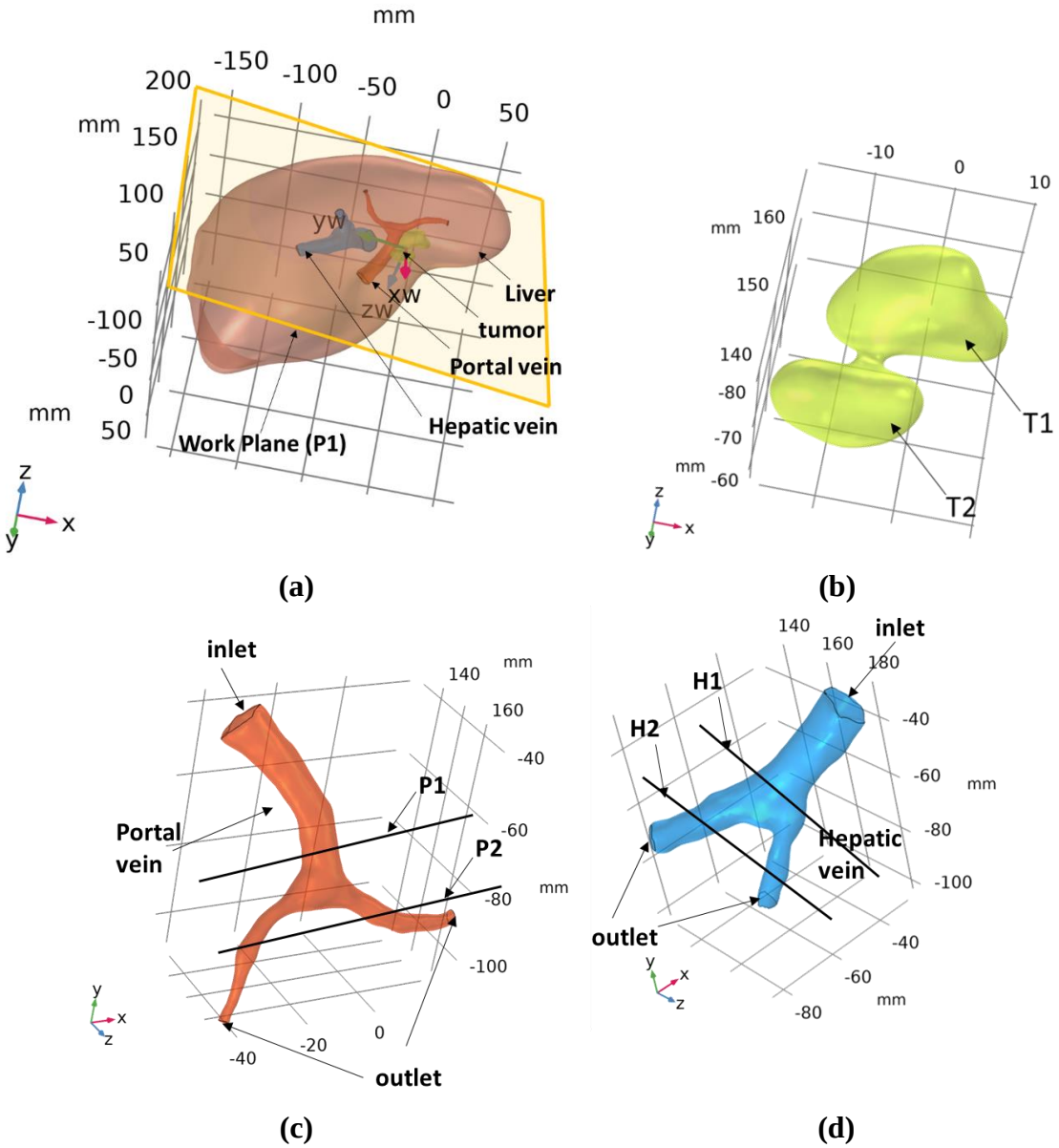

Figure 5.2. Three-dimensional model of **(a)** liver including tumor and BVs (portal and hepatic) **(b)** tumor **(c)** portal BV **(d)** Hepatic BV

Table 5.2. Details of four different tumor position in terms of d/R ratio

Models	P1	P2	P3	P4
d/R	2.6	2	1.4	1

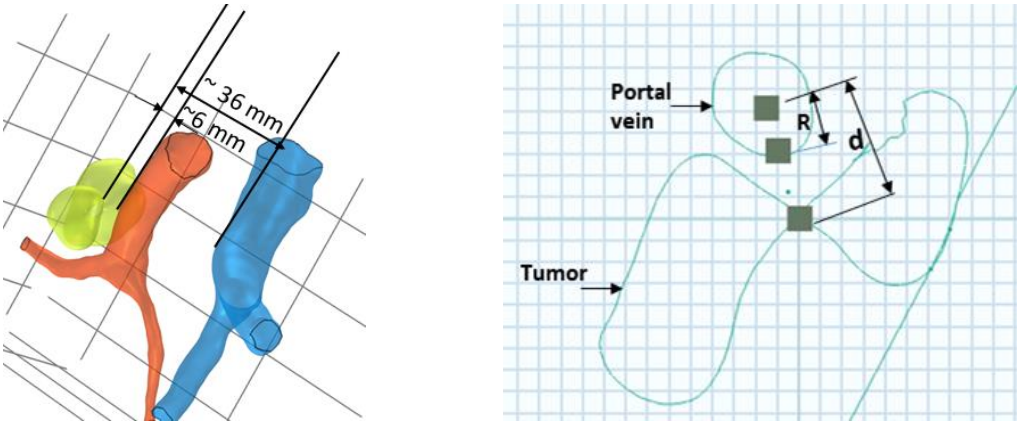

(a) **(b)**

Figure 5.3. Depicts **(a)** the distance between BVs and tumor, **(b)** the ‘d’ and ‘R’ distance to shift the tumor position from existing to near portal BV.

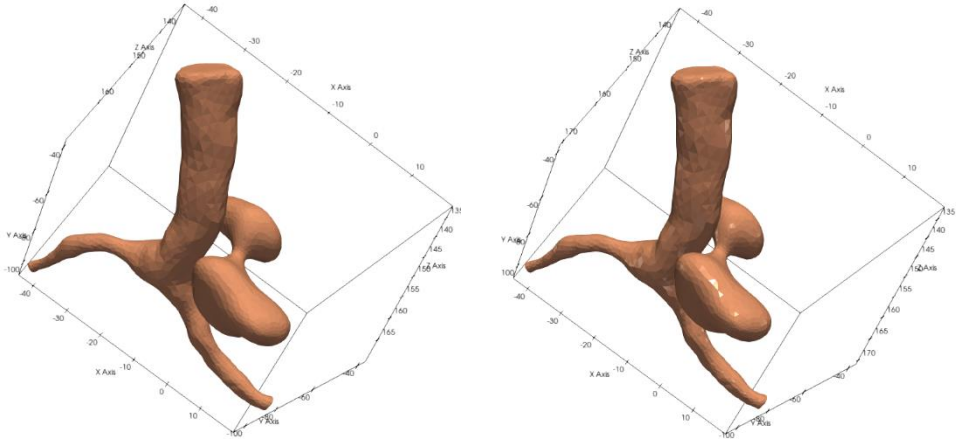

(a) **(b)**

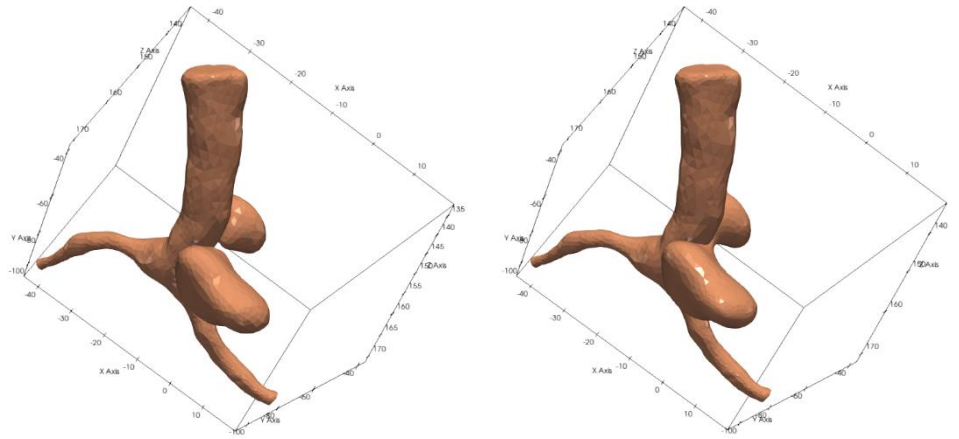

(c) **(d)**

Figure 5.4. Depiction of the portal BV and different tumor position **(a)** P1, **(b)** P2, **(c)** P3, **(d)** P4

5.2.2 Mathematical model

Blood flow in the liver tissue through a portal and hepatic BVs is considered laminar [120]. The blood flows in both hepatic and portal BVs are modelled by Navier Stoke's equation (equation (5.1)).

Fluid transport equations

$$\frac{d\rho_b}{dt} + \rho_b \nabla . \boldsymbol{u} = 0 \qquad (a)$$
$$\rho_b \frac{D\boldsymbol{u}}{Dt} = -\nabla \mathrm{p} - \nabla . \tau \qquad (b) \qquad 5.1$$
$$\tau = -\mu \left(\nabla \boldsymbol{u} + \nabla \boldsymbol{u^T} - \frac{\mathbf{2}}{\mathbf{3}} \nabla . \boldsymbol{u} \right) \qquad (c)$$

where, $\boldsymbol{u}$ is vector quantity represents the velocity of blood in x, y, and z directions. 'p' represents the pressure and $'\tau'$ represents the stress tensor. ρ_b and μ are physical properties of blood, represents density and viscosity, respectively. Equation 5.1a is the continuity equation According the literature, the total amount of blood flow in the average male liver is 1.5L/min. This value may vary according to person between 1 to 2L/min. The hepatic BV supplies blood flow nearly 25 % of total liver blood flow and remaining 75% flow through the portal BV [121].

To evaluate the temperature distribution in the tissue (tumor and healthy) and intestine fluid, the PBHT model has been used (equation 2.1). The heat interaction in the hepatic and portal BV are modelled using the convection -diffusion equation (5.2).

Heat transfer equation in fluids

$$(\rho C_p)_b \left(\frac{\partial T}{\partial t} + \boldsymbol{u} \nabla T \right) = \mathrm{k}_b \nabla^2 T \qquad 5.2$$

where ρ and C_p denotes the density and specific heat capacity. 'T' is the temperature in tissue and BV. The metabolic heat source (q_m) and perfusion coefficient (ω_b) are considered zero for the intestine fluid. The steady-state velocity field $\boldsymbol{u}$ is obtained from equation (5.1) is utilized in equation (5.2). The liver and tumor exhibit distinct thermo-physical properties, as depicted in "Chapter 2"-Table 2.1. The properties of the intestinal fluid are assumed to be equivalent to those of blood. The heat generated from the magnetic nanoparticles (MNP) hyperthermia is transferred to the liver and intestinal fluid.

5.2.3 Heat generation due to MNP in Tissues

In this study, we have considered the uniform MNP distribution within the 25% of tumor volume with a volume fraction (ratio of MNP volume to the MNP distributed tumor volume) 0.0064. According to in-vivo and in-vitro investigation, heat source spread within tumor lies between the 2.37 mm to 12 mm depending upon the different infusion rate and amount of injection [9,19,30]. The spatial spread radius of MNP in T1 and T2 tumor volume is 5.99 and 4.4 mm, respectively. The BNF starch nanoparticles as hyperthermia inducers are utilized for MNPH therapy. SLP of MNP are evaluated by a sixth-order polynomial equation reported by Soetart et al. [50] To ensure the safe application of MNPH, it is important to consider the product of magnetic field strength and frequency, which should not exceed 5 × 109 Am [26]. Therefore, the magnetic field strength of 20.5 kA/m and a frequency of 150 kHz are used for MNPH. The specific loss power (SLP) value calculated using the co-relation predicted by Soetart et al. [50] for these parameters is 50.64 W/(g of MNP).

5.2.4 Computational methodology and boundary conditions

The aforementioned momentum, bioheat, and heat transfer equations have been simulated using COMSOL. Multiphysics 5.6 on a Dell Precision Tower 5820 workstation. This software employs the finite element method (FEM) to discretize the governing differential equations. The software is routinely utilized for the simulation of heat transfer and fluid flow physics [122]. First, the momentum equation is solved in hepatic and portal BVs to evaluate the flow variable 'u'. The constant mass flow rate ($\dot{m}$) is given as the boundary condition at the inlet (as shown in Figure 5.2(c and d) and the non-slip condition is considered at the vessel's wall. The amount of flow rate in both hepatic and portal BVs is considered at inlet 0.375L/min and 1.125L/min, respectively. The velocity field 'u' is utilized in the heat transfer equation (equation (5.2)) for hepatic and portal BVs. The spatial temperature distribution (T) in the physical model is evaluated by solving the heat transfer equations (equations 5.1 and 5.2) in tissue (tumor and liver), hepatic and portal BVs, and intestine fluid simultaneously. The tumor is surrounded by the liver tissue and intestine fluid. The boundary of the intestine fluid is located at a significant distance from the tumor. Therefore, the core body temperature is assumed at the boundary of the intestine fluid. Similarly, the temperature of blood at the inlet of BVs is at the core body temperature. While at the interface between tissue and BVs, the continuity of temperature and heat flux conditions have been applied (equation (5.3)).

$$-k_{tis}\frac{dT}{d\eta} = -k_b\frac{dT}{d\eta} \qquad 5.3$$

5.3 Results

5.3.1 Velocity profile in hepatic and portal BV

The steady-state contour of the velocity profile in the hepatic and portal BV is depicted in Figure 5.5. Since the cross-sectional radii of the vessels vary along the path of the blood flow, thus the velocity profile also varies at different cross-sections. At the two different planes (P1, P2, H1, and H2, as shown in Figure 5.2 c and d), the velocity profile is depicted in both vessels (hepatic and portal). As both the vessels (hepatic and portal) are divided into two parts, thus size of the upper part is larger than the two lobes in both cases. The peak velocity in portal BV in the upper and its two lobes are nearly 20 cm/s and 40-50cm/s, respectively. The peak velocity in hepatic BV in the upper portion and its two lobes 4 cm/s and 10 cm/s, respectively.

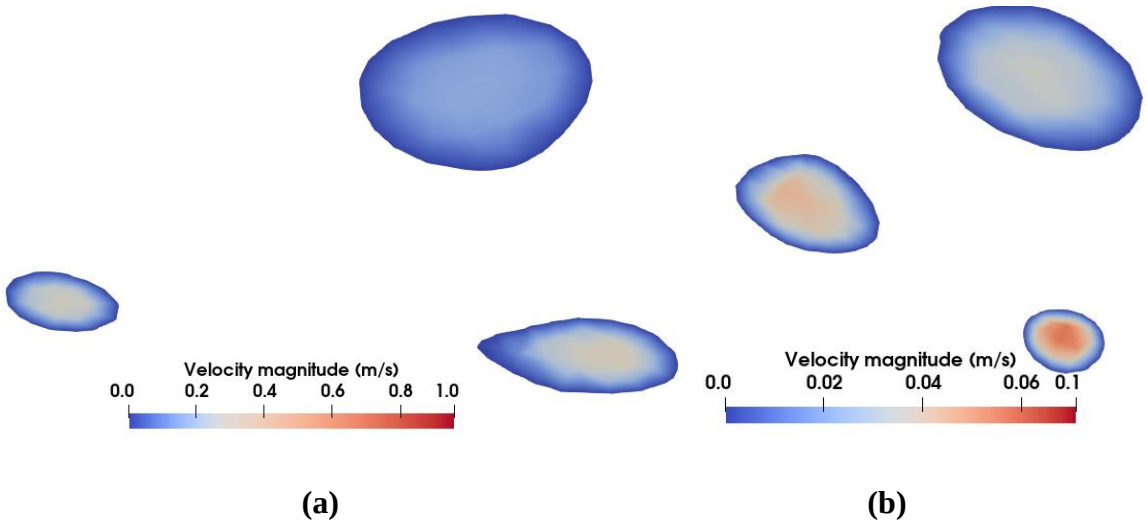

Figure 5.5. The velocity contours in **(a)** portal BV at P1 and P2 plane **(b)** hepatic BV at H1 and H2 plane.

5.3.2 Spatial temperature distribution

The MNPH. therapy is induced for 60 minutes in all tumor models. Figure 5.6 depicts the 2D spatial temperature profile just after 60 minutes in tumor and the portal BV, on the plane that passes through the injection sites and portal BV. It can be noted from this figure that temperature variation in the blood at the depicted cross-section of the portal BV is negligible. This observation has also been noted by previous researchers [51,114]. Because the amount of

thermal energy enters into the blood vessels is insufficient to significantly raise the temperature of high mass flow rate of blood.

The cooling effect due to the blood flow increases in the tumor as the tumor inches toward the portal BV as described in Table 5.3. Table 5.3, thermal dosimetry parameters are in terms of T_{90}, T_{10}, HI, and percentage tumor volume greater than therapeutic temperature. Because of the cooling effect of BV, the minimum temperature within 90% and 10 % tumor volume (T_{90} and T_{10} (Table 5.3)) decrease nearly 2℃ from P1 to P4 models. The HI index, as discussed in Chapter 3, section 3.3.3, depends on the T_{90} and T_{10} temperatures. The value HI index increases from the P1 to P4 model as shown in Table 5.3.

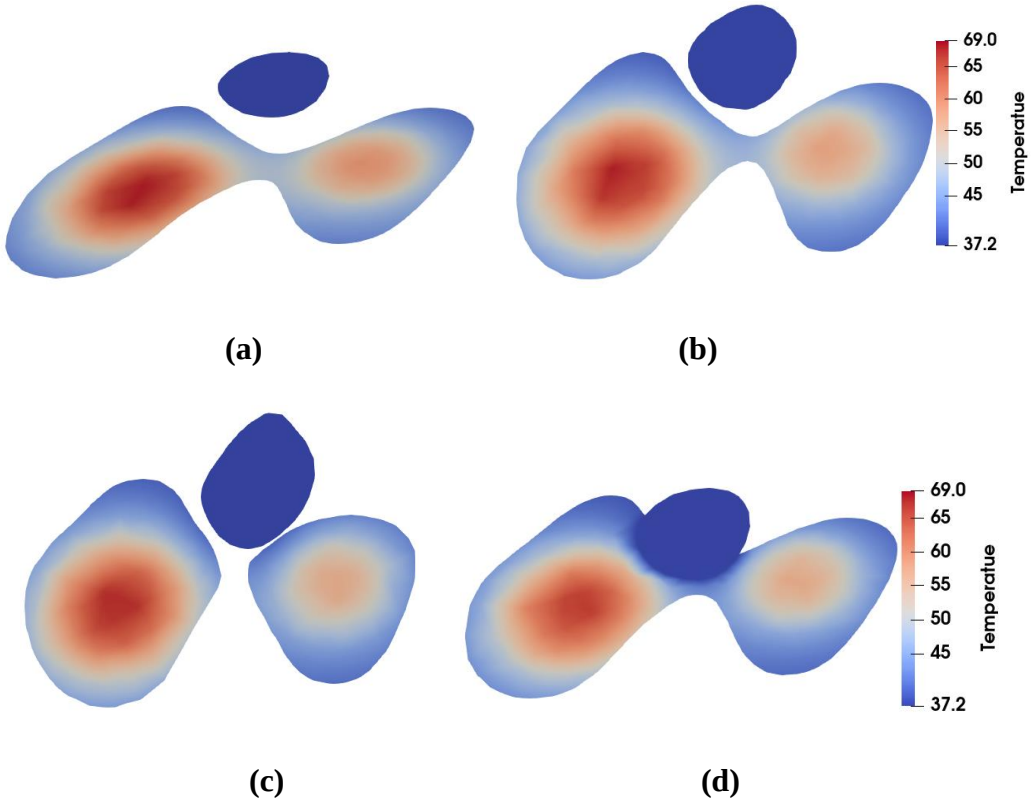

Figure 5.6. Depiction of the 2D temperature profile in tumor and portal BV at different tumor position at (a) P1, (b) P2, (c) P3, (d) P4

This indicates that with the increase in the cooling effect by the proximity of the blood vessel, results in uneven temperature elevation within the tumor. Thus, the peak temperature in the P4 tumor position (as indicated in Figure 5.7) is lower than in the other cases. The maximum temperature achieved during MNPH is 69.24℃ for the P1 model. It is important to note that the therapeutic effect in the tumor is considered effective if most of the tumor volume

(TV) is above the 43℃ temperatures. The thermally affected TV reduces up to 17 percentage from the P1 to P4 model during MNPH.

Table 5.3. Heterogeneity, thermal dosimetry parameters attained in the considered cases due to MNPH Tumor

Models	T_{90}	T_{10}	HI	T_{max}	$TV > 43℃$
P1	41.15	58.75	4.24	69.24	76.72
P2	40.75	58.3	4.68	68.92	71.9
P3	39.8	58.0	6.5	68.5	66.1
P4	39.32	56.6	7.4	67.32	59.15

Figure 5.7 depicts the variation in peak temperature and the tumor volume above the therapeutic temperature within the tumor over the time during MNPH for all tumor models. The steady-state temperature is achievedd after 10 minutes in all cases (Figure 5.7a). Due to the high convection effect induced by the BV for d/R = 1, the elevation of maximum temperature for this case (P4) is minimum. From Figure 5.7 (b) plot, it can be noted that, within 10 minutes, more than 40 percent of tumor volume gains temperature higher than the therapeutic range. As time progresses, the tissue volume above the therapeutic temperature increases, however, the rate of increment slows down after 10 minutes. It should be noted from this plot that the maximum thermal dose is induced to the tumor having the highest value of d/R ratio i.e., 2.6. Furthermore, minimum therapeutic effects are induced in the tumor model with a d/R ratio equal to 1 (for the case portal BV touches the tumor boundary). Thus, the effectiveness of therapy decreases as BV inches towards the tumor.

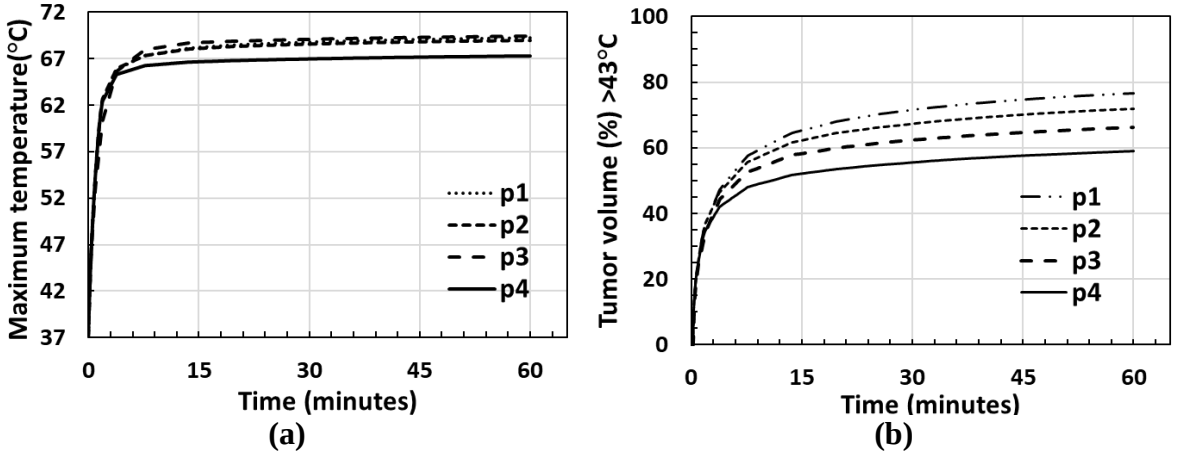

Figure 5.7. Variation of **(a)** maximum temperature in tissue with time, **(b)** percentage tumor volume above therapeutic range with time.

The cooling effect on the MNPH therapy caused by the larger BV near the tumor is summarised in Figure 5.8. Figure 5.8 illustrates the plot between the percentage tumor volume above the therapeutic temperature (43℃) and the d/R ratio. The plot shows that the therapeutic effects (thermal dose during MNPH) in tumor are highly affected by the proximity of BV. As the d/R ratio decreases from 2.6 to 1, there is an approximate 20% reduction in therapeutic efficacy. In other words, as the distance between the tumor and the BV increases the impact of blood flow on the MNPH therapy diminishes.

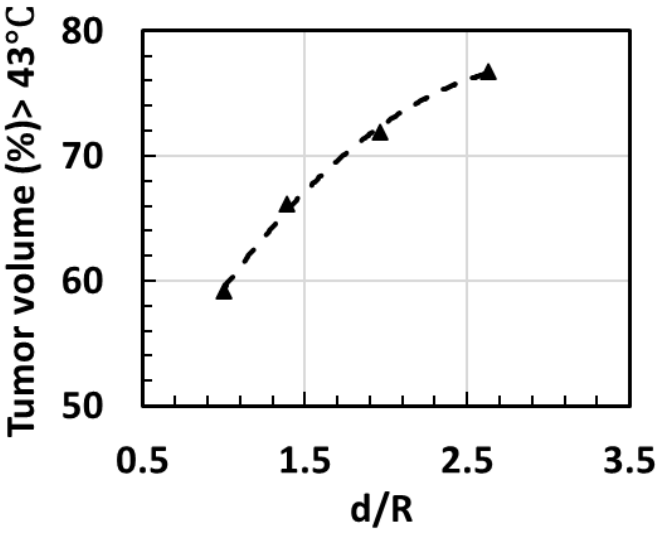

Figure 5.8. Variation the percentage tumor volume above therapeutic range with d/R ratio.

5.4 Discussion

The efficacy of MNPH therapy in treating tumors is significantly influenced by various factors, one of which is the cooling effect caused by major BVs when heating the malignant tissue. Various researchers have shown that the therapeutic effect in tumor significantly reduces near the BVs [47,51,114]. However, there has been limited exploration into quantifying the therapeutic region affected by the BVs. In the present study, we have simulated the MNPH therapy in the real tumor model including the BVs (portal and hepatic) and surrounding healthy tissue. We assume a uniform velocity at the inlet of the BVs for simplicity; notably, previous investigation by Horng et al. [123], have indicated that the pulsatile velocity profile has only minor differences in the thermal lesion region when compared to a uniform or parabolic velocity profile. Navier-Stokes equation is used to calculate the steady-state velocity profile within the BVs.

The temperature distribution in both the tissue (tumor and healthy) and the BVs is computed using a coupled bioheat equation and convection-diffusion equation. This distance between the

BV and the tumor is parameterized and expressed as the d/R ratio. Results reveal that the therapeutic effects decrease from approximately 78% to 58% as the d/R ratio varies from 2.5 to 1, respectively. It's important to note that in our computational investigation, we have made certain simplifying assumptions, such as assuming a uniform velocity profile at inlet and a homogenous distribution of MNP. Nevertheless, this study provides valuable insights into predicting the reduction in therapeutic effectiveness due to the presence of BVs.

5.5 Closing Remarks

Effects of blood carrying vessel on the MNPH therapy have been studied. Results indicate that the therapeutic effect significantly reduces if the tumor is close to the BV. The cooling effect of the BV is parameterized by the d/R ratio. With increasing the d/R ratio beyond 2.5, the cooling effect curve begins to flatten.

Chapter 6

Conclusion and Future Scope

6.1 Summary and Conclusion

The present work describes the development of the FV-IBM method for the numerical simulation of the bioheat physics in arbitrary shaped tumor models. Using FV-IBM, the simulation is conducted in the Cartesian grid structure, instead of body-fitted grid structure used by other numerical technique. The boundary conditions are enforced at the immersed cells using quadratic and linear functions. The accuracy of the numerical method is validated by comparing the FV-IBM solution with analytical and previously reported numerical results for heat and bioheat transfer problems. The L2 norm error for this numerical methodology demonstrates that the scheme is second-order accurate. Subsequently, the FV-IBM scheme is employed to simulate the bioheat model in a realistic 3D liver tumor model. The 3D liver model, including the tumor, is extracted from DICOM images using the open-source 3D Slicer software. The numerical results of the spatial heating are compared to experimental data and COMSOL results considering both uniform and Gaussian distributions of magnetic nanoparticles (MNP).

The developed FV-IB framework has been utilized to investigate the influence of tumor shapes on MNP-based hyperthermia therapy. Three different tumor shapes (oblate, prolate, and egg-shaped) with equal volumes are considered, and a single injection of the same amount of MNP is administered. The therapeutic effect in each tumor is evaluated using a shape factor, and it is found that an increase in the shape factor leads to a decrease in the therapeutic effect. Moreover, the study proposes an empirical relationship between the therapeutic effect and the shape factor derived from the obtained numerical results.

In order to improve the therapeutic effect in tumors with arbitrary shapes or high shape factors, a guiding criterion has been developed for an intratumoral multi-injection strategy. The optimal positions for primary and secondary injections are determined through numerical simulations conducted on a 3D tumor model. The tumor volume is divided into two parts: the core volume and the protruding volumes. The primary injection is assumed to be in the tumor core, while secondary injections are administered in the protruding volumes. It should be emphasized that this strategy proves to be effective when the protruding volume constitutes more than 10% of the total tumor volume.

To investigate the cooling effect induced by major blood vessel on MNPH, another supplementary study is conducted on a real liver tumor that encompasses two major blood vessels, namely the portal and hepatic vessels. A parametric investigation is performed by varying the tumor's proximity to the blood vessels, and the results reveal a sharp increase in the cooling effect as the tumor gets closer to the blood vessels. Interestingly, the cooling effect diminishes when the distance ratio (d/R) exceeds '2.5'.

The present study provides a comprehensive analysis, beginning with the development of a numerical FV-IBM scheme for the bioheat equation. This scheme is then implemented to simulate the MNPH therapy in arbitrary tumor shapes and investigate the effects of tumor shapes, multi-injection strategies, and the cooling effect of blood vessels.

6.2 Scope for future study

MNP based hyperthermia therapy is numerically investigated using the FV-IB method in the present work. Many challenges and issues in experimental and computational modelling should be addressed and can be worked on in a future extension of this work.

In the present MNP hyperthermia have considered the Gaussian or uniform MNP distribution profile. In previous studies, some experimental studies have reported the Gaussian profile for the heat source. However, in order to accurate modelling of MNP distribution in tissue requires more experimental data. Some researchers have utilized a continuum approach to computationally model the MNP distribution in tissue by solving the Darcy and MNP transport equations. This approach overlooks the individual behavior of the particles within the tissue. On the other hand, the discrete element method (DEM) approach is an emerging high-fidelity simulation method that allows for the analysis of the behavior of each individual particle within the tissue.

The specific loss power (SLP) of MNP, which determines their ability to generate heat in the tissue, is another crucial factor. In this study, we employed a sixth-order polynomial relation based on experimental data for BNF starch MNP at a fixed frequency to evaluate the SLP. Although a theoretical Rosensweigh model is available in the literature for calculating the SLP, it is prone to considerable errors when measuring the heating value [88,124,125]. Therefore, future research can focus on developing accurate models that incorporate the properties of MNP and the magnetic field parameters such as frequency and magnetic field strength.

Despite the significant advantages and successful outcomes observed in MNPH therapy, its routine clinical establishment necessitates thoroughly exploring potential side effects and post-therapy outcomes. A clinical trial by [126] reported an absence of systematic toxicity even in a 17.5-month patient follow-up. However, certain patients experienced side effects during the therapy, such as skin burns, elevated blood pressure, and increased pulse rates. In parallel, in vitro investigations have indicated that elevated concentrations of MNPs can induce cell damage and toxicity [127]. However, further in vivo investigations are necessary to explore potential side effects and post-therapy outcomes associated with concentrations of MNPs , as well as to assess their toxicity.

List of Publications

Referred journals:

1. Amritpal Singh, and Neeraj Kumar. "Parameterizing the effects of tumor shape in magnetic nanoparticle thermotherapy through a computational approach". **Journal of Heat Transfer** (2022). **[SCI_IF 1.855]**
2. Amritpal Singh and Neeraj Kumar. "A coupled finite-volume immersed boundary method for the simulation of bioheat transfer in 3D complex tumor". **Engineering with Computers** (2023). **[SCI_IF 8.083].**

International Conferences:

1. Amritpal Singh, Neeraj Kumar. “Immersed boundary method-based simulation for bioheat model in complex shape tissue”. **UKACM2022- conference paper**
2. Amritpal Singh, and Neeraj Kumar. “Evaluation of the cooling effect due to the presence of major blood vessel on the magnetic hyperthermia therapy” **ICHMT 2023 conference paper (Submitted)**

Under review

1. Amritpal Singh, and Neeraj Kumar. “Estimation of the injection criteria for optimizing the magnetic hyperthermia therapy based on tumor morphology”. **(Under review)**

Bibliography

[1] World Health Organization, Cancer. (2023). https://www.who.int/news-room/fact-sheets/detail/cancer (accessed August 2, 2023).

[2] V. Kulothungan, K. Sathishkumar, S. Leburu, T. Ramamoorthy, S. Stephen, D. Basavarajappa, N. Tomy, R. Mohan, G.R. Menon, P. Mathur, Burden of cancers in India - estimates of cancer crude incidence, YLLs, YLDs and DALYs for 2021 and 2025 based on National Cancer Registry Program, BMC Cancer. 22 (2022) 1–12. https://doi.org/10.1186/s12885-022-09578-1.

[3] P. Mathur, K. Sathishkumar, M. Chaturvedi, P. Das, K.L. Sudarshan, S. Santhappan, V. Nallasamy, A. John, S. Narasimhan, F.S. Roselind, Cancer Statistics, 2020: Report From National Cancer Registry Programme, India, JCO Glob. Oncol. (2020) 1063–1075. https://doi.org/10.1200/go.20.00122.

[4] MINISTRY OF HEALTH & FAMILY WELFARE, INDIA, Natl. Cancer Control Program. (2023). https://main.mohfw.gov.in/sites/default/files/1493693747note_0.pdf (accessed July 2, 2023).

[5] C.E. DeSantis, C.C. Lin, A.B. Mariotto, R.L. Siegel, K.D. Stein, J.L. Kramer, R. Alteri, A.S. Robbins, A. Jemal, Cancer treatment and survivorship statistics, 2014, CA. Cancer J. Clin. 64 (2014) 252–271. https://doi.org/10.3322/caac.21235.

[6] J. Boivin, Second cancers and other late side effects of cancer treatment.A review, Cancer. 65 (1990) 770–775. https://doi.org/10.1002/1097-0142(19900201)65:3+<770::AID-CNCR2820651323>3.0.CO;2-8.

[7] S. Müller, Magnetic fluid hyperthermia therapy for malignant brain tumors-an ethical discussion, Nanomedicine Nanotechnology, Biol. Med. 5 (2009) 387–393. https://doi.org/10.1016/j.nano.2009.01.011.

[8] G. Bellizzi, O.M. Bucci, Magnetic NanoParticle Hyperthermia, in: L. Crocco, I.S. Karanasiou, R.C. Conceição, M.L. James (Eds.), Emerg. Electromagn. Technol. Brain Dis. Diagnostics, Monit. Ther., First, Springer Cham, 2018: pp. 129–191. https://doi.org/https://doi.org/10.1007/978-3-319-75007-1.

[9] M. Salloum, R. Ma, L. Zhu, An in-vivo experimental study of temperature elevations in animal tissue during magnetic nanoparticle hyperthermia, Int. J. Hyperth. 24 (2008)

589–601. https://doi.org/10.1080/02656730802203377.

[10] M. Dewhirst, S. Das, P. Stauffer, O. Craciunescu, Z. Vujaskovic, D. Thrall, Chapter 21 - Hyperthermia, in: L.L. Gunderson, J. Tepper (Eds.), Clin. Radiat. Oncol., Third Edit, Elsevier Inc., 2012: pp. 385–403. https://doi.org/https://doi.org/10.1016/B978-1-4377-1637-5.00021-3.

[11] P. Wust, B. Hildebrandt, G. Sreenivasa, B. Rau, J. Gellermann, H. Riess, R. Felix, P. Schlag, Hyperthermia in combined treatment of cancer, Lancet Oncol. 3 (2002) 487–497. https://doi.org/10.1016/S1470-2045(02)00818-5.

[12] S. Phatak, H. Natesan, J. Choi, R. Sweet, J. Bischof, Heat Transfer in Biology and Biological Systems, in: F.A. Kulacki, S. Acharya, R. Devireddy, V.K. Dhir (Eds.), Handb. Therm. Sci. Eng., Springer International Publishing, 2018: pp. 2279–2301. https://doi.org/10.1007/978-3-319-26695-4_21.

[13] J. Van der Zee, Heating the patient: a promising approach?, Ann. Oncol. 13 (2002) 1173–1184. https://doi.org/https://doi.org/10.1093/annonc/mdf280.

[14] C.S.S.R. Kumar, F. Mohammad, Magnetic nanomaterials for hyperthermia-based therapy and controlled drug delivery, Adv. Drug Deliv. Rev. 63 (2011) 789–808. https://doi.org/https://doi.org/10.1016/j.addr.2011.03.008.

[15] P.S. Yarmolenko, E.J. Moon, C. Landon, A. Manzoor, D.W. Hochman, B.L. Viglianti, M.W. Dewhirst, Thresholds for thermal damage to normal tissues: An update, Int. J. Hyperth. 27 (2011) 320–343. https://doi.org/10.3109/02656736.2010.534527.

[16] A. Chicheł, J. Skowronek, M. Kubaszewska, M. Kanikowski, Hyperthermia - Description of a method and a review of clinical applications, Reports Pract. Oncol. Radiother. 12 (2007) 267–275. https://doi.org/10.1016/S1507-1367(10)60065-X.

[17] R. Dua, S. Chakraborty, A novel modeling and simulation technique of photo–thermal interactions between lasers and living biological tissues undergoing multiple changes in phase, Comput. Biol. Med. 35 (2005) 447–462. https://doi.org/https://doi.org/10.1016/j.compbiomed.2004.02.005.

[18] V. Satish, J. Kumar, R. Repaka, Analysis of Ablation Volume Produced During Microwave Ablation of Breast Cancerous Lesion Using Fourier and Non-Fourier Models, in: ASME Int. Mech. Eng. Congr. Expo., 2019: p. V003T04A038.

https://doi.org/10.1115/IMECE2019-10800.

[19] A. Attaluri, R. Ma, Y. Qiu, W. Li, L. Zhu, Nanoparticle distribution and temperature elevations in prostatic tumours in mice during magnetic nanoparticle hyperthermia, Int. J. Hyperth. 27 (2011) 491–502. https://doi.org/10.3109/02656736.2011.584856.

[20] M. Salloum, R. Ma, L. Zhu, Enhancement in treatment planning for magnetic nanoparticle hyperthermia: Optimization of the heat absorption pattern, Int. J. Hyperth. 25 (2009) 309–321. https://doi.org/10.1080/02656730902803118.

[21] F.A. Duck, Physical Properties of Tissue. A Comprehensive Reference Book, Academic press, London, 2013. https://doi.org/https://doi.org/10.1016/C2009-0-02755-X.

[22] A. Matsumine, K. Takegami, K. Asanuma, T. Matsubara, T. Nakamura, A. Uchida, A. Sudo, A novel hyperthermia treatment for bone metastases using magnetic materials, Int. J. Clin. Oncol. 16 (2011) 101–108. https://doi.org/10.1007/s10147-011-0217-3.

[23] I. Negut, V. Grumezescu, Nanoparticles and hyperthermia, in: G. Alexandru Mihai (Ed.), Biomed. Appl. Nanoparticles, William Andrew Publishing, 2019: pp. 63–90. https://doi.org/10.1016/b978-0-12-816506-5.00012-7.

[24] R.E. Rosensweig, Heating magnetic fluid with alternating magnetic fiel, J. Magn. Magn. Mater. 252 (2002) 370–374. https://doi.org/10.1016/S0022-5347(17)32321-2.

[25] Z. Hedayatnasab, F. Abnisa, W.M.A.W. Daud, Review on magnetic nanoparticles for magnetic nanofluid hyperthermia application, Mater. Des. 123 (2017) 174–196. https://doi.org/10.1016/j.matdes.2017.03.036.

[26] S. Dutz, R. Hergt, Magnetic nanoparticle heating and heat transfer on a microscale: basic principles, realities and physical limitations of hyperthermia for tumour therapy, Int. J. Hyperth. 29 (2013) 790–800. https://doi.org/10.3109/02656736.2013.822993.

[27] R.R. Shah, T.P. Davis, A.L. Glover, D.E. Nikles, C.S. Brazel, Impact of magnetic field parameters and iron oxide nanoparticle properties on heat generation for use in magnetic hyperthermia, J. Magn. Magn. Mater. 387 (2015) 96–106. https://doi.org/https://doi.org/10.1016/j.jmmm.2015.03.085.

[28] D.E. Bordelon, C. Cornejo, C. Grttner, F. Westphal, T.L. DeWeese, R. Ivkov, Magnetic nanoparticle heating efficiency reveals magneto-structural differences when characterized with wide ranging and high amplitude alternating magnetic fields, J. Appl.

Phys. 109 (2011) 124904. https://doi.org/10.1063/1.3597820.

[29] I. Raouf, S. Khalid, A. Khan, J. Lee, H.S. Kim, M.-H. Kim, A review on numerical modeling for magnetic nanoparticle hyperthermia: Progress and challenges, J. Therm. Biol. 91 (2020) 102644. https://doi.org/https://doi.org/10.1016/j.jtherbio.2020.102644.

[30] M. Salloum, R.H. Ma, D. Weeks, L. Zhu, Controlling nanoparticle delivery in magnetic nanoparticle hyperthermia for cancer treatment: Experimental study in agarose gel, Int. J. Hyperth. 24 (2008) 337–345. https://doi.org/10.1080/02656730801907937.

[31] X. Wang, H. Gu, Z. Yang, The heating effect of magnetic fluids in an alternating magnetic field, J. Magn. Magn. Mater. 293 (2005) 334–340. https://doi.org/10.1016/j.jmmm.2005.02.028.

[32] N. Mahesh, N. Singh, P. Talukdar, Investigation of a breast cancer magnetic hyperthermia through mathematical modeling of intratumoral nanoparticle distribution and temperature elevations, Therm. Sci. Eng. Prog. 40 (2023) 101756. https://doi.org/https://doi.org/10.1016/j.tsep.2023.101756.

[33] M. Johannsen, U. Gneveckow, L. Eckelt, A. Feussner, N. Waldöfner, R. Scholz, S. Deger, P. Wust, S.A. Loening, A. Jordan, Clinical hyperthermia of prostate cancer using magnetic nanoparticles: Presentation of a new interstitial technique, Int. J. Hyperth. 21 (2005) 637–647. https://doi.org/10.1080/02656730500158360.

[34] M. Johannsen, B. Thiesen, A. Jordan, K. Taymoorian, U. Gneveckow, N. Waldöfner, R. Scholz, M. Koch, M. Lein, K. Jung, S.A. Loening, Magnetic fluid hyperthermia (MFH) reduces prostate cancer growth in the orthotopic Dunning R3327 rat model, Prostate. 64 (2005) 283–292. https://doi.org/10.1002/pros.20213.

[35] M. Johannsen, U. Gneveckow, L. Eckelt, A. Feussner, N. Waldöfner, R. Scholz, S. Deger, P. Wust, S.A. Loening, A. Jordan, Clinical hyperthermia of prostate cancer using magnetic nanoparticles: Presentation of a new interstitial technique, Int. J. Hyperth. 21 (2005) 637–647. https://doi.org/10.1080/02656730500158360.

[36] A. Jordan, P. Wust, H. Fähling, W. John, A. Hinz, R. Felix, Inductive heating of ferrimagnetic particles and magnetic fluids: Physical evaluation of their potential for hyperthermia, Int. J. Hyperth. 9 (1993) 51–68. https://doi.org/10.3109/02656739309061478.

[37] G. Wang, D. Xu, Q. Chai, X. Tan, Y. Zhang, N. Gu, J. Tang, Magnetic fluid hyperthermia inhibits the growth of breast carcinoma and downregulates vascular endothelial growth factor expression, Oncol. Lett. 7 (2014) 1370–1374. https://doi.org/10.3892/ol.2014.1893.

[38] L.W. Bassett, S. Lee-Felker, 26 - Breast Imaging Screening and Diagnosis, in: K.I. Bland, E.M. Copeland, V.S. Klimberg, W.J.B.T. Gradishar (Eds.), The Breast, Fifth Edit, Elsevier, 2018: pp. 337–361. https://doi.org/https://doi.org/10.1016/B978-0-323-35955-9.00026-X.

[39] B.K. Byrd, V. Krishnaswamy, J. Gui, T. Rooney, R. Zuurbier, K. Rosenkranz, K. Paulsen, R.J. Barth, The shape of breast cancer, Breast Cancer Res. Treat. 183 (2020) 403–410. https://doi.org/10.1007/s10549-020-05780-6.

[40] S.K. Kandala, E. Liapi, L.L. Whitcomb, A. Attaluri, R. Ivkov, Temperature-controlled power modulation compensates for heterogeneous nanoparticle distributions: a computational optimization analysis for magnetic hyperthermia, Int. J. Hyperth. 36 (2019) 115–129. https://doi.org/10.1080/02656736.2018.1538538.

[41] Y. Tang, R.C.C. Flesch, T. Jin, Numerical investigation of temperature field in magnetic hyperthermia considering mass transfer and diffusion in interstitial tissue, J. Phys. D. Appl. Phys. 51 (2018). https://doi.org/10.1088/1361-6463/aa9b9a.

[42] Y.D. Tang, T. Jin, R.C.C. Flesch, H.Y. Jiang, Simultaneous Optimization of Injection Dose and Location for Magnetic Hyperthermia Using Metaheuristic Algorithms, IEEE Trans. Magn. 56 (2020) 1–6. https://doi.org/10.1109/TMAG.2019.2949933.

[43] Q. Jiang, F. Ren, C. Wang, Z. Wang, G. Kefayati, S. Kenjeres, K. Vafai, Y. Liu, H. Tang, On the magnetic nanoparticle injection strategy for hyperthermia treatment, Int. J. Mech. Sci. 235 (2022) 107707. https://doi.org/10.1016/j.ijmecsci.2022.107707.

[44] G. Singh, N. Kumar, P.K. Avti, Computational evaluation of effectiveness for intratumoral injection strategies in magnetic nanoparticle assisted thermotherapy, Int. J. Heat Mass Transf. 148 (2020) 119129. https://doi.org/10.1016/j.ijheatmasstransfer.2019.119129.

[45] R. Roohi, S. Baromand, H. Emdad, M. Reza, Optimization of focused multi-site injection therapy to provide the desired temperature pattern for arbitrary tumor

configuration based on MNP hyperthermia : Implementation of dual phase lag bioheat equation, Ain Shams Eng. J. 12 (2021) 901–915. https://doi.org/10.1016/j.asej.2020.05.016.

[46] M.P. Boroon, M.B. Ayani, S.R. Bazaz, Estimation of the optimum number and location of nanoparticle injections and the specific loss power for ideal hyperthermia, J. Therm. Biol. 72 (2018) 127–136. https://doi.org/10.1016/j.jtherbio.2018.01.010.

[47] I. Astefanoaei, I. Dumitru, A. Stancu, H. Chiriac, A thermo-fluid analysis in magnetic hyperthermia, Chinese Phys. B. 23 (2014) 044401 (1–7). https://doi.org/10.1088/1674-1056/23/4/044401.

[48] M. Mital, Hooman V. Tafreshi, A methodology for determining optimal thermal damage in magnetic nanoparticle hyperthermia cancer treatment, Training. 4179 (2008) 53. https://doi.org/10.1002/cnm.1456.

[49] Y. Tang, R. C. C. Flesch, T. Jin, Injection Strategy for the Optimization of Therapeutic Temperature Profile Considering Irregular Tumors in Magnetic Hyperthermia, IEEE Trans. Magn. 54 (2018) 1–6. https://doi.org/10.1109/TMAG.2018.2808206.

[50] F. Soetaert, L. Dupre, G. Crevecoeur, Computational analysis of the effect of superparamagnetic nanoparticle properties on bioheat transfer in magnetic nanoparticle hyperthermia, 2016 Int. Symp. Fundam. Electr. Eng. (2016) 1–5. https://doi.org/10.1109/ISFEE.2016.7803170.

[51] K. Yue, C. Yu, Q. Lei, Y. Luo, X. Zhang, Numerical simulation of effect of vessel bifurcation on heat transfer in the magnetic fluid hyperthermia, Appl. Therm. Eng. 69 (2014) 11–18. https://doi.org/10.1016/j.applthermaleng.2014.04.035.

[52] Y. Tang, T. Jin, R.C.C. Flesch, Numerical temperature analysis of magnetic hyperthermia considering nanoparticle clustering and blood vessels, IEEE Trans. Magn. 53 (2017) 1–6. https://doi.org/10.1109/TMAG.2017.2722425.

[53] B. Gheflati, N. Naghavi, Computational study of nanoparticle assisted hyperthermia in tumors embedded with large blood vessels, Int. J. Heat Mass Transf. 151 (2020) 1–10. https://doi.org/10.1016/j.ijheatmasstransfer.2020.119415.

[54] F. Soetaert, L. Dupré, R. Ivkov, G. Crevecoeur, Computational evaluation of amplitude modulation for enhanced magnetic nanoparticle hyperthermia, Biomed. Tech. 60 (2015)

491–504. https://doi.org/10.1515/bmt-2015-0046.

[55] A.A. Golneshan, M. Lahonian, Diffusion of magnetic nanoparticles in a multi-site injection process within a biological tissue during magnetic fluid hyperthermia using lattice Boltzmann method, Mech. Res. Commun. 38 (2011) 425–430. https://doi.org/10.1016/j.mechrescom.2011.05.012.

[56] M. Lahonian, A.A. Golneshan, Numerical study of temperature distribution in a spherical tissue in magnetic fluid hyperthermia using lattice Boltzmann method, IEEE Trans. Nanobioscience. 10 (2011) 262–268. https://doi.org/10.1109/TNB.2011.2177100.

[57] Y. Tang, T. Jin, R.C.C. Flesch, Impact of different infusion rates on mass diffusion and treatment temperature field during magnetic hyperthermia, Int. J. Heat Mass Transf. 124 (2018) 639–645. https://doi.org/10.1016/j.ijheatmasstransfer.2018.03.096.

[58] J.H. Seo, R. Mittal, A sharp-interface immersed boundary method with improved mass conservation and reduced spurious pressure oscillations, J. Comput. Phys. 230 (2011) 7347–7363. https://doi.org/10.1016/j.jcp.2011.06.003.

[59] M. Kumar, S. Roy, A sharp interface immersed boundary method for moving geometries with mass conservation and smooth pressure variation, Comput. Fluids. 137 (2016) 15–35. https://doi.org/10.1016/j.compfluid.2016.07.008.

[60] E.R. Mittal, G. Iaccarino, Immersed Boundary Methods, Annu. Rev. Fluid Mech. 37 (2005) 239–261. https://doi.org/10.1146/annurev.fluid.37.061903.175743.

[61] S. Das, A. Panda, N.G. Deen, J.A.M. Kuipers, A sharp-interface Immersed Boundary Method to simulate convective and conjugate heat transfer through highly complex periodic porous structures, Chem. Eng. Sci. 191 (2018) 1–18. https://doi.org/10.1016/j.ces.2018.04.061.

[62] S. Roy, A. De, E. Balaras, Immersed Boundary Method, Springer, Singapore, 2020. https://doi.org/https://doi.org/10.1007/978-981-15-3940-4.

[63] A. Fedorov, R. Beichel, J. Kalpathy-Cramer, J. Finet, J.C. Fillion-Robin, S. Pujol, C. Bauer, D. Jennings, F. Fennessy, M. Sonka, J. Buatti, S. Aylward, J. V. Miller, S. Pieper, R. Kikinis, 3D Slicer as an image computing platform for the Quantitative Imaging Network, Magn. Reson. Imaging. 30 (2012) 1323–1341.

https://doi.org/10.1016/j.mri.2012.05.001.

[64] A.A. Golneshan, M. Lahonian, The effect of magnetic nanoparticle dispersion on temperature distribution in a spherical tissue in magnetic fluid hyperthermia using the lattice Boltzmann method, Int. J. Hyperth. 27 (2011) 266–274. https://doi.org/10.3109/02656736.2010.519370.

[65] N. Siauve, L. Nicolas, C. Vollaire, C. Marchal, Optimization of the sources in local hyperthermia using a combined finite element-genetic algorithm method, 8 (2004) 815–833. https://doi.org/10.1080/02656730410001711664.

[66] S.M. Becker, A. V. Kuznetsov, Heat Transfer and Fluid Flow in Biological Processes, 2015. https://doi.org/10.1016/C2012-0-03651-4.

[67] C.K. Charny, Bioengineering Heat Transfer, Adv. Heat Transf. 22 (1992) 19–155. http://www.sciencedirect.com/science/article/pii/S0065271708703447.

[68] E.H. Wissler, Pennes' 1948 paper revisited, J. Appl. Physiol. 85 (1998) 35–41. https://doi.org/https://doi.org/10.1152/jappl.1998.85.1.35.

[69] H.K. Versteeg, W. Malalasekera, An introduction to computational fluid dynamics: the finite volume method, Pearson education, 2007.

[70] M. Kumar, S. Roy, M.S. Ali, An efficient immersed boundary algorithm for simulation of flows in curved and moving geometries, Comput. Fluids. 129 (2016) 159–178. https://doi.org/10.1016/j.compfluid.2016.02.009.

[71] A. Gilmanov, F. Sotiropoulos, A hybrid Cartesian/immersed boundary method for simulating flows with 3D, geometrically complex, moving bodies, J. Comput. Phys. 207 (2005) 457–492. https://doi.org/10.1016/j.jcp.2005.01.020.

[72] A. Mark, R. Rundqvist, F. Edelvik, Comparison between different immersed boundary conditions for simulation of complex fluid flows, Fluid Dyn. Mater. Process. 7 (2011) 241–258.

[73] A. Mark, B.G.M. Van Wachem, Derivation and validation of a novel implicit second-order accurate immersed boundary method, 227 (2008) 6660–6680. https://doi.org/10.1016/j.jcp.2008.03.031.

[74] F. Municchi, S. Radl, International Journal of Heat and Mass Transfer Consistent

closures for Euler-Lagrange models of bi-disperse gas-particle suspensions derived from particle-resolved direct numerical simulations, Int. J. Heat Mass Transf. 111 (2017) 171–190. https://doi.org/10.1016/j.ijheatmasstransfer.2017.03.122.

[75] X. He, S. McGee, J.E. Coad, F. Schmidlin, P.A. Iaizzo, D.J. Swanlund, S. Kluge, E. Rudie, J.C. Bischof, Investigation of the thermal and tissue injury behaviour in microwave thermal therapy using a porcine kidney model, Int. J. Hyperth. 20 (2004) 567–593. https://doi.org/10.1080/0265673042000209770.

[76] J.A. Pearce, Relationship between Arrhenius models of thermal damage and the CEM 43 thermal dose, Energy-Based Treat. Tissue Assess. 7181 (2009) 718104. https://doi.org/10.1117/12.807999.

[77] D.J. Schutt, D. Haemmerich, Effects of variation in perfusion rates and of perfusion models in computational models of radio frequency tumor ablation, Med. Phys. 35 (2008) 3462–3470. https://doi.org/10.1118/1.2948388.

[78] P. Vaupel, F. Kallinowski, P. Okunieff, Blood Flow, Oxygen and Nutrient Supply, and Metabolic Microenvironment of Human Tumors: A Review, Cancer Res. 49 (1989) 6449–6465.

[79] S. Soni, H. Tyagi, R.A. Taylor, A. Kumar, The influence of tumour blood perfusion variability on thermal damage during nanoparticle-assisted thermal therapy, Int. J. Hyperth. 31 (2015) 615–625. https://doi.org/10.3109/02656736.2015.1040470.

[80] I. V. Agafonkina, A.G. Belozerov, A.O. Vasilyev, A. V. Pushkarev, D.I. Tsiganov, A. V. Shakurov, A.A. Zherdev, Thermal Properties of Human Soft Tissue and Its Equivalents in a Wide Low-Temperature Range, J. Eng. Phys. Thermophys. 94 (2021) 233–246. https://doi.org/10.1007/s10891-021-02292-y.

[81] L. Bianchi, F. Cavarzan, L. Ciampitti, M. Cremonesi, F. Grilli, P. Saccomandi, Thermophysical and mechanical properties of biological tissues as a function of temperature: a systematic literature review, Int. J. Hyperth. 39 (2022) 297–340. https://doi.org/10.1080/02656736.2022.2028908.

[82] M. Nabaei, M. Karimi, Numerical investigation of the effect of vessel size and distance on the cryosurgery of an adjacent tumor, J. Therm. Biol. 77 (2018) 45–54. https://doi.org/https://doi.org/10.1016/j.jtherbio.2018.08.001.

[83] I. dos Santos, D. Haemmerich, D. Schutt, A.F. da Rocha, L.R. Menezes, Probabilistic finite element analysis of radiofrequency liver ablation using the unscented transform, Phys. Med. Biol. 54 (2009) 627–640. https://doi.org/10.1088/0031-9155/54/3/010.

[84] K. Clark, B. Vendt, K. Smith, J. Freymann, J. Kirby, P. Koppel, S. Moore, S. Phillips, D. Maffitt, M. Pringle, The Cancer Imaging Archive (TCIA): maintaining and operating a public information repository, J. Digit. Imaging. 26 (2013) 1045–1057.

[85] J.B. Doshi, Differential Equations for Scientists and Engineers, Narosa Publishing House, India, 2010. https://api.semanticscholar.org/CorpusID:118317943.

[86] N. Kumar, S. Suneet, J.B. Doshi, Nodal Integral Method Using Quadrilateral Elements for Transport Equations : Part 1 — Convection-diffusion Equation, Numer. Heat Transf. 64 (2013) 1–21. https://doi.org/10.1080/10407790.2013.784125.

[87] C.T. Lin, K.C. Liu, Estimation for the heating effect of magnetic nanoparticles in perfused tissues, Int. Commun. Heat Mass Transf. 36 (2009) 241–244. https://doi.org/10.1016/j.icheatmasstransfer.2008.11.006.

[88] R.E. Rosensweig, Heating magnetic fluid with alternating magnetic fiel, J. Urol. 152 (1994) 2098–2100. https://doi.org/10.1016/S0022-5347(17)32321-2.

[89] L.W. Bassett, S. Lee-Felker, 26 - Breast imaging screening and diagnosis, in: K.I. Bland, E.M. Copeland, V.S. Klimberg, W.J.B.T. Gradishar (Eds.), The Breast, Fifth Edit, Elsevier, 2018: pp. 337–361. https://doi.org/10.1016/B978-0-323-35955-9.00026-X.

[90] J.D. Brierley, M.K. Gospodarowicz, C. Wittekind, TNM classification of malignant tumours, 8th ed., John Wiley & Sons, Geneva, Switzerland, 2017.

[91] H.M. Byrne, M.A.J. Chaplain, Modelling the role of cell-cell adhesion in the growth and development of carcinomas, Math. Comput. Model. 24 (1996) 1–17. https://doi.org/https://doi.org/10.1016/S0895-7177(96)00174-4.

[92] J. Wu, Stationary solutions of a free boundary problem modeling the growth of tumors with Gibbs-Thomson relation, J. Differ. Equ. 260 (2016) 5875–5893. https://doi.org/10.1016/j.jde.2015.12.023.

[93] M.J. Lu, C. Liu, J. Lowengrub, S. Li, Complex Far-Field Geometries Determine the Stability of Solid Tumor Growth with Chemotaxis, Bull. Math. Biol. 82 (2020) 1–41. https://doi.org/10.1007/s11538-020-00716-z.

[94] World Health Organization.WHO handbook for reporting results of cancer treatment.Geneva, WHO, (1979) 1–45. https://iris.who.int/handle/10665/37200.

[95] M. Sefidgar, M. Soltani, K. Raahemifar, H. Bazmara, S.M.M. Nayinian, M. Bazargan, Effect of tumor shape, size, and tissue transport properties on drug delivery to solid tumors, J. Biol. Eng. 8 (2014) 1–13. https://doi.org/10.1186/1754-1611-8-12.

[96] J. Köller, Egg curves and ovals, Math. Basteleien. (2019). http://www.mathematische-basteleien.de/eggcurves.htm,2017 (accessed December 13, 2019).

[97] A.S. Tavill, B.R. Bacon, Hemochromatosis: How much iron is too much?, Hepatology. 6 (1986) 142–145. https://doi.org/10.1002/hep.1840060128.

[98] P. Gas, J. Wyszkowska, Influence of multi-tine electrode configuration in realistic hepatic RF ablative heating, Arch. Electr. Eng. 68 (2019) 521–533. https://doi.org/10.24425/aee.2019.129339.

[99] M.H.H. Tehrani, M. Soltani, F.M. Kashkooli, K. Raahemifar, Use of microwave ablation for thermal treatment of solid tumors with different shapes and sizes—A computational approach, PLoS One. 15 (2020) e0233219. https://doi.org/https://doi.org/10.1371/journal.pone.0233219.

[100] G.C. Van Rhoon, T. Samaras, P.S. Yarmolenko, M.W. Dewhirst, E. Neufeld, N. Kuster, CEM43°C thermal dose thresholds: A potential guide for magnetic resonance radiofrequency exposure levels?, Eur. Radiol. 23 (2013) 2215–2227. https://doi.org/10.1007/s00330-013-2825-y.

[101] P.L. Zadnik, C.A. Molina, R. Sarabia-Estrada, M.L. Groves, M. Wabler, J. Mihalic, E.F. McCarthy, Z.L. Gokaslan, R. Ivkov, D.M. Sciubba, Characterization of intratumor magnetic nanoparticle distribution and heating in a rat model of metastatic spine disease, J. Neurosurg. Spine. 20 (2014) 740–750. https://doi.org/10.3171/2014.2.SPINE13142.

[102] M. Dewhirst, P.R. Stauffer, S. Das, O.I.C. Cra, Z. Vujaskovic, Hyperthermia, in: L.L. Gunderson, J.E. Tepper (Eds.), Clin. Radiat. Oncol., Fourth ed., Elsevier Health Sciences, china, 2016: pp. 381–398. https://books.google.co.in/books?id=m5ruCQAAQBAJ.

[103] J.F. Van Der Koijk, J.J.W. Lagendijk, J. Crezee, J. De Bree, A.N.T.J. Kotte, G.M.J. Van Leeuwen, J.J. Battermann, The influence of vasculature on temperature distributions in

MECS interstitial hyperthermia: Importance of longitudinal control, Int. J. Hyperth. 13 (1997) 365–385. https://doi.org/10.3109/02656739709046539.

[104] A. LeBrun, R. Ma, L. Zhu, MicroCT image based simulation to design heating protocols in magnetic nanoparticle hyperthermia for cancer treatment, J. Therm. Biol. 62 (2016) 129–137. https://doi.org/https://doi.org/10.1016/j.jtherbio.2016.06.025.

[105] Q. Wang, Z.S. Deng, J. Liu, Theoretical evaluations of magnetic nanoparticle-enhanced heating on tumor embedded with large blood vessels during hyperthermia, J. Nanoparticle Res. 14 (2012) 1–10. https://doi.org/10.1007/s11051-012-0974-6.

[106] M. Sefidgar, L. Alinezhad, E. Bashooki, P. Shojaee, Effect of different dynamic microvasculature in a solid tumor with the necrotic region during magnetic hyperthermia: An in-silico study, Int. J. Heat Mass Transf. 189 (2022) 122662. https://doi.org/10.1016/j.ijheatmasstransfer.2022.122662.

[107] Y. Hou, J. Konen, D.J. Brat, A.I. Marcus, L.A.D. Cooper, TASI: A software tool for spatial-temporal quantification of tumor spheroid dynamics, Sci. Rep. 8 (2018) 1–9. https://doi.org/10.1038/s41598-018-25337-4.

[108] H.B. Frieboes, X. Zheng, C.H. Sun, B. Tromberg, R. Gatenby, V. Cristini, An integrated computational/experimental model of tumor invasion, Cancer Res. 66 (2006) 1597–1604. https://doi.org/10.1158/0008-5472.CAN-05-3166.

[109] A. Jordan, R. Scholz, K. Maier-Hauff, F.K.H. van Landeghem, N. Waldoefner, U. Teichgraeber, J. Pinkernelle, H. Bruhn, F. Neumann, B. Thiesen, A. von Deimling, R. Felix, The effect of thermotherapy using magnetic nanoparticles on rat malignant glioma, J. Neurooncol. 78 (2006) 7–14. https://doi.org/10.1007/s11060-005-9059-z.

[110] Y.D. Tang, J. Zou, R.C.C. Flesch, T. Jin, Effect of injection strategy for nanofluid transport on thermal damage behavior inside biological tissue during magnetic hyperthermia, Int. Commun. Heat Mass Transf. 133 (2022) 105979. https://doi.org/10.1016/j.icheatmasstransfer.2022.105979.

[111] S. De, S. Das, J.A.M. Kuipers, E.A.J.F. Peters, J.T. Padding, A coupled finite volume immersed boundary method for simulating 3D viscoelastic flows in complex geometries, J. Nonnewton. Fluid Mech. 232 (2016) 67–76. https://doi.org/10.1016/j.jnnfm.2016.04.002.

[112] A. Paul, A. Narasimhan, F.J. Kahlen, S.K. Das, Temperature evolution in tissues embedded with large blood vessels during photo-thermal heating, J. Therm. Biol. 41 (2014) 77–87. https://doi.org/https://doi.org/10.1016/j.jtherbio.2014.02.010.

[113] B. Gheflati, N. Naghavi, Computational study of nanoparticle assisted hyperthermia in tumors embedded with large blood vessels, Int. J. Heat Mass Transf. 151 (2020) 119415. https://doi.org/https://doi.org/10.1016/j.ijheatmasstransfer.2020.119415.

[114] Y. Tang, T. Jin, R.C.C. Flesch, Numerical Temperature Analysis of Magnetic Hyperthermia Considering Nanoparticle Clustering and Blood Vessels, IEEE Trans. Magn. 53 (2017) 1–6. https://doi.org/10.1109/TMAG.2017.2722425.

[115] R. Singh, K. Das, S.C. Mishra, Laser-induced hyperthermia of nanoshell mediated vascularized tissue–A numerical study, J. Therm. Biol. 44 (2014) 55–62. https://doi.org/https://doi.org/10.1016/j.jtherbio.2014.07.001.

[116] I. Astefanoaei, I. Dumitru, A. Stancu, H. Chiriac, A thermo-fluid analysis in magnetic hyperthermia, Chinese Phys. B. 23 (2014) 044401–7. https://doi.org/https://doi.org/10.1088/1674-1056/23/4/044401.

[117] A.L. Simpson, M. Antonelli, S. Bakas, M. Bilello, K. Farahani, B. Van Ginneken, A. Kopp-Schneider, B.A. Landman, G. Litjens, B. Menze, A large annotated medical image dataset for the development and evaluation of segmentation algorithms, ArXiv Prepr. ArXiv1902.09063. (2019). https://doi.org/https://doi.org/10.48550/arXiv.1902.09063.

[118] V.K. Kikinis R, Pieper SD, 3D Slicer: a platform for subject-specific image analysis, visualization, and clinical support, in: F.A. Jolesz (Ed.), Intraoperative Imaging Image-Guided Ther., First, Springer, New York, 2013: pp. 277–289. https://doi.org/https://doi.org/10.1007/978-1-4614-7657-3.

[119] Y. He, M. Shirazaki, H. Liu, R. Himeno, Z. Sun, A numerical coupling model to analyze the blood flow, temperature, and oxygen transport in human breast tumor under laser irradiation, Comput. Biol. Med. 36 (2006) 1336–1350. https://doi.org/10.1016/j.compbiomed.2005.08.004.

[120] H. Yoon, P.N. Kim, H.K. Ha, A.Y. Kim, H.J. Kim, M. Lee, CT during Hepatic Arteriography and Portography: An Illustrative Review 1, Radiographics. 22 (2002) 1041–1051.

https://doi.org/https://pubs.rsna.org/doi/10.1148/radiographics.22.5.g02se071041.

[121] F.G. Rocha, Liver blood flow: Physiology, measurement, and clinical relevance, in: W.R. Jarnagin, J. Belghiti, M.W. Büchler, W.C. Chapman (Eds.), Blumgart's Surg. Liver, Pancreas Biliary Tract, Elsevier Saunders, 2012: pp. 74–86. https://doi.org/https://doi.org/10.1016/B978-1-4377-1454-8.00004-7.

[122] K. Muralidhar, T. Sundarajan, Computational fluid flow and heat transfer, Narosa Publishing House, 1995. https://doi.org/https://books.google.co.in/books?id=X2q6AAAACAAJ.

[123] T. Horng, W. Lin, C. Liauh, T. Shih, Effects of pulsatile blood flow in large vessels on thermal dose distribution during thermal therapy, Med. Phys. 34 (2007) 1312–1320. https://doi.org/https://doi.org/10.1118/1.2712415.

[124] J. Carrey, B. Mehdaoui, M. Respaud, Simple models for dynamic hysteresis loop calculations of magnetic single-domain nanoparticles: Application to magnetic hyperthermia optimization, J. Appl. Phys. 109 (2011) 083921. https://doi.org/https://doi.org/10.1063/1.3551582.

[125] C.L. Dennis, R. Ivkov, Physics of heat generation using magnetic nanoparticles for hyperthermia, Int. J. Hyperth. 29 (2013) 715–729. https://doi.org/https://doi.org/10.3109/02656736.2013.836758.

[126] B. Thiesen, A. Jordan, Clinical applications of magnetic nanoparticles for hyperthermia, Int. J. Hyperth. 24 (2008) 467–474. https://doi.org/10.1080/02656730802104757.

[127] N. Malhotra, J. Lee, R.A.D. Liman, J.M.S. Ruallo, O.B. Villaflores, T. Ger, C. Hsiao, Potential Toxicity of Iron Oxide Magnetic Nanoparticles : A Review, Molecules. (2020) 1–26. https://doi.org/10.3390/molecules25143159.